













4DATLANTIC-OHC

PRODUCT VALIDATION REPORT (PVR)

	Name	Organization	Date	Visa
Written by :	Odilon Joël Houndegnonto William Llovel Damien Desbruyères Matthew Hammond Giuseppe Foti Francisco Mir Calafat Robin Fraudeau Florence Marti Victor Rousseau Ramiro Ferrari	LOPS NOC Magellium	15/05/2025	
Checked by :	Michael Ablain	MAGELLIUM	15/05/2025	All
Approved by :	Joel Dorandeu	MAGELLIUM	15/05/2025	Jonan
Accepted by :	Roberto Sabia	ESA		

Document reference :	OHCATL_DT_033_MAG
Edition.Revision:	3.0
Date Issued:	15/05/2025
Customer:	ESA
Ref. Market, consultation :	AO/1-10546/20/I-NB
Contrat No. :	4000134928/21/I-NB

Date: 15/05/2025 Issue: 3.0

Distribution List

	Name	Organization	Nb. copies
Sent to:	Roberto Sabia	ESA	1 (digital copy)
Internal copy:	Project Report	Magellium	1 (digital copy)

Document evolution sheet

Ed.	Rev.	Date	Purpose evolution	Comments
1	0	01/09/2022	Creation of document	
1	1	13/10/2022	Update with ESA feedback	
1	2	31/01/2023	Update with complementary analysis	Section 3.6
2	0	12/12/2024	Modifications related to version 2.0 of the product	Add section 4 and section 6.2
3	0	15/05/2025	Modifications related to version 3.0 of the product	Add section 5 and section 6.3



Date: 15/05/2025 Issue: 3.0

Contents

1. Introduction	9
1.1. Purpose of the document	g
1.2. Document structure	10
1.3. Related documents	10
1.4. Abbreviations and Acronyms	10
1.5. Bibliography	17
2. Validation on RAPID-MOCHA section (V1.0)	17
2.1. Overview	17
2.2. Data and methods	18
2.2.1. Datasets	18
2.2.1.1. 4DAtlantic	18
2.2.1.2. NOC ARGO optimally interpolated (OI) data	18
2.2.1.3. RAPID-MOCHA array data	18
2.2.2. Method	19
2.2.2.1. Trend analysis	19
2.2.2. Uncertainty analysis	19
2.2.2.3. RAPID-MOCHA processing	20
2.2.2.3.1. Estimation of OHC at the mooring locations	20
2.2.2.3.2. Estimation of OHC across the section	20
2.3. Results	21
2.3.1. Validation against NOC ARGO OI	21
2.3.1.1. 4DAtlantic v0.2	21
2.3.1.1.1. Regional average trends	21
2.3.1.1.2. Latitudinal average trends	22
2.3.1.1.3. Trend spatial distribution	23
2.3.1.2. 4DAtlantic v0.4	24
2.3.1.2.1. Region average trends	24
2.3.1.2.2. Latitudinal average trends	26
2.3.1.2.3. Trend spatial distribution	27
2.3.2. Validation against the RAPID-MOCHA array	29
2.3.2.1. Validation at mooring locations	30
2.3.2.2. Experimental versions of 4DAtlantic (v0.4-ECCO, v0.4-Mascon)	33
2.3.2.3. Assessment across the RAPID-MOCHA transect	33
2.3.2.3.1. Western Basin	33



Ref.: OHCATL_DT_033_MAG Date: 15/05/2025 Issue: 3.0

2.3.2.3.2. Eastern Basin	34
2.4. Summary	35
3. Validation on OVIDE section (V1.0)	36
3.1. Overview	36
3.2. Data and Methods	37
3.3. Interannual variability along the A25-OVIDE sections	39
3.3.1. Comparisons between the 4DAtlantic and A25-OVIDE products over 2002-2018	39
3.3.2. Sub-Basin intercomparison of the OHC estimates	41
3.4. Seasonal and interannual time scales	42
3.4.1. Seasonal full-depth OHC changes in the Irminger sea	42
3.4.2. Year-to-year full-depth OHC changes in the Irminger sea	43
3.5. Assessing the geodetic local uncertainties	45
3.6. Validation of experimental products	48
3.6.1. Overview	48
3.6.2. 4DAtlantic with ECCO model vs ISAS21 estimates	48
3.6.2.1. Seasonal full-depth OHC changes in the Irminger sea	48
3.6.2.2. Year-to-year full-depth OHC changes in the Irminger sea	49
3.6.3. 4DAtlantic with MASCON method vs ISAS21 estimates	51
3.6.3.1. Seasonal full-depth OHC changes in the Irminger sea	51
3.6.3.2. Year-to-year full-depth OHC changes in the Irminger sea	52
3.7. Summary	55
4. Validation on OVIDE section (V2.0)	56
4.1. Comparisons against A25-OVIDE sections from Greenland to Portugal coasts	56
4.2. Comparisons against ISAS21 gridded products in the North Atlantic ocean	58
5. Validation of the V3.0	60
5.1. 4DAtlantic-OHC v3.0 product	61
5.2. Comparative Assessment of 4DAtlantic-OHC v3.0 and v2.0 Products in the Atlanti62	c Basın
5.3. Evaluating differences between 4DAtlantic-OHC v3.0 and in situ products	62
5.3. Analysis of the geodetic product in the Mediterranean Sea	65
5.3. Assessing global ocean heat content from geodetic and in situ observations	66
6. Conclusions	67
6.1. Validation of the V1.0	67
6.2. Validation of the V2.0	67
6.3. Validation of the V3.0	68



Date: 15/05/2025 Issue: 3.0

List of Tables and Figures

Figure 1: Schematic showing the location of the RAPID-MOCHA (at 26.5oN) and OSNAP (red line) sections superposed on map of mean dynamic topography. The French OVIDE line across the eastern North Atlantic is also shown (Lozier et al., 2019).	11
Figure 2: Average OHC time series for the entire Subtropical North Atlantic region, showing the NOC ARGO OI (green) and 4DAtlantic v0.2 (orange) products. The dashed lines represent the linear trend for the respective datasets	19
Figure 3: Average OHC time series (de-seasonalised) for the entire Subtropical North Atlantic region, showing the NOC ARGO OI (green) and 4DAtlantic v0.2 (orange) products. The dashed vertical lines represent the location of potential changepoints identified using the At-Most-One-Change approach.	20
Figure 4: Average OHC time series in 5° latitudinal bands of the Subtropical North Atlantic region for the NOC ARGO OI (green) and 4DAtlantic v0.2 (orange) products. The dashed lines represent the linear trend for the respective datasets.	21
Figure 5: OHC trends in each 1° grid cell of the Subtropical North Atlantic region for NOC ARGO OI (top) 4DAtlantic v0.2 (bottom) products.	22
Figure 6: Average OHC time series for the entire Subtropical North Atlantic region, showing the NOC ARGO OI (green) and 4DAtlantic v0.4 (purple) products. The dashed lines represent the linear trend for the respective datasets.	23
Figure 7: Average OHC time series (de-seasonalised) for the entire Subtropical North Atlantic region, showing the NOC ARGO OI (green) and 4DAtlantic v0.4 (purple) products. The dashed vertical lines represent the location of potential changepoints identified using the At-Most-One-Change approach.	24
Figure 8: Average OHC time series in 5° latitudinal bands of the Subtropical North Atlantic region for the NOC ARGO OI (green) and 4DAtlantic v0.4 (purple) products. The dashed lines represent the linear trend for the respective datasets.	25
Figure 9: OHC trends in each 1° grid cell of the Subtropical North Atlantic region for NOC ARGO OI (top) 4DAtlantic v0.4 (bottom) products.	26
Figure 10: Map of the Subtropical North Atlantic region showing where the NOC ARGO OI OHC trends are significantly different from the 4DAtlantic v0.4 trends at a 2σ significance level. Maps of 4DAtlantic v0.4 OHC trends with this mask applied can be seen in Figure 11.	27
Figure 11: OHC trends in each 1° grid cell of the Subtropical North Atlantic region for the	27



Figure 11: OHC trends in each 1° grid cell of the Subtropical North Atlantic region for the

Date: 15/05/2025

Issue: 3.0

4DAtlantic v0.4 product. Where a trend is significantly different from ARGO (c.f. Figure 9 and Figure 10) it is treated as zero (i.e. white).

Figure 12: Schematic showing the name, location, and vertical extent of the RAPID-MOCHA moorings. Blue arrows indicate moorings used in this study, Western Boundary (WB) left, Mid Atlantic Ridge West (MAR-West) middle, Eastern Boundary (EB) right.

28

Figure 13: Temporal evolution of depth-integrated OHC anomaly computed at the RAPID-MOCHA mooring location using a 10-day low-pass filter (grey) and a 1-year moving average (black), for the average of the Western boundary (top, left), the mooring west of the Mid-Atlantic Ridge (bottom, left) and the average of the Eastern boundary (bottom, right).

29

Figure 14: Temporal evolution of depth-integrated OHC anomaly at the mooring locations estimated from RAPID (black), NOC ARGO OI (grey), 4DAtlantic v0.2 (yellow) and 4DAtlantic v0.4 (purple), for the average of the Western boundary (top, left), the mooring west of the Mid-Atlantic Ridge (bottom, left) and the average of the Eastern boundary (bottom, right).

30

Figure 15: Temporal evolution of depth-integrated OHC anomaly at the mooring locations estimated from RAPID (black), NOC ARGO OI (grey), 4DAtlantic v0.2 (yellow) and 4DAtlantic v0.4 (purple), for the average of the Western boundary (top, left), the mooring west of the Mid-Atlantic Ridge (bottom, left) and the average of the Eastern boundary (bottom, right). Comparison with 4DAtlantic experimental products v0.4 ECCO (green) and 4DAtlantic Mascon (cyan).

31

Figure 16: De-seasonalised temporal evolution of depth-integrated OHC anomaly estimated from the RAPID array at 26.5N spatially integrated across the Western basin of the North Atlantic (cyan). Comparison with estimates from 4DAtlantic OHC anomalies (red) computed using release v0.2 (top, left), v0.4(top, right), v0.4 ECCO (bottom, left) and v0.4 Mascon (bottom, right). Respective trends shown with dashed lines.

32

Figure 17 De-seasonalised temporal evolution of depth-integrated OHC anomaly estimated from the RAPID array at 26.5N spatially integrated across the Eastern basin of the North Atlantic (cyan). Comparison with estimates from 4DAtlantic OHC anomalies (red), computed using release v0.2 (top, left), v0.4(top, right), v0.4 ECCO (bottom, left) and v0.4 Mascon (bottom, right). Respective trends shown with dashed lines.

33

Figure 18: The north Atlantic ocean area. Bathymetry is based on the ETOPO dataset (doi:10.7289/V5C8276M) with the solid black line showing the -2000m isobath. The red line shows the A25-OVIDE hydrography sections. The black hatched area represents the Irminger sea for the validation of the Ocean Heat Content (OHC) estimates from the space geodetic 4DAtlantic product. The green contour corresponds to the commun area between the 4DAtlantic product and the in situ-based product for validation purposes.

Figure 19: Intercomparison of time series of the full depth Ocean Heat Content Anomalies



Date: 15/05/2025

Issue: 3.0

(OHC) estimates averaged along the A25-OVIDE line from (a) geodetic 4DAtlantic-OHC v0.4 product and in situ OVIDE hydrographic data set (black curve). The light blue and cyan bands represent respectively the lower and upper bounds of the error associated with the OHC estimates from the 4DAtlantic product. (b) A25-OVIDE 0-2000m layer's OHC (solid red cure) and 2000m-bottom (dashed red curve). The OHC are referred to the OHC mean over A25-OVIDE sections period (2002-2020).

Figure 20: a) Scatter-plot of Ocean Heat Content estimates from 4DAtlantic OHC v0.4 product (vertical axis) and from in situ A25-OVIDE sections hydrographic data set (horizontal axis). The color of the dots indicates the distance from the Greenland; b) Systematic difference between OHC estimates from 4DAtlanti product and from in situ A25-OVIDE data set.

40

Figure 21: Decomposition of the OHC time series of the A25-OVIDE line into two sub-basins in the Subpolar North Atlantic: (a) for the Irminger sea (West of the Reykjanes Ridge until greenland) and (b) for the Iceland and the Iberian basins (West European basin between Reykjanes Ridge and Portugal). Time series show the space geodetic 4DAtlantic OHC estimates (blue curve), the in situ A25-OVIDE OHC estimates for the full-depth (black curve) and 0-2000m layer (red curve). The light blue and cyan bands represent respectively the lower and upper bounds of the error associated with the OHC estimates from the 4DAtlantic product. The OHC are referred to the OHC mean over A25-OVIDE sections period (2002-2020).

41

Figure 22: 2002-2020 climatology of seasonal time series of the full-depth OHC estimates from the geodetic 4DAtlantic product (blue curve) and ISAS21 product (black curve) in the Irminger Sea. The vertical blue and black bars represent the spatial STD for the selected domain for Irminger sea. The magenta curve represents the estimates of OHC seasonal cycle for the layer of 2000m-bottom from ISAS21 product.

42

Figure 23: Interannual time series of the Ocean Heat Content Anomalies (OHC) referred the 2002-2020 OHC mean in the Irminger (area of green contour of the Figure 1) estimated from the space geodetic 4DAtlantic OHC product (solid blue curve) and the in situ ISAS21 data set (solid black curve). The dashed red and black curves are OHC trend lines from 4DAtlantic and ISAS21 estimates respectively. The light blue and cyan bands represent the lower and upper bounds of error associated with the OHC estimates from the 4DAtlantic product.

43

Figure 24: Trends of Ocean Heat Content Anomalies (OHC) from (a) 4DAtlantic product and (b) ISAS21 in situ product in the SPNA.

43

Figure 25: Interannual time series of OHC changes estimates over 2002-2020 in the Irminger sea from the geodetic 4DAtlantic product (blue curve) and from ISAS21 in situ product (black curve). Time series of OHC changes within the layer from 2000m depth to bottom (magenta curve) from ISAS21 in situ product. The light blue and cyan bands represent the lower and upper bounds of error associated with the OHC estimates from the 4DAtlantic product.



Date: 15/05/2025

Issue: 3.0

Figure 26: (a) OHC estimates from in situ OVIDE hydrographic with the full-resolution (black curve), with the geodetic 4DAtlantic-OHC v0.4 grid resolution (1°x1°, red curve) and from 4DAtlantic-OHC product (blue curve) averaged along A25-OVIDE line. (b) Difference of OHC A25-OVIDE estimates between the full in situ resolution and satellite-derived grid resolution: OHC = OHCA(OVIDE)full resolution - OHCA(OVIDE)satellite resolution(red barplot).

45

Figure 27: (a) Full-depth Steric sea level anomalies (SSLA) estimates from A25-OVIDE hydrographic data (black curve) and the space geodetic 4DAtlantic product (blue curve) and, the associated Sea Level Anomalies (LSA) from CMEMS product (magenta curve) during 2002-2018. The light blue and cyan bands represent respectively the lower and upper bounds of the error associated with the SSL estimates from the 4DAtlantic product. (b) sub-layer decomposition of the halosteric sea level anomalies (HSSLA): 0-2000m depth layer (solid red curve) and for the layer below 2000m (dashed red curve).

47

Figure 28: The north Atlantic ocean area (left panel). Bathymetry is based on the ETOPO dataset (doi:10.7289/V5C8276M) with the solid black line showing the -2000m isobath. Right: Commun area of the Irminger sea between 4DAtlantic-OHC (with ECCO model) and ISAS21 products, and the red contour (hatched area) corresponds to the common area between the 4DAtlantic product (with MASCON method) and the ISAS21 product for validation purposes.

48

Figure 29: 2002-2017 climatology of seasonal time series of the full-depth OHC estimates from the geodetic 4DAtlantic (with ECCO model) product (blue curve) and ISAS21 product (black curve) in the Irminger Sea. The vertical blue and black bars represent the spatial STD for the selected domain for Irminger sea. The magenta curve represents the estimates of OHC seasonal cycle for the layer of 2000m-bottom from ISAS21 product.

49

Figure 30: Interannual time series of the Ocean Heat Content Anomalies (OHC) referred the 2002-2017 OHC mean in the Irminger (selected area of the Figure 28, right figure) estimated from the space geodetic 4DAtlantic OHC product with ECCO model (solid blue curve) and the in situ ISAS21 data set (solid black curve). The magenta curve represents the interannual time series of OHC from ISAS21 within the layer of 2000m to bottom. The dashed magenta and black curves are OHC trend lines from 4DAtlantic and ISAS21 estimates respectively. The light blue and cyan bands represent the lower and upper bounds of error associated with the OHC estimates from the 4DAtlantic product.

50

Figure 31: Interannual time series of OHC changes estimates over 2002-2017 in the Irminger sea from the geodetic 4DAtlantic product with ECCO model (blue curve) and from ISAS21 in situ product (black curve). Time series of OHC changes within the layer from 2000m depth to bottom (magenta curve) from ISAS21 in situ product. The light blue and cyan bands represent the lower and upper bounds of error associated with the OHC estimates from the 4DAtlantic product.

50

Figure 32: Trends of Ocean Heat Content Anomalies (OHC) over 2002-2017 from (a) 4DAtlantic product (with ECCO model) and (b) ISAS21 in situ product in the SPNA, and (c



Date: 15/05/2025

Issue: 3.0

) represents the difference between (a) and (b).

Figure 33: 2002-2020 climatology of seasonal time series of the full-depth OHC estimates from the geodetic 4DAtlantic (with MASCON method) product (blue curve) and ISAS21 product (black curve) in the Irminger Sea. The green curve stands for the 2002-2017 climatology of seasonal time series of the full-depth OHC from 4DAtlantic product (with ECCO model) within the red contour of the Figure 28 (right panel). The vertical blue, green and black bars represent the associated spatial STD for each selected for the Irminger sea. The magenta curve represents the estimates of OHC seasonal cycle for the layer of 2000m-bottom from ISAS21 product.

52

Figure 34: Interannual time series of the Ocean Heat Content Anomalies (OHC) referred the 2002-2020 OHC mean in the Irminger (within the red contour of the Figure 28, right panel) estimated from the space geodetic 4DAtlantic OHC product with MASCON method (solid blue curve) and the in situ ISAS21 data set (solid black curve). The magenta curve represents the interannual time series of OHC from ISAS21 within the layer of 2000m to bottom. The green curve stands for the interannual OHC time series from 4DAtlantic (with ECCO model, within the red contour of the Figure 28) over 2002-2017. The dashed magenta, red and black curves are OHC trend lines from 4DAtlantic (with MASCON method and ECCO model respectively) and ISAS21 estimates respectively. The light blue and cyan bands represent the lower and upper bounds of error associated with the OHC estimates from the 4DAtlantic product (with MASCON method).

53

Figure 35: Trends of Ocean Heat Content Anomalies (OHC) over 2002-2020 from (a) 4DAtlantic product (with MASCON method) and (b) ISAS21 in situ product in the SPNA, and (c) represents the difference between (a) and (b).

54

Figure 36: Interannual time series of OHC changes estimates over 2002-2020 in the Irminger sea from the geodetic 4DAtlantic product with MASCON method (blue curve) and from ISAS21 in situ product (black curve). The green curve stands for the one over 2002-2017 from the 4DAtlantic-OHC with ECCO model. The magenta curve represents the time series of OHC changes within the layer from 2000m depth to bottom from ISAS21 in situ product. The light blue and cyan bands represent the lower and upper bounds of error associated with the OHC estimates from the 4DAtlantic product.

55

Figure 37: Time series of Ocean Heat Content per unit area (in J m-2) along the A25-OVIDE section over 2002-2021 for ISAS21 (black lines), the 4DAtlantic products (blue lines; V1 upper panel, V2alpha middle panel and V2official for the lower panel). The dashed red and black curves are OHC linear fits from 4Datlantic products and ISAS21 estimates respectively. The blue envelops represent the uncertainty range derived from the 4DAtlantic products. The red dots represent the full-depth OHC estimates from full-depth and high-resolution repeat hydrography cruises.

59

Figure 38: OHC trend maps (in W m-2) over 2005-2020 from 4DatlanticV1 product (upper left panel), ISAS21 in situ product (upper right panel) and the difference between 4Datlantic and ISAS21 products (lower right panel).



Figure 39: OHC trend maps (in W m-2) over 2005-2020 from 4DatlanticV2alpha product (upper left panel), ISAS21 in situ product (upper right panel) and the difference between 4Datlantic and ISAS21 products (lower right panel) and between 4Datlantic V2alpha and V1 (lower right panel).	61
Figure 40: OHC trend maps (in W m-2) over 2005-2020 from 4DatlanticV2official product (upper left panel), ISAS21 in situ product (upper right panel) and the difference between 4Datlantic V2 official and ISAS21 products (lower right panel) and between 4Datlantic V2official and V1 (lower right panel).	61
Figure 41: Anomalies in the Ocean Heat Content Trends (a) and variance (b) estimated using 4DAtlantic v3 dataset for the period April 2002–December 2022.	63
Figure 42: Anomalies in Ocean Heat Content Trend (a) and Variance (b): Differences between 4DAtlantic v3 and v2.	64
Figure 43: Ocean Heat Content Trend Anomalies from 4DAtlantic v3 and in situ products.	65
Figure 44: Standard deviation of the Ocean Heat Content from 4DAtlantic v3 and in situ products.	66
Figure 45: Anomalies in the Ocean Heat Content Trends (a) and variance (b) estimated using 4DAtlantic v3 dataset for the period April 2002–December 2022 in the	67
Mediterranean Sea.	67
Figure 46: Time series of Global Ocean Heat Content derived from the 4DAtlantic v2 (red) and v3 (blue) datasets for the Atlantic Basin.	68
Figure 47: Time series of Global Ocean Heat Content derived from the 4DAtlantic v3 and in situ products.	68



Date: 15/05/2025

Issue: 3.0

1. Introduction

1.1. Purpose of the document

The objective of this document is to resume the validation activities that were carried out on the 4DAtlantic-OHC product. The space geodetic will be compared against in-situ observations over two test sites (see figure below):

- RAPID-MOCHA section
- OVIDE section

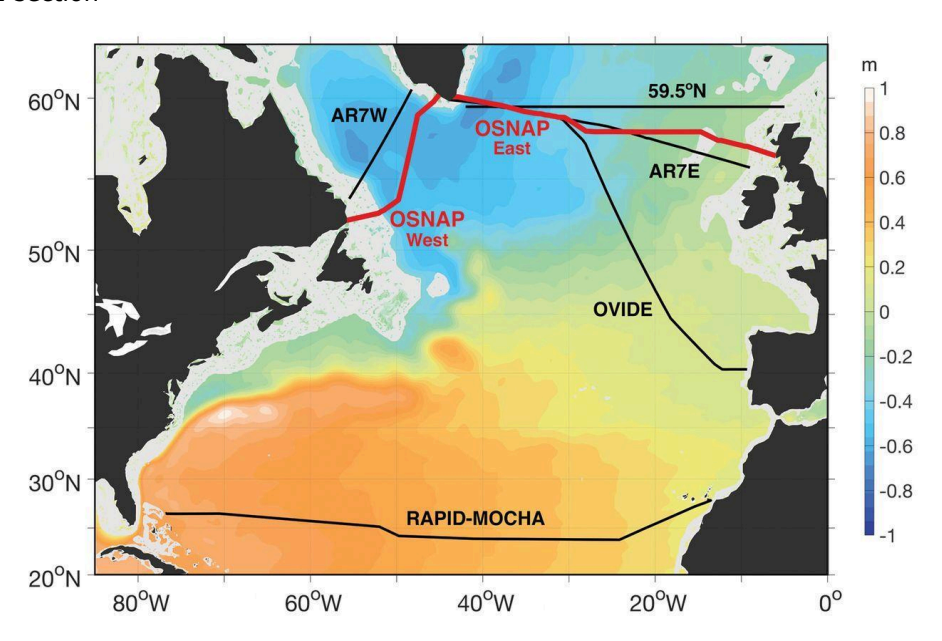


Figure 1: Schematic showing the location of the RAPID-MOCHA (at 26.50N) and OSNAP (red line) sections superposed on map of mean dynamic topography. The French OVIDE line across the eastern North Atlantic is also shown (Lozier et al., 2019).

The objective of this validation study is to provide a detailed experimental error analysis for evaluating the accuracy and reliability of the OHC-4DAtlantic product at these 2 test sites, based on the performance of each algorithm. These two test sites are representative of different oceanic processes that depend on latitude. In the North Atlantic region, the sub-tropical area (RAPID-MOCHA) is important to study because an important part of the heat transport through the North Atlantic Ocean occurs there at the surface and interacts with the atmosphere and ultimately modulates the climate variability of Western Europe. Concerning sub-polar region (OVIDE-AR7W), the gyre over there plays a fundamental role in the large-scale redistribution of physical and biogeochemical properties (e.g. heat, freshwater, carbon) within the ocean interior. Both places are therefore key actors of the Earth climate system.

The validation will also compare the ameliorations that were added to the product during the development activities, in particular thorough understanding of the range of validity, limits and benefits of the newly generated products, specifically for regional algorithms and developments. Finally, the validation will use regional uncertainties that are provided by the space geodetic product for their analysis and provide some recommendations for further improvements of the 4DAtlantic OHC product.



Date: 15/05/2025

Issue: 3.0

For the first test site (RAPID-MOCHA), the objective is to assess how well the product captures the space-time structure of ocean heat content in the in-situ data over seasonal and longer time scales. It will be compared against NOC ARGO OI dataset, as well as from the RAPID-MOCHA mooring array.

For the second test site (OVIDE) the objectives are the same but the comparison will be focused with Deep-Argo profiles that are available on this area and evaluating the OHC-Atlantic product on interannual to decadal timescales (inc. linear trend).

These validation activities have been carried out independently from the development activities, they have been conducted on some intermediate versions of the product (name V0.X) that were released internally during development phases. The final intermediate version of the product is the version V0.4. This version was chosen to be the official version 1.0 of the product.

1.2. Document structure

In addition to this introduction, the document is organised as follows:

- Section 2 describes the validation performed on the RAPID-MOCHA section
- Section 3 describes the validation performed on the OVIDE section
- Section 4 provides a conclusion of the validation activities

1.3. Related documents

Id.	Description
[AD-1]	4DAtlantic - Detailed Proposal, MAG-19-PTF-120-Vol1
[AD-2]	4DAtlantic - OHC Algorithm Theoretical Basis Document v2.0
[AD-3]	4DAtlantic - OHC Experimental Dataset Description v2.0

Table 1 List of applicable documents

1.4. Abbreviations and Acronyms

Synonym	Description
AMOC	Atlantic Meridional Overturning Circulation
ATBD	Algorithm Theoretical Basis Documents
BSC	Barcelona Supercomputing Centre



Ref.: OHCATL_DT_033_MAG Date: 15/05/2025 Issue: 3.0

CCI	Climate Change Initiative program (supported by ESA)
CLIVAR	CLImate VARiability and predictability
CMEMS	Copernicus Marine Environment and Monitoring Service
DA	Applicable document
DOI	Digital Object Identifier
DR	Reference document
ED(D)	Experimental Dataset (Description)
EEH	Expansion Efficiency of Heat
EEA	European Environment Agency
EEI	Earth Energy Imbalance
ESA	European Space Agency
EOEP-5	Earth Observation Envelope Programme-5
EO	Earth Observations
GCOS	Global Climate Observing System
GEWEX	Global Energy and Water Exchanges (https://www.gewex.org/)
GHG	GreenHouse Gas
GMSL	Global Mean Sea Level
GRACE	Gravity Recovery and Climate Experiment
GRACE-FO	GRACE Follow-On
HSSL	Halosteric Sea Level
IPCC	Intergovernmental Panel on Climate Change
ISSI	International Space Science Institute
LEGOS	Laboratoire d'Etudes en Géophysique et Océanographie Spatiales
LOPS	Laboratoire d'Océanographie Physique et Spatiale
MHT	Meridional Heat Transport
MOHeaCAN	Monitoring of the Ocean Heat Content and the eArth eNergy imbalance (ESA project)
MOi	Mercator-Ocean International
NGGM	Next Generation Gravity Mission
NOC	National Oceanography Centre
ODATIS	Ocean Data and Services portal
ОНС	Ocean Heat Content



Date: 15/05/2025

Issue: 3.0

OM	Ocean mass
OMI	Ocean Monitoring Indicator
OSNAP	Overturning in the Subpolar North Atlantic Program
PVR	Product Validation report
RMSD	Root-mean-square deviation
SL	Sea Level
SSL	Steric Sea Level
SPNA	Subpolar North Atlantic
SOW	Statement Of Work
TOA	Top Of Atmosphere
TS	Tender Specification
WB	Western Boundary
WCRP	World Climate Research Programme
WMO	World Meteorological Organization
WP	Work package
WPD	Work Package Description

Table 2 List of Abbreviations and Acronyms

Table 1 List of applicable documents

Table 2 List of Abbreviations and Acronyms

Table 3: Linear trends of the Global Ocean Heat Content time series derived from the 4DAtlantic v3 and in situ products.

1.5. Bibliography

- Bryden, H. L., Johns, W. E., King, B. A., McCarthy, G., McDonagh, E. L., Moat, B. I., and Smeed, D. A.: Reduction in Ocean Heat Transport at 26°N since 2008 Cools the Eastern Subpolar Gyre of the North Atlantic Ocean, J. Clim., 33, 1677–1689, https://doi.org/10.1175/JCLI-D-19-0323.1, 2020.
- Desbruyères, D. G., Sinha, B., McDonagh, E. L., Josey, S. A., Holliday, N. P., Smeed, D. A., New, A. L., Megann, A., and Moat, B. I.: Importance of Boundary Processes for Heat Uptake in the Subpolar North Atlantic, J. Geophys. Res. Oceans, 125, e2020JC016366, https://doi.org/10.1029/2020JC016366, 2020.
- Desbruyères, D. G., Bravo, E. P., Thierry, V., Mercier, H., Lherminier, P., Cabanes, C., Biló, T. C., Fried, N., and Femke De Jong, M.: Warming-to-Cooling Reversal of Overflow-Derived Water Masses in the Irminger Sea During 2002–2021, Geophys. Res. Lett., 49, e2022GL098057, https://doi.org/10.1029/2022GL098057, 2022.



Date: 15/05/2025

Issue: 3.0

 Gaillard, F., Reynaud, T., Thierry, V., Kolodziejczyk, N., and Schuckmann, K. von: In Situ-Based Reanalysis of the Global Ocean Temperature and Salinity with ISAS: Variability of the Heat Content and Steric Height, J. Clim., 29, 1305–1323, https://doi.org/10.1175/JCLI-D-15-0028.1, 2016

- Johnson, G. C. and Lyman, J. M.: Warming trends increasingly dominate global ocean, Nat. Clim. Change, 10, 757–761, https://doi.org/10.1038/s41558-020-0822-0, 2020.
- Kolodziejczyk, N., Prigent-Mazella, A., and Gaillard, F.: ISAS temperature and salinity gridded fields, https://doi.org/10.17882/52367, 2021.
- Levitus, S., Antonov, J. I., Boyer, T. P., Baranova, O. K., Garcia, H. E., Locarnini, R. A., Mishonov, A. V., Reagan, J. R., Seidov, D., Yarosh, E. S., and Zweng, M. M.: World ocean heat content and thermosteric sea level change (0–2000 m), 1955–2010, Geophys. Res. Lett., 39, https://doi.org/10.1029/2012GL051106, 2012.
- Lozier, M. S., Li, F., Bacon, S., Bahr, F., Bower, A. S., Cunningham, S. A., de Jong, M. F., de Steur, L., deYoung, B., Fischer, J., Gary, S. F., Greenan, B. J. W., Holliday, N. P., Houk, A., Houpert, L., Inall, M. E., Johns, W. E., Johnson, H. L., Johnson, C., Karstensen, J., Koman, G., Le Bras, I. A., Lin, X., Mackay, N., Marshall, D. P., Mercier, H., Oltmanns, M., Pickart, R. S., Ramsey, A. L., Rayner, D., Straneo, F., Thierry, V., Torres, D. J., Williams, R. G., Wilson, C., Yang, J., Yashayaev, I., and Zhao, J.: A sea change in our view of overturning in the subpolar North Atlantic, Science, 363, 516–521, https://doi.org/10.1126/science.aau6592, 2019.
- Mercier, H., Lherminier, P., Sarafanov, A., Gaillard, F., Daniault, N., Desbruyères, D., Falina, A., Ferron, B., Gourcuff, C., Huck, T., and Thierry, V.: Variability of the meridional overturning circulation at the Greenland-Portugal OVIDE section from 1993 to 2010, Prog. Oceanogr., 132, 250–261, https://doi.org/10.1016/j.pocean.2013.11.001, 2015.
- Piecuch, C. G., Ponte, R. M., Little, C. M., Buckley, M. W., and Fukumori, I.: Mechanisms underlying recent decadal changes in subpolar North Atlantic Ocean heat content, J. Geophys. Res. Oceans, 122, 7181–7197, https://doi.org/10.1002/2017JC012845, 2017.
- Roemmich, D., Alford, M. H., Claustre, H., Johnson, K., King, B., Moum, J., Oke, P., Owens, W. B., Pouliquen, S., Purkey, S., Scanderbeg, M., Suga, T., Wijffels, S., Zilberman, N., Bakker, D., Baringer, M., Belbeoch, M., Bittig, H. C., Boss, E., Calil, P., Carse, F., Carval, T., Chai, F., Conchubhair, D. Ó., d'Ortenzio, F., Dall'Olmo, G., Desbruyeres, D., Fennel, K., Fer, I., Ferrari, R., Forget, G., Freeland, H., Fujiki, T., Gehlen, M., Greenan, B., Hallberg, R., Hibiya, T., Hosoda, S., Jayne, S., Jochum, M., Johnson, G. C., Kang, K., Kolodziejczyk, N., Körtzinger, A., Traon, P.-Y. L., Lenn, Y.-D., Maze, G., Mork, K. A., Morris, T., Nagai, T., Nash, J., Garabato, A. N., Olsen, A., Pattabhi, R. R., Prakash, S., Riser, S., Schmechtig, C., Schmid, C., Shroyer, E., Sterl, A., Sutton, P., Talley, L., Tanhua, T., Thierry, V., Thomalla, S., Toole, J., Troisi, A., Trull, T. W., Turton, J., Velez-Belchi, P. J., Walczowski, W., Wang, H., Wanninkhof, R., Waterhouse, A. F., Waterman, S., Watson, A., Wilson, C., Wong, A. P. S., Xu, J., and Yasuda, I.: On the Future of Argo: A Global, Full-Depth, Multi-Disciplinary Array, Front. Mar. Sci., 6, 2019.
- Yashayaev, I. and Loder, J. W.: Recurrent replenishment of Labrador Sea Water and associated decadal-scale variability, J. Geophys. Res. Oceans, 121, 8095–8114, https://doi.org/10.1002/2016JC012046, 2016.



Date: 15/05/2025

Issue: 3.0

2. Validation on RAPID-MOCHA section (V1.0)

2.1. Overview

Following the product validation plan detailed in the 4DAtlantic project proposal [AD1] an assessment of satellite-based ocean heat content estimates produced by the 4DAtlantic consortium was performed at Test Site 1 consisting of the Subtropical North Atlantic, defined here as comprised between latitudes 20°N and 40°N. The validation was performed against in-situ data from the NOC ARGO OI dataset, as well as from the RAPID-MOCHA mooring array. The assessment focuses on how well the 4DAtlantic product captures the spatial and temporal variability of ocean heat content in the Subtropical North Atlantic at both annual and inter-annual timescales. In addition, a comparison of long-term trends of ocean heat content estimates reported by the space-based approach and in-situ instruments is carried out. Finally, uncertainty information (local variance/covariance matrices) provided in the novel 4DAtlantic product is used to assess statistical difference between the novel space geodetic estimates and existing in-situ data.

2.2. Data and methods

2.2.1. Datasets

2.2.1.1. 4DAtlantic

This report focuses on the analysis of versions v0.2 and v0.4 of the novel satellite-based ocean heat content (OHC) estimates produced by the 4DAtlantic scientific consortium. An initial analysis was performed of version v0.3 of the product with findings presented to the science partners; an issue was found in the timings of the seasonal cycles and therefore no further analysis was conducted. Version v0.2 of the product is available at spatial resolutions of 1° and 3° (of which, the 1° version is analysed here), at a temporal resolution of 30 days. The v0.2 product includes data for the period August 2002 - December 2020 and provides depth-integrated OHC estimates between 0-2000m. The v0.2 product used a different reference surface to the other products and thus re-scaling was required. This was done as follows:

$$OHC(lat, lon) = \frac{OHC_p(lat, lon)*surf_{ref}}{Area(lat, lon)}$$
 (eq. 1)

where OHC_p is the OHC data as found in the v0.2 product, $Area_{(lat,lon)}$ is the area in m² of each grid cell, and:



Date: 15/05/2025

Issue: 3.0

$$surf_{ref} = 4\pi (R + h_{TOA})^2$$
 (eq. 2)

where R is the Earth's radius and h_{TOA} is the reference height at the top of the atmosphere defined at an altitude of 20km above the surface.

The v0.4 product is generated on a spatial grid with 1° resolution and at a temporal resolution of 30 days. This newer version includes data for the period April 2002 - December 2020, and provides full-depth estimates of integrated ocean heat content as it also includes contributions from the deep sea.

2.2.1.2. NOC ARGO optimally interpolated (OI) data

The NOC ARGO OI dataset is a gridded product generated by the NOC using optimal interpolation of ARGO float profile data including temperature and salinity. The spatial resolution of NOC ARGO OI is 1° in latitude/longitude and 20m in depth, whereas the temporal resolution of the product is 10 days. In-situ estimates of depth-integrated ocean heat content were computed from the gridded temperature and salinity ARGO OI dataset using thermodynamic routines included in the Gibbs SeaWater (GSW) oceanographic library, and then integrated over the depths 0-2000m. OHC estimates computed using the NOC ARGO OI temperature/salinity dataset are currently available between April 2004 and September 2021.

2.2.1.3. RAPID-MOCHA array data

The RAPID programme aims to study the Atlantic Meridional Overturning Circulation (AMOC) using an array of moored instruments at a latitude of ~26.5°N measuring temperature, salinity, and current velocities from the near surface to the sea-floor. Raw instrument mooring data are processed at the NOC and made publicly available as a gridded product, with a 20m spatial resolution, and a 12-hour temporal resolution. Gridded RAPID data currently spans the period comprised between April 2004 and March 2020. Temperature-salinity instrument data are further combined from moorings located at the western and eastern regions of the array to create merged profiles of temperature and salinity at the Western and at the Eastern boundary, respectively. In this study, full-depth temperature/salinity data reported by the MAR-West mooring located west of the Mid-Atlantic Ridge (MAR) were also used. Additional processing of RAPID gridded data was carried out to reconstruct the full OHC field and compute depth-integrated estimates of OHC across the whole RAPID section for comparison with the 4DAtlantic OHC products (see Section 2.2.2.3.2 for details).

2.2.2. Method

2.2.2.1. Trend analysis

A linear regression approach was used to estimate values for trends and seasonal cycles in the NOC ARGO and 4DAtlantic datasets on three spatial scales, the entire Subtropical North Atlantic (20° N - 40° N) region, basin-wide 5° -latitudinal section across the Subtropical North Atlantic, and on an individual grid cell basis (1°). Trends were estimated using a Generalised Least Squares (GLS) approach with additional terms to model the seasonal cycle and temporal autocorrelation within the data:



Date: 15/05/2025

Issue: 3.0

$$OHC \sim \beta_0 + \beta_1 t + \beta_2 s + \epsilon_t$$
 (eq. 3)

where t is time, s is a seasonal factor (running from 1 to 12 for the monthly 4DAtlantic datasets, and from 1 to 37 for the 10-day ARGO dataset), β_n are regression coefficients and ϵ_t represents the error terms including auto-correlation:

$$\epsilon_t = \rho \epsilon_{t-1} + \omega_t$$
 (eq. 4)

For comparison between the NOC ARGO OI-derived and 4DAtlantic OHC datasets, which span different timeframes, trends were estimated over a common time period, from the start of the ARGO dataset to the end of the 4DAtlantic datasets (i.e. from April 2004 until December 2020). Initial analysis suggested the presence of potential temporal discontinuities in the data, as such a mean-shift changepoint detection using the "At Most One Change" algorithm was applied to de-seasonalised time series to determine if there was consistency in the timings of potential changepoints between the datasets (Killick & Eckley, 2014).

2.2.2.2. Uncertainty analysis

The 4DAtlantic v0.4 product includes local variance-covariance matrices of OHC data for each 1° grid cell. These matrices have dimensions of 19×19 , where 19 is the number of years in the 4DAtlantic dataset. represented by a 19×19 matrix in each grid cell. As the NOC ARGO OI product length was shorter, only the last 17 matrix elements of each grid cell in each dimension were used (representing the common time period). These matrices allow calculation of the OHC trend uncertainty as detailed in the 4DAtlantic-OHC ATBD [AD2]. Accordingly, these were calculated at NOC using the local variance-covariance matrices in the 4DAtlantic v0.4 product. These were then used to test whether the ARGO trend was significantly different from the 4DAtlantic trend on a grid cell by grid cell basis (this was done at a 2σ significance level). No information is available for NOC ARGO OI uncertainties, so the test determines whether the ARGO trend (a mean) lies within the confidence intervals of the 4DAtlantic product.

2.2.2.3. RAPID-MOCHA processing

2.2.2.3.1. Estimation of OHC at the mooring locations

Similarly to the approach used for NOC ARGO OI described above, in-situ estimates of OHC from individual moorings were obtained from the RAPID temperature/salinity gridded dataset. OHC of vertical cells was then integrated from surface to sea-floor to obtain depth-integrated OHC at each mooring location.

2.2.2.3.2. Estimation of OHC across the section

Obtaining spatially averaged estimates of OHC across the RAPID array is challenging because the moorings are located in such a way that large portions of the ocean along 26.5°N are left unsampled. To address this challenge, we began by splitting the ocean along 26.5°N into two zonal sections demarcated by the full-depth profiles at the Eastern and Western boundaries as well as at the mooring located West of the Mid Atlantic Ridge (see Figure 12). The goal is to obtain estimates of zonally averaged ocean heat



Date: 15/05/2025

Issue: 3.0

content over each section. Mathematically, such estimates can be obtained by first calculating areal density of OHC along the section:

$$h(x) = \int_{-H}^{0} C_p \rho(x, z) T(x, z) dz$$
 (eq. 5)

where h(x) is the areal density of OHC (units: Jm^{-2}), Cp is the specific heat capacity of seawater, $\varrho(x, z)$ is seawater density, T(x, z) is the temperature of seawater, and H is the depth of the ocean bottom.

Then we proceed by zonally integrating h(x) to compute the zonally-averaged OHC, per unit length, where x_1 and x_2 are the locations of the western and eastern boundaries of the section, respectively.

$$OHC = \frac{1}{x_2 - x_1} \int_{x_1}^{x_2} h(x) dx$$
 (eq. 6)

Only the value of h(x) at the boundaries of the section is known, namely $h(x_1)$ and $h(x_2)$, but to compute the zonal integral we need to know the value of h(x) at each point inside the zonal section. Hence, we need a way of approximating h(x), and thus the zonal integral.

To this aim, we compute h(x) inside each of the two sections using the NOC Argo OI data set and then we calibrate it against RAPID observations. Here we assume that the h(x) derived from Argo OI is equal to the true value except for an additive bias. That is,

$$h_{true}(x) = a + h_{OI}(x),$$
 (eq. 7)

where the additive bias can be estimated from the RAPID data as:

$$a = \frac{h_{Rapid}(x_2) + h_{Rapid}(x_1)}{2} - \frac{h_{OI}(x_2) + h_{OI}(x_1)}{2}$$
 (eq. 8)

2.3. Results

2.3.1. Validation against NOC ARGO OI

2.3.1.1. 4DAtlantic v0.2

2.3.1.1.1. Regional average trends

Figure 2 shows regional average OHC time series for the 4DAtlantic v0.2 and NOC ARGO OI products. From this we can see a match in the timing of the seasonal cycles but that the two products have different amplitudes (4DAtlantic v0.2: 1.0×10^9 Jm⁻², NOC ARGO OI: 0.6×10^9 Jm⁻²). In terms of temporal evolution similarity is shown in terms of the pattern of interannual variability, additionally the linear trends both show an increase over time, although the 4DAtlantic product has a greater magnitude



Date: 15/05/2025

Issue: 3.0

(4DAtlantic v0.2 trend: 4.6 Wm⁻², NOC ARGO OI trend: 2.3 Wm⁻²). Some evidence of a discontinuity is seen in late 2013 in the 4DAtlantic product, whereby a rapid increase is observed. However, changepoint analysis (Figure 3) shows that there is statistical evidence of this temporal discontinuity in both the NOC ARGO OI and the 4DAtlantic v0.2 datasets, which indicates the presence of a possible geophysical signal, or the results of temporal autocorrelation.

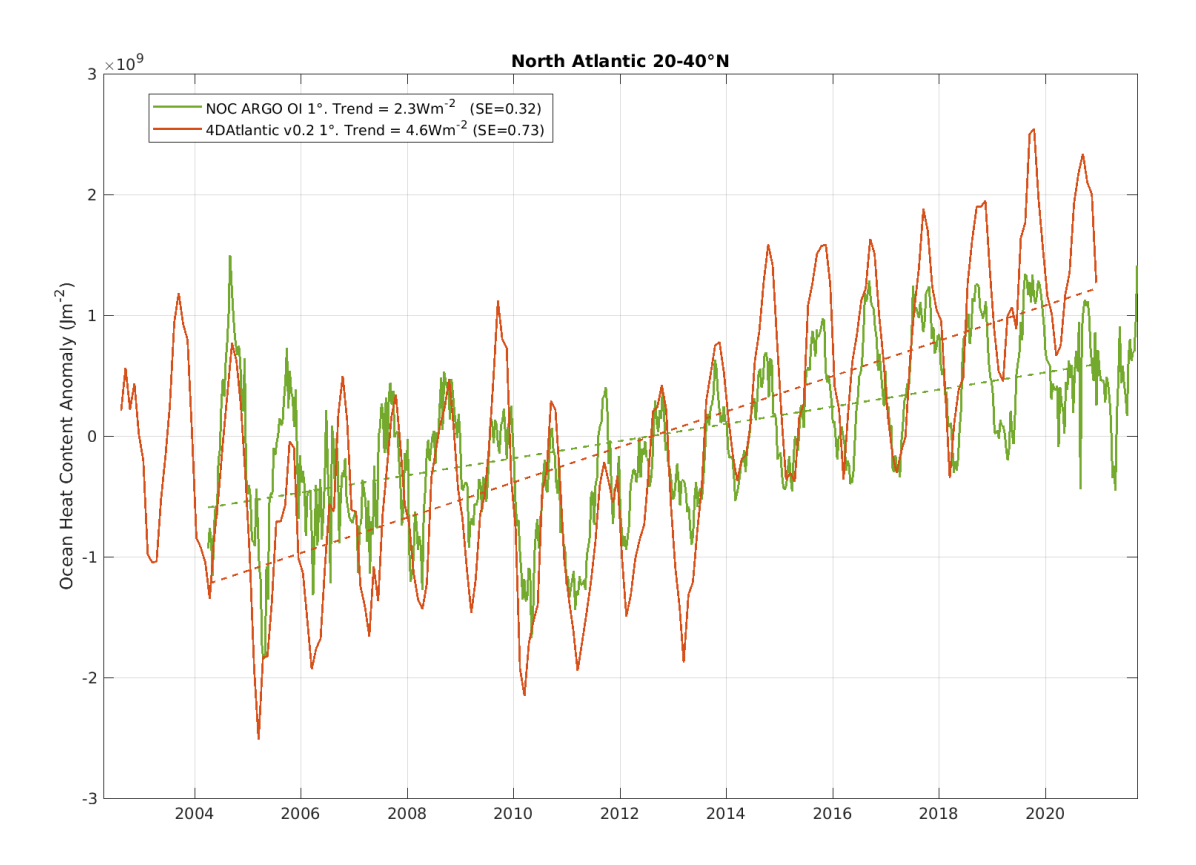


Figure 2: Average OHC time series for the entire Subtropical North Atlantic region, showing the NOC ARGO OI (green) and 4DAtlantic v0.2 (orange) products. The dashed lines represent the linear trend for the respective datasets



Date: 15/05/2025

Issue: 3.0

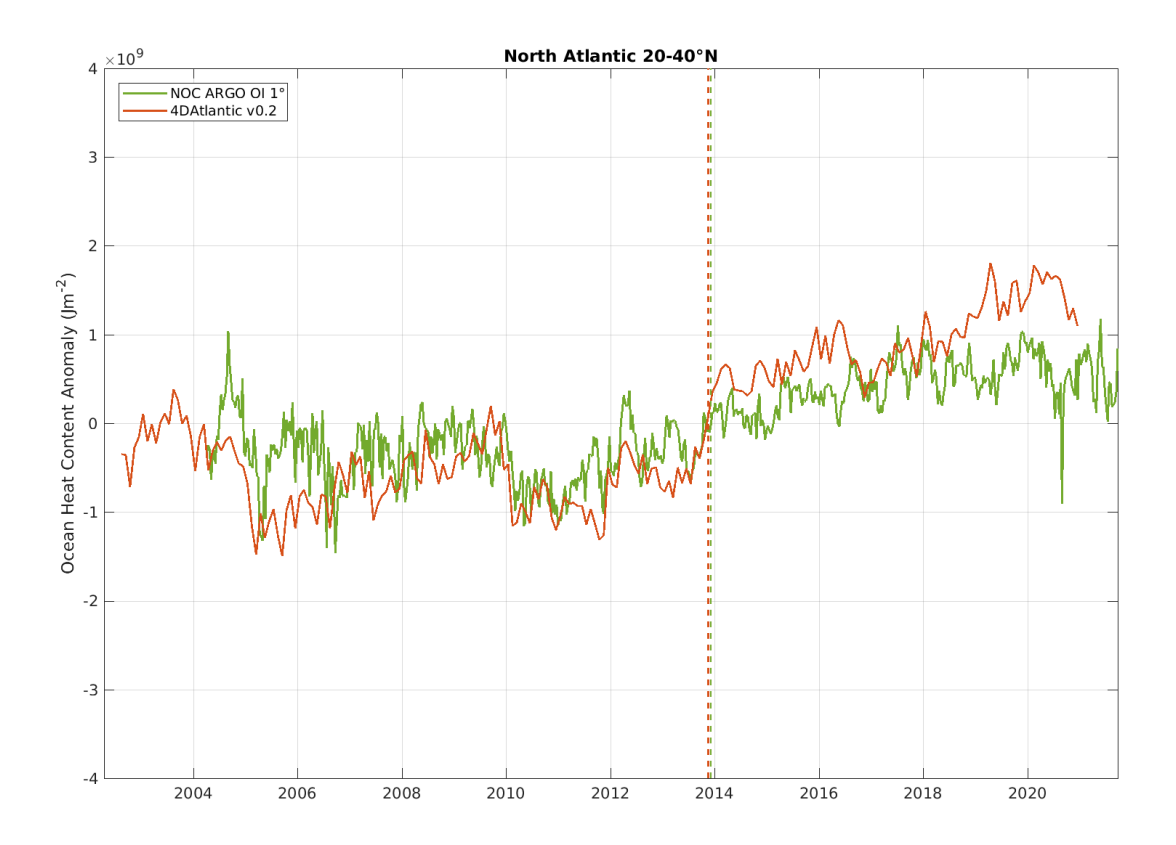


Figure 3: Average OHC time series (de-seasonalised) for the entire Subtropical North Atlantic region, showing the NOC ARGO OI (green) and 4DAtlantic v0.2 (orange) products. The dashed vertical lines represent the location of potential changepoints identified using the At-Most-One-Change approach.

2.3.1.1.2. Latitudinal average trends

To compare the two products latitudinally, both datasets were split into basin-wide 5°- latitudinal bands prior to additional trend analysis (Figure 4). In this we can see that for both datasets the trend magnitude and seasonal cycle amplitude increase towards high latitudes. It can also be seen that the seasonal cycle amplitude and trend magnitude are greater in the 4DAtlantic v0.2 product, with the trend values appearing to be most similar in the lowest latitude division (20°N-25°N).



Ref.: OHCATL_DT_033_MAG Date: 15/05/2025

Issue: 3.0

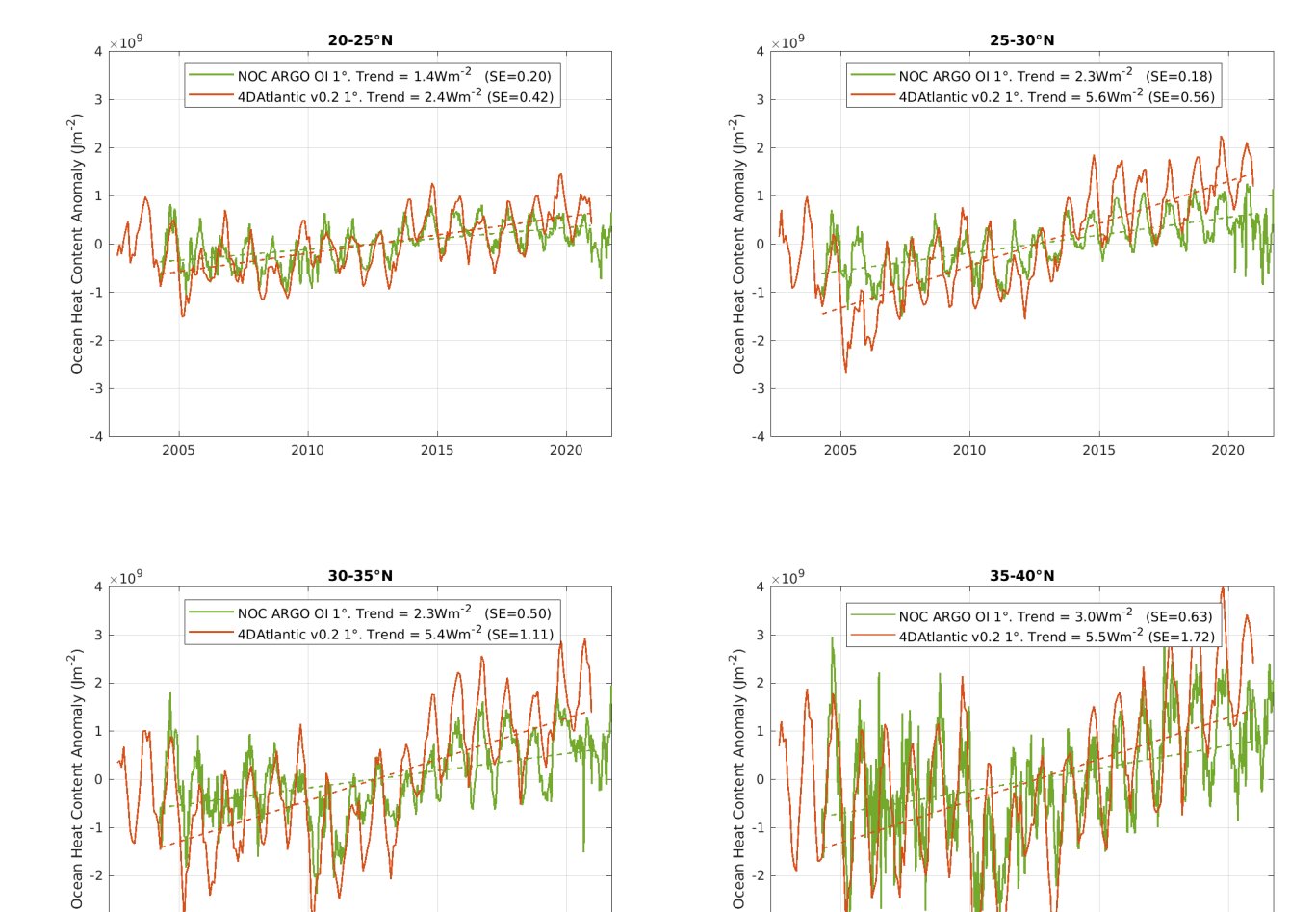


Figure 4: Average OHC time series in 5° latitudinal bands of the Subtropical North Atlantic region for the NOC ARGO OI (green) and 4DAtlantic v0.2 (orange) products. The dashed lines represent the linear trend for the respective datasets.

2005

2010

2015

2020

2020

2.3.1.1.3. Trend spatial distribution

2010

2015

2005

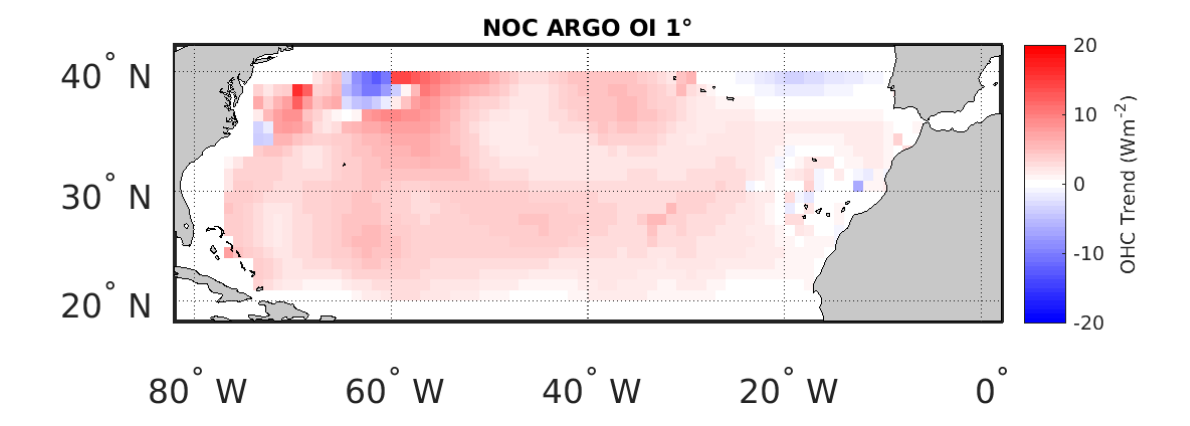
OHC trends estimated in each 1° grid cell are shown in Figure 5. Overall patterns are similar for the NOC ARGO OI and 4DAtlantic v0.2 datasets, with generally positive trends over the region, with the strongest positive trends, as well as the strongest negative trends, in the Northwest for both datasets. However, some dissimilarities are also seen. For example, in the NOC ARGO OI product there are regions of negative trends in the Northeast and East of the Subtropical North Atlantic, which are not present in the



Date: 15/05/2025

Issue: 3.0

4DAtlantic v0.2 dataset. Additionally, over the majority of the region, the trend magnitudes are greater in the 4DAtlantic v0.2 product, consistent with Figure 2 & Figure 4.



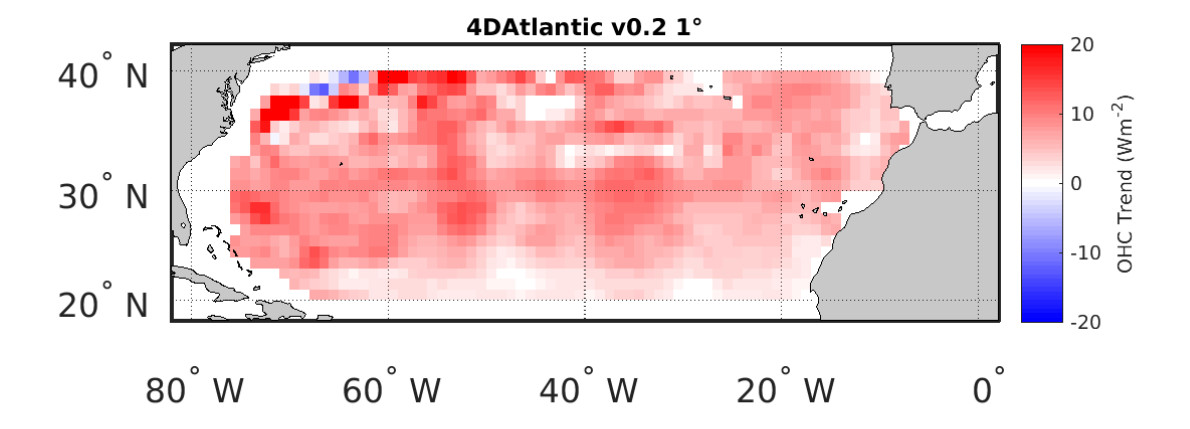


Figure 5: OHC trends in each 1° grid cell of the Subtropical North Atlantic region for NOC ARGO OI (top) 4DAtlantic v0.2 (bottom) products.

2.3.1.2. 4DAtlantic v0.4

2.3.1.2.1. Region average trends

Figure 6 shows regional average time series for the 4DAtlantic v0.4 and NOC ARGO OI datasets. The timing of the seasonal cycles is shown to match in both datasets, which was not seen in the interim 4DAtlantic v0.3 product (not shown). The amplitude of the season cycles in the 4DAtlantic v0.4 product shows better agreement with the NOC ARGO OI product than did the 4DAtlantic v0.2 product, albeit the 4DAtlantic product still has slightly larger amplitudes (4DAtlantic v0.4: 0.8x10⁹ Jm⁻², NOC ARGO OI:



Date: 15/05/2025 Issue: 3.0

0.6x10⁹ Jm⁻²). The overall pattern of interannual variability is similar, although after 2018 the 4DAtlantic product seems to become higher than the ARGO product. Likewise, the magnitude of the linear trends is now in closer agreement, albeit still of greater magnitude in the 4DAtlantic v0.4 product (4DAtlantic v0.4: 2.9 Wm⁻², NOC ARGO OI: 2.3 Wm⁻²), possibly caused by the discrepancy after 2018. The differences between the two datasets may be partially connected to the different depth profiles of the two products, the 4DAtlantic v0.4 product represents OHC for the full ocean depth, but the NOC ARGO OI only represents the top 2000m. More limited visual evidence is shown for a discontinuity in 2013 when compared to the v0.2 product; change point analysis again showed statistical evidence of a step at this time, present in both the NOC ARGO OI and 4DAtlantic v0.4 datasets (Figure 7).

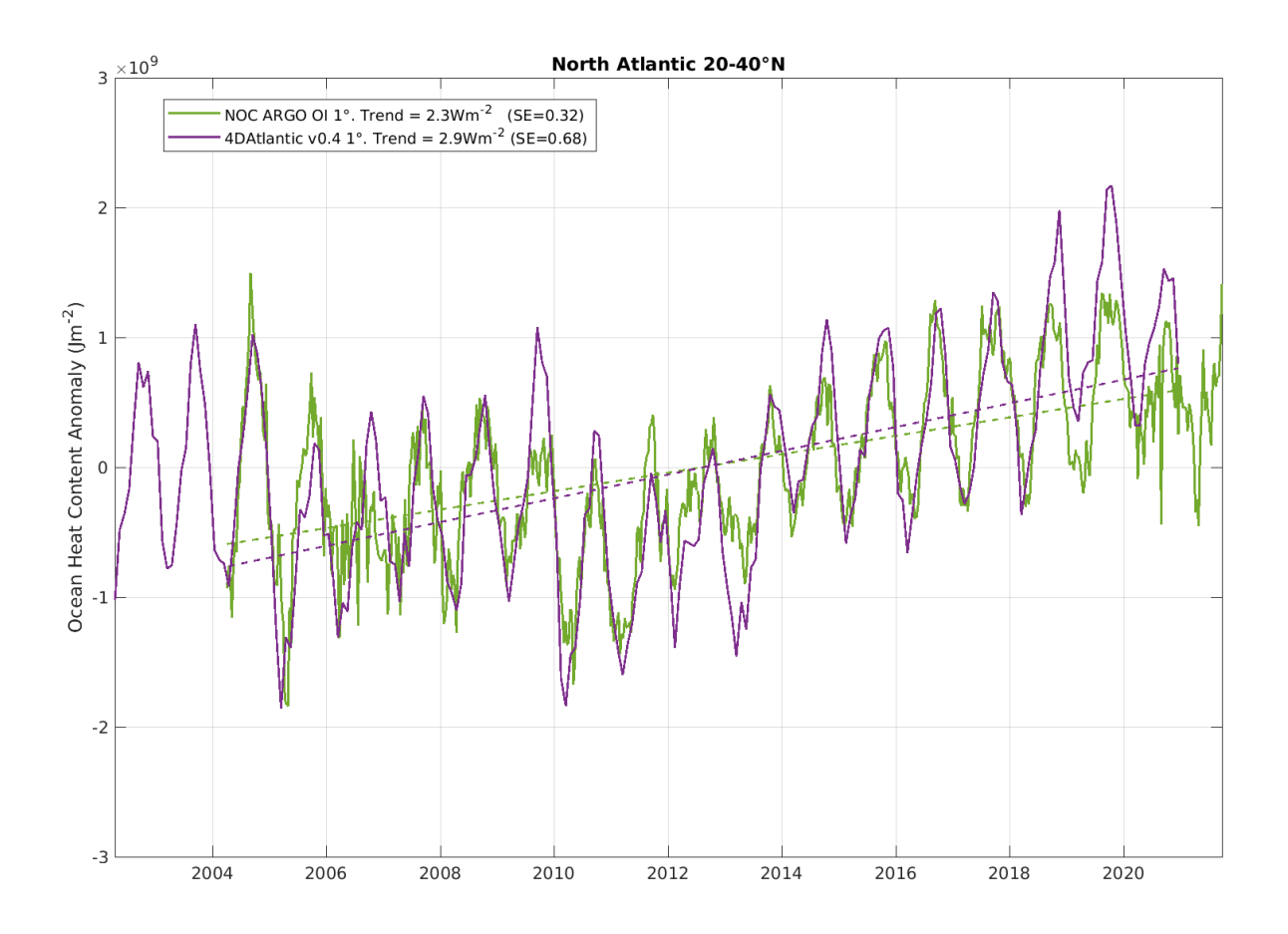


Figure 6: Average OHC time series for the entire Subtropical North Atlantic region, showing the NOC ARGO OI (green) and 4DAtlantic v0.4 (purple) products. The dashed lines represent the linear trend for the respective datasets.



Date: 15/05/2025

Issue: 3.0

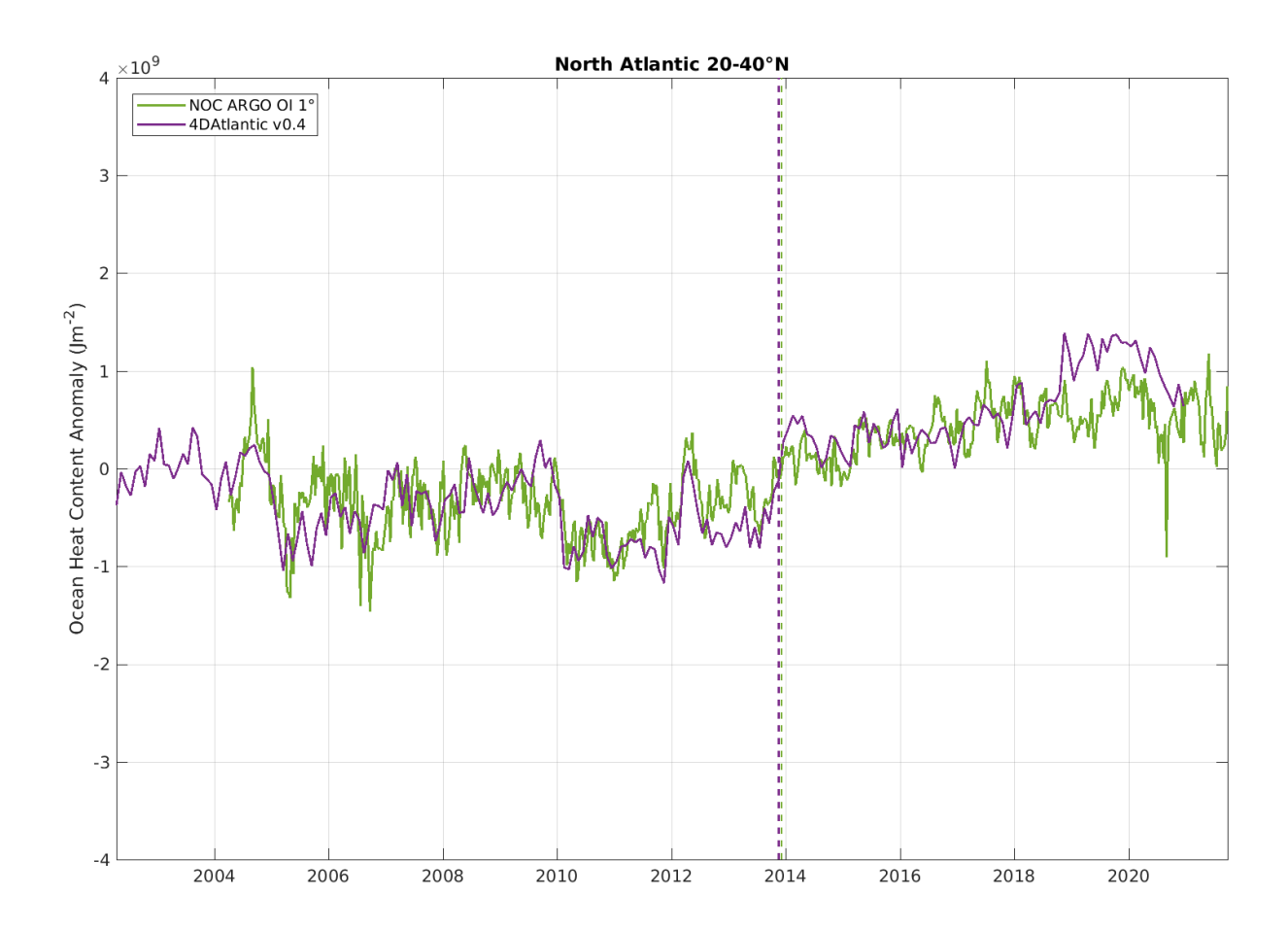


Figure 7: Average OHC time series (de-seasonalised) for the entire Subtropical North Atlantic region, showing the NOC ARGO OI (green) and 4DAtlantic v0.4 (purple) products. The dashed vertical lines represent the location of potential changepoints identified using the At-Most-One-Change approach.

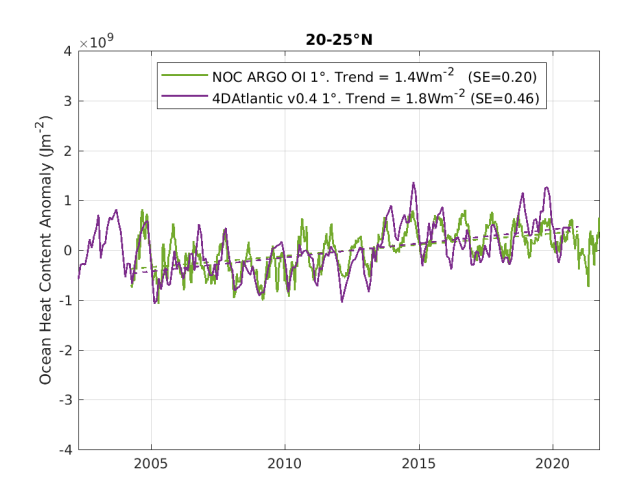
2.3.1.2.2. Latitudinal average trends

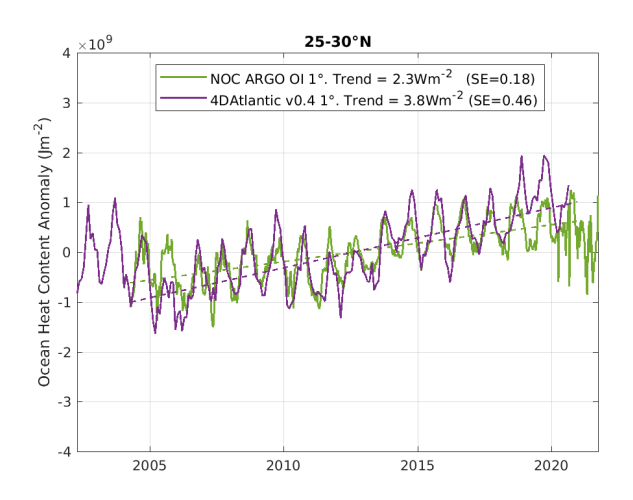
Trends averaged over 5° latitudinal bands are shown in Figure 8. As in the analysis of the 4DAtlantic v0.2 product, the NOC ARGO OI and 4DAtlantic v0.4 products both show increased trend magnitude and seasonal cycle amplitude towards high latitude. The 4DAtlantic v0.4 product is shown to be in closer agreement with the NOC ARGO OI dataset. In the $20^{\circ}N-25^{\circ}N$ and $35^{\circ}N-40^{\circ}N$ latitudinal bands the trends are found to be near identical, only in the latitudinal bands between these are the 4Datlantic v0.4 trends still found to be higher.

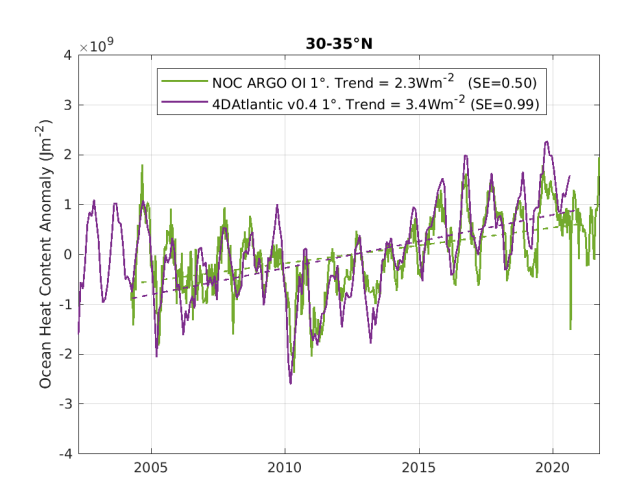


Date: 15/05/2025

Issue: 3.0







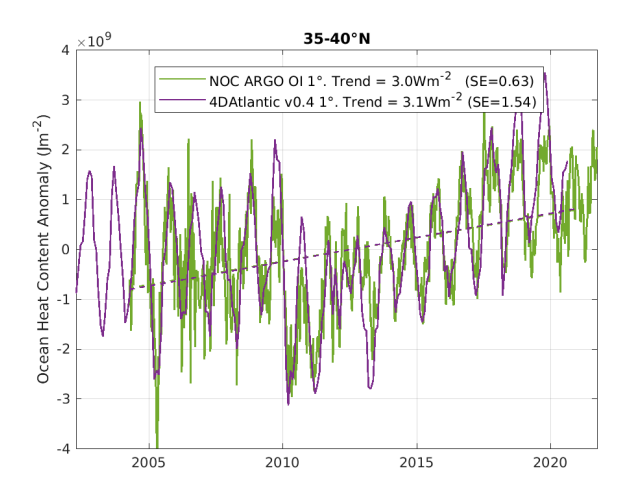


Figure 8: Average OHC time series in 5° latitudinal bands of the Subtropical North Atlantic region for the NOC ARGO OI (green) and 4DAtlantic v0.4 (purple) products. The dashed lines represent the linear trend for the respective datasets.

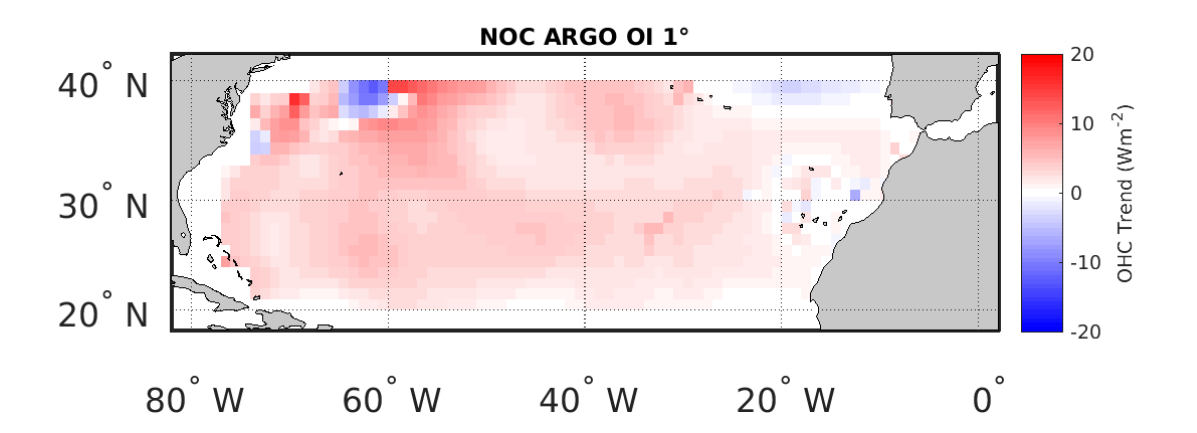
2.3.1.2.3. Trend spatial distribution

OHC trends estimated in each 1° grid cell of the NOC ARGO OI and 4DAtlantic v0.4 datasets are shown in Figure 9. Overall patterns are very similar with an overall positive trend, strongest positive trends in the Northwest, as well as areas of negative trends in the Northwest and Northeast in both datasets. Additionally, the average magnitude of the 4DAtlantic v0.4 dataset has been reduced and is now closer to the NOC ARGO OI dataset, although it still appears to be higher, particularly at latitudes at the centre of the analysed region.



Date: 15/05/2025

Issue: 3.0



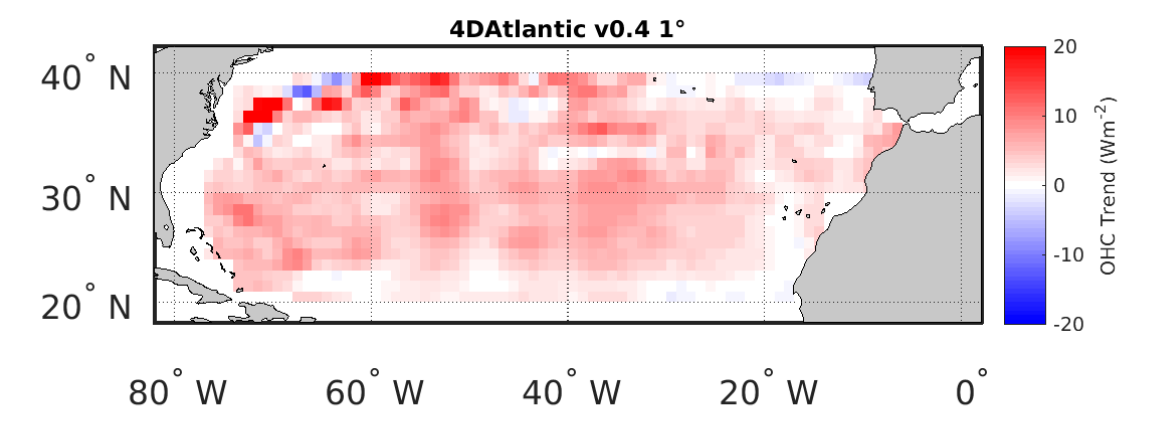


Figure 9: OHC trends in each 1° grid cell of the Subtropical North Atlantic region for NOC ARGO OI (top) 4DAtlantic v0.4 (bottom) products.

To assess the significance of the 4DAtlantic v0.4 trends compared to the NOC ARGO OI dataset, significance testing was performed using trend uncertainties calculated from the local variance-covariance matrices provided in the 4DAtlantic v0.4 product. A map showing this binary significance check in each 1° grid cell, indicating whether trends reported by NOC ARGO OI and 4DAtlantic v0.4 trends are significantly different or not, is shown in Figure 10. Finally, a map of trends after the removal grid cells considered to be significantly different is shown in Figure 11. The greatest areas of difference are at latitudes at the centre of the analysed region, particularly at longitudes towards the centre of the Atlantic. Furthermore, the large positive trends in the Northwest of the region are largely found to be significantly different from NOC ARGO OI product, despite both datasets tending to have larger positive trends here.



Date: 15/05/2025

Issue: 3.0

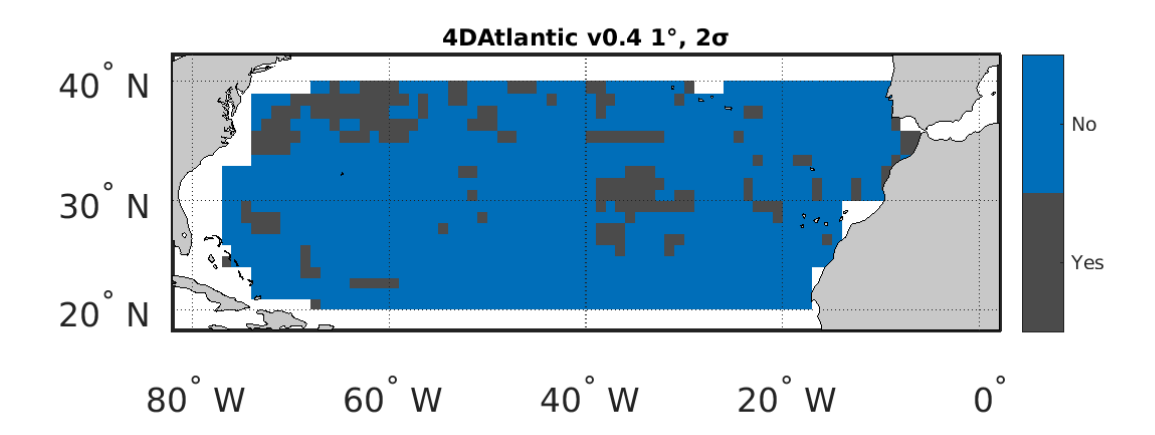


Figure 10: Map of the Subtropical North Atlantic region showing where the NOC ARGO OI OHC trends are significantly different from the 4DAtlantic v0.4 trends at a 2σ significance level. Maps of 4DAtlantic v0.4 OHC trends with this mask applied can be seen in Figure 11.

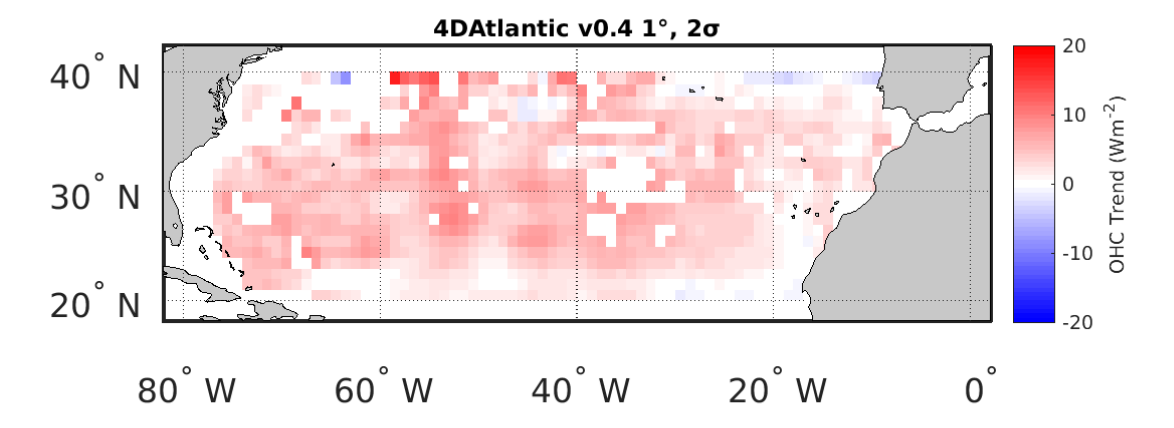


Figure 11: OHC trends in each 1° grid cell of the Subtropical North Atlantic region for the 4DAtlantic v0.4 product. Where a trend is significantly different from ARGO (c.f. Figure 9 and Figure 10) it is treated as zero (i.e. white).

2.3.2. Validation against the RAPID-MOCHA array

An assessment of the 4DAtlantic OHC product was carried out using verification data from the RAPID-MOCHA mooring array located in the subtropical North Atlantic at a latitude of 26.5° N. Figure 12 shows the locations of the RAPID moorings with blue arrows indicating the ones used in this study.



Date: 15/05/2025

Issue: 3.0

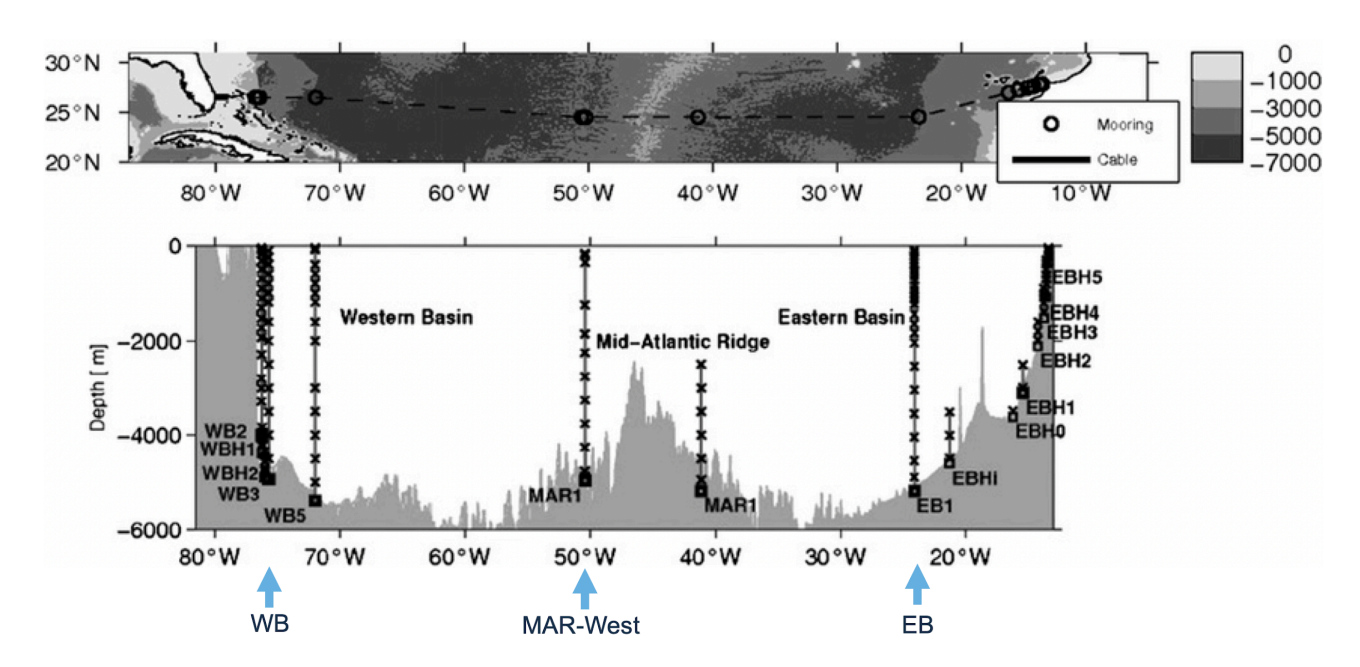


Figure 12: Schematic showing the name, location, and vertical extent of the RAPID-MOCHA moorings. Blue arrows indicate moorings used in this study, Western Boundary (WB) left, Mid Atlantic Ridge West (MAR-West) middle, Eastern Boundary (EB) right.

2.3.2.1. Validation at mooring locations

Three different locations were analysed, namely the average of the Western Boundary (WB), the mooring west of the Mid-Atlantic Ridge (MAR-West) and the average of the Eastern Boundary (EB) indicated by the blue arrows on the left, middle and right on the bottom of Figure 12, respectively.

OHC anomalies computed at these mooring locations are presented in Figure 13 and show that OHC increases in time at all three locations over the period under study, albeit at different rates, with the EB moorings reporting a steeper trend with respect to the WB moorings.



Date: 15/05/2025

Issue: 3.0

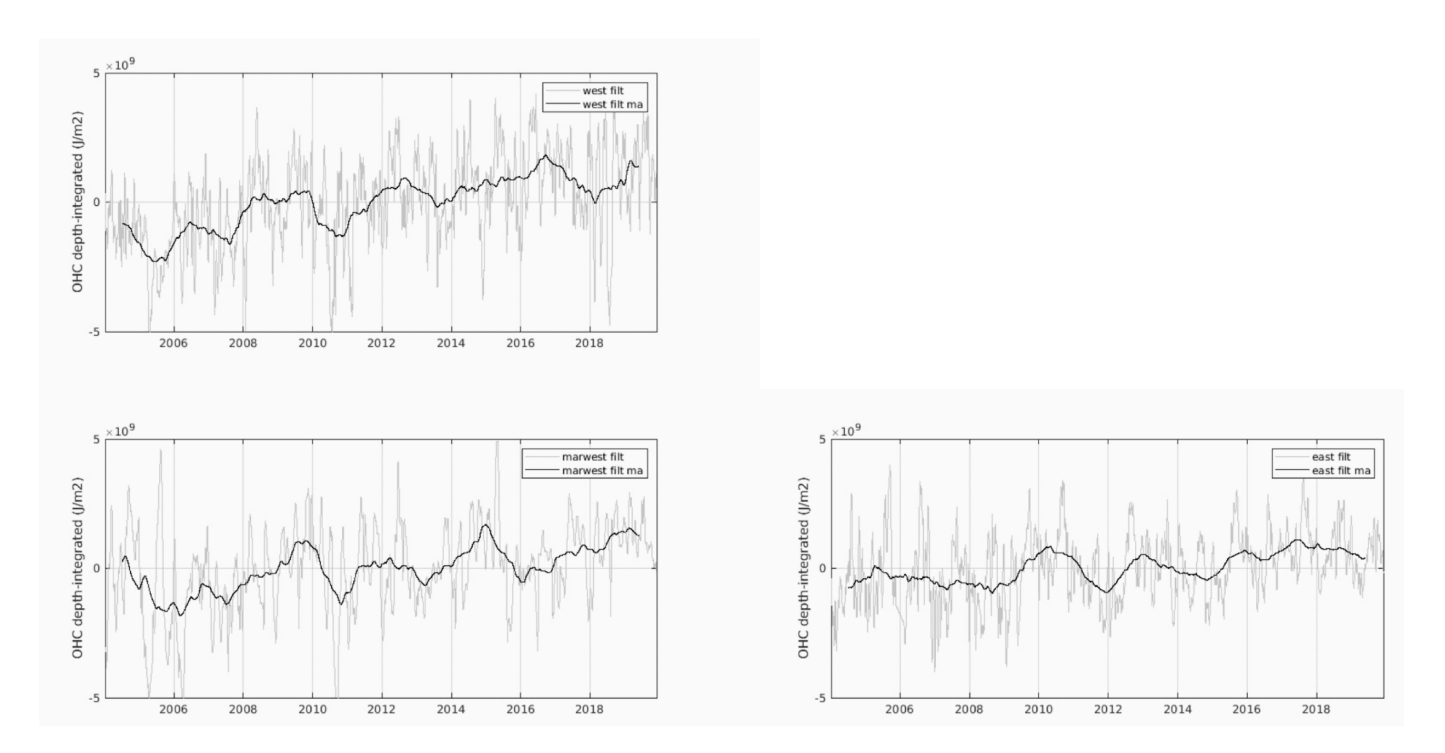


Figure 13: Temporal evolution of depth-integrated OHC anomaly computed at the RAPID-MOCHA mooring location using a 10-day low-pass filter (grey) and a 1-year moving average (black), for the average of the Western boundary (top, left), the mooring west of the Mid-Atlantic Ridge (bottom, left) and the average of the Eastern boundary (bottom, right).

We proceeded then with evaluating OHC anomalies at the same locations using 4DAtlantic v0.2, 4DAtlantic v0.4, and NOC ARGO OI for completeness. In general, the results presented in Figure 14 show an increasing OHC trend at all locations for RAPID, both version of 4DAtlantic, and for ARGO as well; with the Western boundary area being characterised by a faster OHC increase rate than the Eastern region.



Date: 15/05/2025

Issue: 3.0

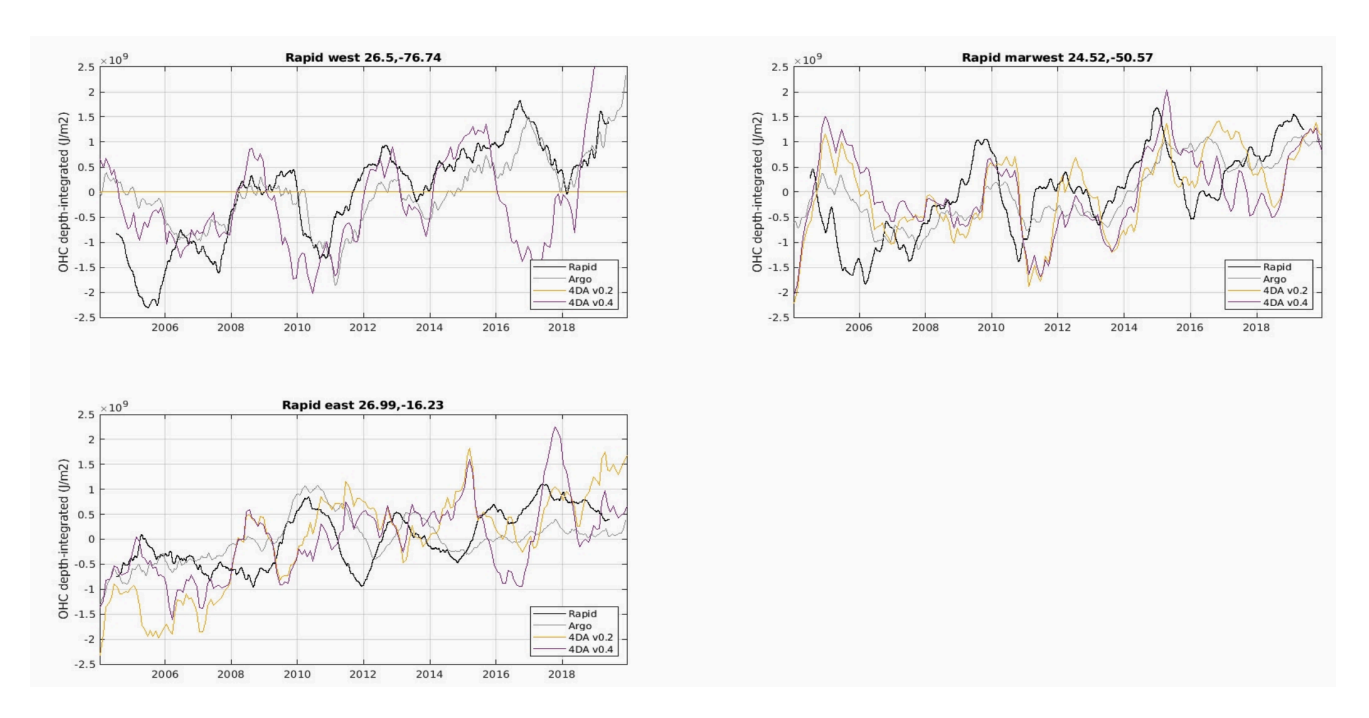


Figure 14: Temporal evolution of depth-integrated OHC anomaly at the mooring locations estimated from RAPID (black), NOC ARGO OI (grey), 4DAtlantic v0.2 (yellow) and 4DAtlantic v0.4 (purple), for the average of the Western boundary (top, left), the mooring west of the Mid-Atlantic Ridge (bottom, left) and the average of the Eastern boundary (bottom, right).

Findings at the WB presented in the top left plot show that no data are found in 4DAtlantic v0.2 at this RAPID mooring location (26.5° N, 76.74° W; plot top left), likely because of the proximity to the coast line, and associated possible lack of reliable Integrated Expansion Efficiency of Heat (IEEH) information in that grid cell. Using 4DAtlantic v0.4, we find instead that a meaningful OHC signal is found, which shows that the most recent version of the space geodetic product covers a larger area of the ocean, including grid cells in closer proximity of land.

A closer look at the WB results reveals that temporal correlation between RAPID (black) and 4DAtlantic v0.4 (purple) is generally good, although in some periods (2016-2018) the two trends actually appear to be anti-correlated. On the other hand, we observe that RAPID and ARGO (grey) are typically temporally well correlated, including the period 2016-2018. Agreement in terms of magnitude of the OHC anomaly is generally good, with some temporal variability, see e.g. the time frame 2004-2006 where a dip is reported by RAPID at the EB whereas ARGO appears more stable, possibly an effect of the optimal interpolation process of float profile data.

Inspection of results found at the MAR-West location (24.52° N, 50.57° W; plot top right) similarly reveals good temporal correlation and similar magnitudes between RAPID and 4DAtlantic, with some exceptions. Again, the mooring reports a dip in 2004-2006 which only appears later on (lag \sim 1 year) in both the 4DAtlantic and ARGO timeseries. Similar delays appear later on, see e.g. the RAPID peak of 2009-2010 which is similar in magnitude and duration to the 4DAtlantic and ARGO OHC peak of 2010-2011. The reason behind this apparent lag is unclear at present and may be potentially related to processing of float profiles, including spatial interpolation.

At the Eastern boundary (26.99 °N, 16.23 °W, plot bottom left), we observe a relatively smaller OHC increase, with good agreement between RAPID and 4DAtlantic trends, especially with the later version



Date: 15/05/2025

Issue: 3.0

v0.4. In terms of temporal correlation, we typically find good correspondence between RAPID and ARGO, less so with 4DAtlantic where a similar lag effect as described above is also found at the EB.

2.3.2.2. Experimental versions of 4DAtlantic (v0.4-ECCO, v0.4-Mascon)

For completeness, a comparative analysis of the experimental 4DAtlantic products was also performed.

Figure 15 (top left) displays findings at the WB moorings, including all 4DAtlantic versions available at the time of writing. We find that temporal agreement with RAPID does not appear to vary much between different version of the 4DAtlantic dataset, including the experimental ones. On the other hand, OHC scales of variability reported by the v0.4-Mascon sometimes appear to provide better agreement with RAPID than version v0.4, whereas discrepancies between v0.4-ECCO and RAPID are at times higher than v0.4 (see e.g. the 4DAtlantic peak of 2008-2009), although this behaviour is not always consistent across the whole timeseries.

Similar conclusions can be derived from inspection and comparison of the OHC temporal evolutions at the MAR-West mooring (top right), and at the Eastern boundary (bottom left).

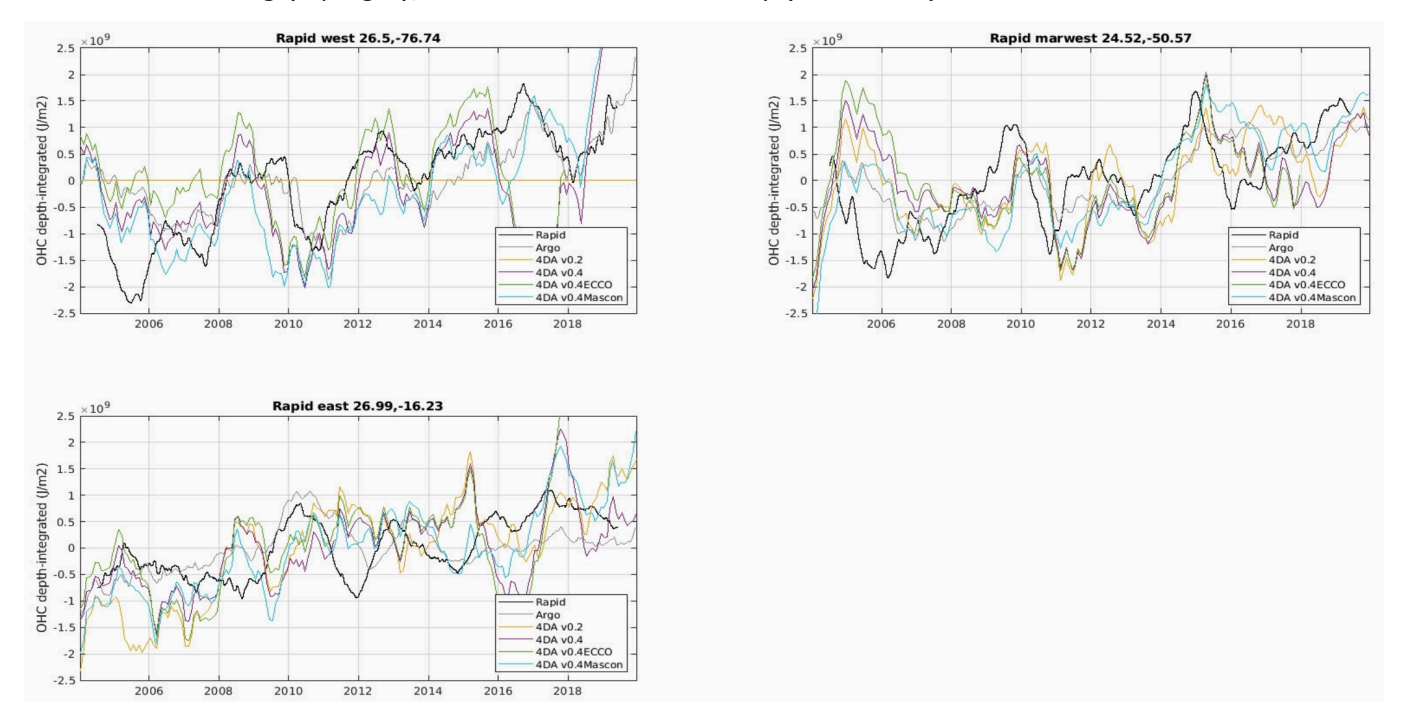


Figure 15: Temporal evolution of depth-integrated OHC anomaly at the mooring locations estimated from RAPID (black), NOC ARGO OI (grey), 4DAtlantic v0.2 (yellow) and 4DAtlantic v0.4 (purple), for the average of the Western boundary (top, left), the mooring west of the Mid-Atlantic Ridge (bottom, left) and the average of the Eastern boundary (bottom, right). Comparison with 4DAtlantic experimental products v0.4 ECCO (green) and 4DAtlantic Mascon (cyan).

2.3.2.3. Assessment across the RAPID-MOCHA transect

Following the approach described in 2.2.2.3.2 above, spatially integrated estimates of OHC anomaly were produced across the Western basin of the subtropical North Atlantic at 26.5 N spanning longitudes from 76.74° W to 50.57° W, and across the Eastern Basin comprised between longitudes 50.57° W and 16.23° W.



Date: 15/05/2025

Issue: 3.0

2.3.2.3.1. Western Basin

Figure 16 shows the temporal evolution of depth-integrated OHC anomaly estimated from the RAPID array at 26.5°N, spatially integrated across the Western basin of the North Atlantic (cyan). Equivalent 4DAtlantic OHC anomalies are shown in red for release v0.2 (top left), v0.4 (top right), v0.4-ECCO (bottom left) and v0.4-Mascon (bottom right). Trends are shown with dashed lines.

Verification of the 4DAtlantic OHC data against RAPID reveal good temporal agreement for all versions, albeit with different levels of agreement in terms of magnitude depending on the version.

Trend of OHC increase of 4DAtlantic v0.2 is found to be significantly higher (9.00 W/m2) than the one reported by RAPID (not shown here), whereas trend computed from 4DAtlantic v0.4 is much closer to it (5.82W/m2), a clear sign of improvement following the product development carried out in this study.

With respect to RAPID, analysis of the experimental versions shows that v0.4-ECCO is underestimating (4.07 W/m2) the OHC trend found in this area of the ocean, whereas v0.4-Mascon is overestimating it (6.63 W/m2).

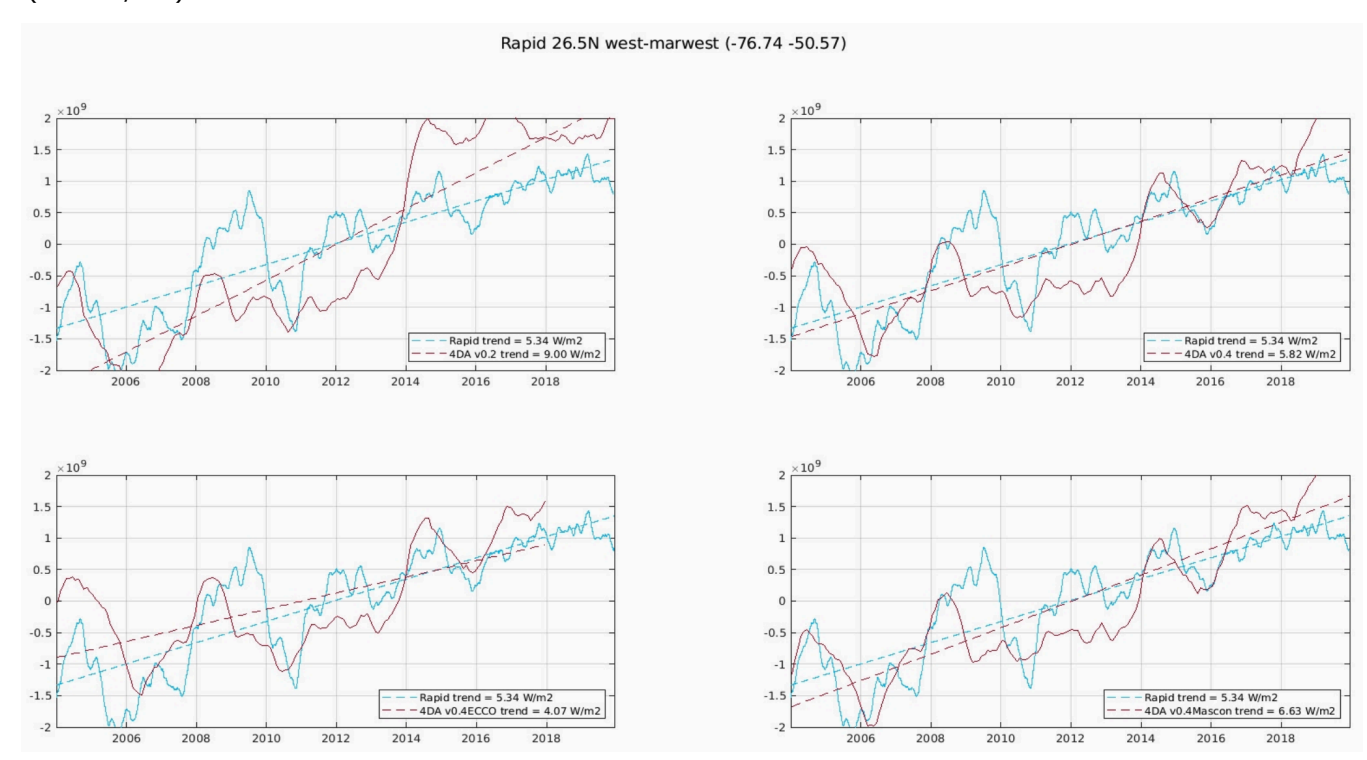


Figure 16: De-seasonalised temporal evolution of depth-integrated OHC anomaly estimated from the RAPID array at 26.5N spatially integrated across the Western basin of the North Atlantic (cyan). Comparison with estimates from 4DAtlantic OHC anomalies (red) computed using release v0.2 (top, left), v0.4(top, right), v0.4 ECCO (bottom, left) and v0.4 Mascon (bottom, right). Respective trends shown with dashed lines.

2.3.2.3.2. Eastern Basin

We proceed then with the analysis of the Eastern Basin along RAPID-MOCHA (26.5° N), between longitudes 50.57°W and 16.23°W.



Date: 15/05/2025

Issue: 3.0

Using a similar arrangement as the one described above, Figure 17 shows the temporal evolution of OHC anomaly integrated across the Eastern basin calculated using the four different 4DAtlantic versions, and assessed against RAPID.

In general we observe that temporal agreement with RAPID is not as good as in the Western basin, and that correlation does not depend much on product version. Again, the agreement with the array in terms of magnitude is seen to depend on the version used.

In comparison with the RAPID-estimated trend (3.75 W/m2), again we find that 4DAtlantic v0.2 is overestimating this (5.38 W/m2), and so is v0.4-Mascon (6.38 W/m2), whereas v0.4-ECCO is underestimating it (2.53 W/m2). Again we find that the closest space-based estimation is provided by 4DAtlantic v0.4 (3.99 W/m2), a tangible improvement over the previous product version.

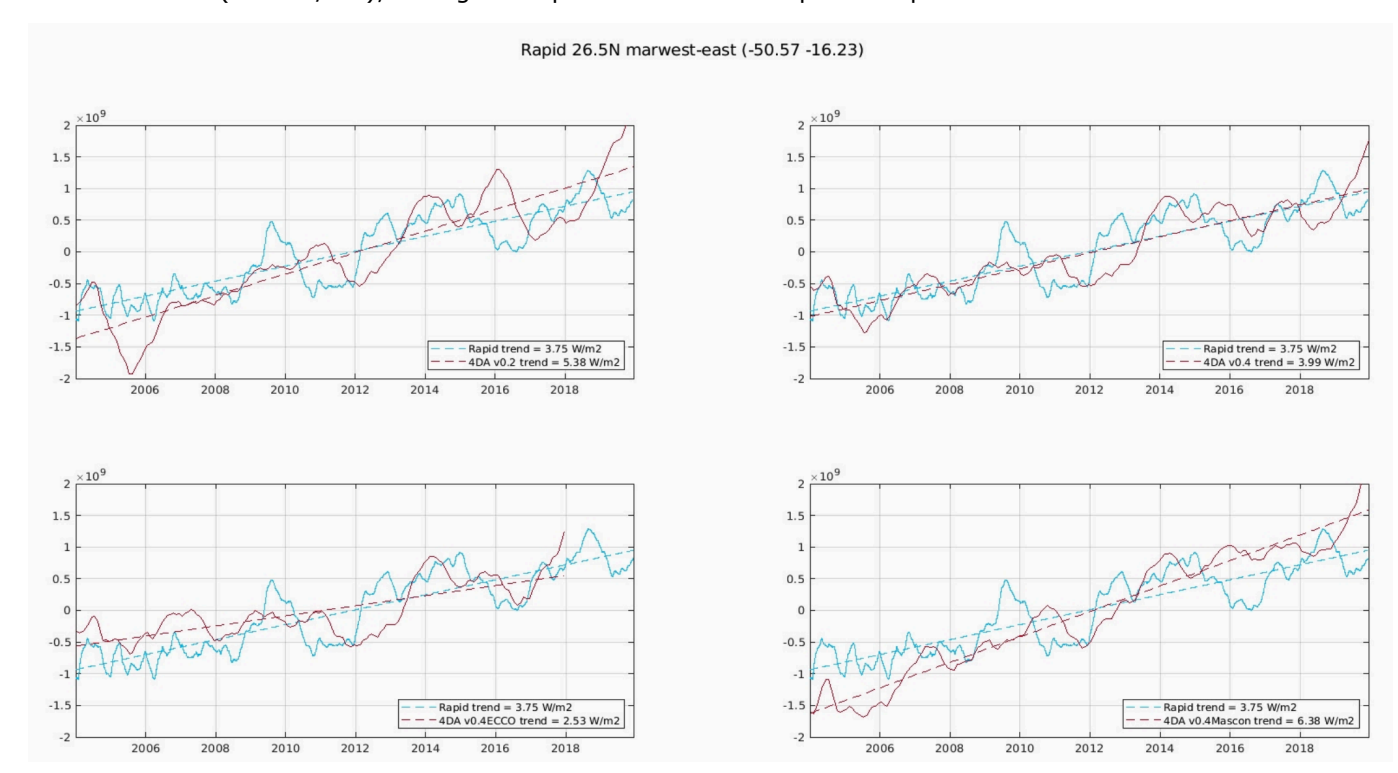


Figure 17 De-seasonalised temporal evolution of depth-integrated OHC anomaly estimated from the RAPID array at 26.5N spatially integrated across the Eastern basin of the North Atlantic (cyan). Comparison with estimates from 4DAtlantic OHC anomalies (red), computed using release v0.2 (top, left), v0.4(top, right), v0.4 ECCO (bottom, left) and v0.4 Mascon (bottom, right). Respective trends shown with dashed lines.

2.4. Summary

Two versions of the 4DAtlantic product (v0.2 and v0.4) were compared against in-situ OHC data in the Subtropical North Atlantic (20°N -40°N) computed from NOC ARGO OI. Comparison of the 4DAtlantic v0.2 product with NOC ARGO OI found that trend magnitude and seasonal cycle amplitude were typically higher in the 4DAtlantic v0.2 product than in NOC ARGO OI. This difference was greatly reduced in the 4DAtlantic v0.4 product although trend magnitudes and seasonal cycle amplitudes were still typically



Ref.: OHCATL DT 033 MAG

Date: 15/05/2025

Issue: 3.0

found to be higher in the 4DAtlantic v0.4 dataset. An apparent discontinuity in late 2013/early 2014 appears in all datasets and likely indicates a real geophysical signal, or a signal originating from temporal autocorrelation. Local variance-covariance matrices in the 4DAtlantic v0.4 product allowed calculation of trend uncertainties which were used to test if the NOC ARGO OI trends were significantly different from the 4DAtlantic v0.4 trends. The majority of the test region was found not to be significantly different, although some areas were found to be significantly different at the 2σ level, particularly in the Northwest and centre of the region of study.

Additional validation of both 4DAtlantic product versions v0.2 and v0.4 (including experimental versions v0.4 ECCO and v0.4 Mascon) was also carried out using verification OHC data computed from the RAPID-MOCHA mooring array measurements. Comparison at single mooring locations shows increasing OHC trends at all locations, for all satellite-based product versions, which is in agreement with both RAPID and NOC ARGO OI. Temporal correlation of the 4DAtlantic and RAPID OHC timeseries appears to be generally good, albeit a lag is sometimes observed. 4DAtlantic OHC anomaly magnitudes are generally on similar scales as RAPID, although some differences exist between different 4DAtlantic versions.

Verification along the OHC field estimated across the basin-wide RAPID latitude was split in two sections, the Western basin of the subtropical North Atlantic and the Eastern one. Results show better temporal correlation east of the Mid Atlantic Ridge than west of it. OHC increase trends are found to be higher in the Western section, than in the Eastern one. The agreement of 4DAtlantic with RAPID in terms of magnitude of the OHC increase trend is found to have some dependence on product version. Agreement between 4DAtlantic estimates and RAPID is found to have significantly improved in the course of this study, with relative discrepancies between OHC trends derived from 4DAtlantic v0.4 and from RAPID found to be within a $\sim 5-10\%$ range.

As recommendations for future validation activities, but also to facilitate the exploitation of the 4DAtlantic product, we suggest that the 4DAtlantic project provides estimates of the contribution to OHC anomalies from the waters below 2000 m, in addition to the full-depth estimates. This would allow for a more consistent validation as estimates of OHC based on NOC ARGO OI reflect only the contribution from the top 2000 m. This also applies to many potential users who typically rely on Argo data to obtain estimates of OHC. We would also recommend providing error covariance matrices for monthly time scales and, in the future, also spatial error covariances.



Date: 15/05/2025

Issue: 3.0

3. Validation on OVIDE section (V1.0)

3.1. Overview

The Subpolar North Atlantic (hereafter SPNA, Figure 18) plays a fundamental role in the large-scale redistribution of physical and biogeochemical properties (e.g. heat, freshwater, carbon ...) within the ocean interior, and is therefore a key actor of the Earth climate system. It undergoes pronounced OHC variability on a wide range of temporal scales and over significant depth ranges, notably due to the presence of vigorous vertical overturning and horizontal gyre circulation cells (Bryden et al., 2020; Piecuch et al., 2017), open ocean deep-water formation sites (Yashayaev and Loder, 2016) and strong surface-interior connectivity along its continental slopes (Desbruyères et al., 2020). The SPNA notably stands out of the global picture of upper OHC trends during 1993-2019 with a significant and unique cooling pattern (Johnson and Lyman, 2020). For those reasons, and because the SPNA is historically one of the most well-sampled basins of the world's oceans (temperature and salinity), it represents a best-choice for performing a data-driven validation of the 4DAtlantic satellite-based OHC product developed within the present project. This validation of the SPNA variability will be performed using independent in situ observational arrays with complementary sampling capabilities - i.e. capturing different temporal and spatial scales of variability - and all enabling robust full-depth OHC monitoring.



Date: 15/05/2025 Issue: 3.0

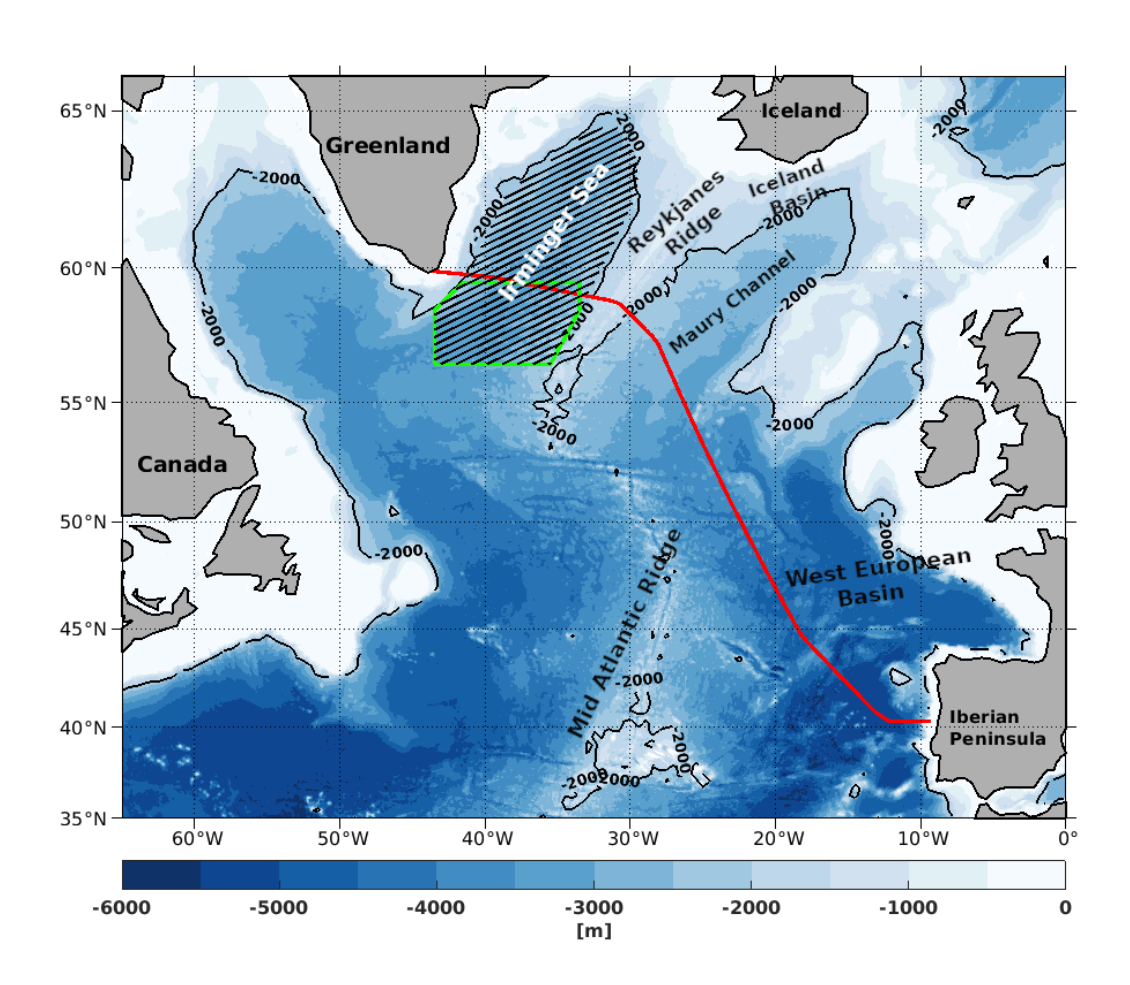


Figure 18: The north Atlantic ocean area. Bathymetry is based on the ETOPO dataset (doi:10.7289/V5C8276M) with the solid black line showing the -2000m isobath. The red line shows the A25-OVIDE hydrography sections. The black hatched area represents the Irminger sea for the validation of the Ocean Heat Content (OHC) estimates from the space geodetic 4DAtlantic product. The green contour corresponds to the commun area between the 4DAtlantic product and the in situ-based product for validation purposes.

3.2. Data and Methods

To evaluate the regional reliability of the space geodetic 4DAtlantic-v0.4 estimates in the SPNA, two in situ datasets are used: A25-OVIDE and ISAS21. A25-OVIDE hydrographic data (Mercier et al., 2015) consist of 9 biennial CTD sections (~98 stations) of temperature (T) and salinity (S) profiles (Portugal-Greenland, red line on Figure 18). The CTD casts have a high vertical resolution of 1 meter (from surface to the near sea-floor), with an accuracy of 0.002 °C for temperature and 0.002 PSS-78 for salinity. The oceanographic cruises took place every other year during 2002-2018 (in early boreal summer: May-June or June-July). Vertical profiles of T and S, typically spaced out by 20 meters in the



Date: 15/05/2025

Issue: 3.0

interior down to a few meters above steep continental slopes, have been objectively interpolated onto a \sim 7km horizontal grid.

The validation activities will also consider the In Situ Analysis System (ISAS) which is a 3D gridded monthly-mean product of S and T from Argo measurements (https://doi.org/10.17882/52367). ISAS is based on an optimal interpolation method (Gaillard et al., 2016) with 187 standard depth levels between 0-5500 m depth and $0.5^{\circ}x0.5^{\circ}$ global horizontal grid. In the SPNA, the horizontal grid resolution along the latitude is in the range of $\sim 0.20^{\circ}$ to $\sim 0.4^{\circ}$ while longitudinal resolution is 0.5° . ISAS21 is an update of ISAS20 (Kolodziejczyk et al., 2021) that is built with all available Deep-Argo profiles (Roemmich et al., 2019) over the 2002-2020 period including all Deep-Argo profiles available in the Irminger sea (Desbruyères et al., 2022).

The full-depth steric sea level (SSL, in m), Halosteric sea level (HSSL, in m) and Ocean Heat Content per unit area (OHC, in J/m²) from in situ measurements are estimated as follow:

$$\Delta(SSL) = -1/\rho_0 \cdot \int_{Z}^{0} (\rho - \rho_0) \cdot dz \qquad \text{(eq. 9)}$$

$$\Delta(HSSL) = -1/\rho_0 \cdot \int_{Z}^{0} [\rho(S, \overline{T_{2002-2018}}, p) - \rho_0] dz$$
 (eq. 10)

$$OHC = Cp. \, \boldsymbol{\rho}_0 \int_Z^0 T(z). \, dz \qquad \text{(eq. 11)}$$

where $\rho_0 = \rho(S=35.165, T=0, p)$ is the reference density (using TEOS-10). S, T and p are Absolute salinity (in g/kg) , conservative temperature (in °C) and Pressure (dbar), respectively. Cp=3991.87 J/kg. K° represents the heat capacity used in TEOS-10. $\overline{T}_{2002-2018}$ represents the average conservative temperature over the period 2002-2018 from the A25-OVIDE hydrographic data. Note that prior to the intercomparison process, all in situ estimates have been regridded onto the spatial grid resolution of the space geodetic 4DAtlantic product (1°x1°). Each time series presented in this validation part is an anomaly with respect to its time mean.

The local geodetic OHC error estimates along the A25-OVIDE section and within the selected domain for the Irminger sea are respectively evaluated following equations 12 and 13 for the lower bounds and the upper bounds of the real uncertainty, assuming that those errors are not correlated spatially:

$$\varepsilon_{OHC_{lower bounds}} = \sqrt{\frac{\sum\limits_{i=1}^{N} S_{i}^{2} Var_{i}}{(\sum\limits_{i=1}^{N} S_{i})^{2}}}$$
 (eq. 12)



Date: 15/05/2025

Issue: 3.0

$$\varepsilon_{OHC_{upper bounds}} = \frac{1}{\sum\limits_{i=1}^{N} S_i} \sum\limits_{i=1}^{N} S_i \sqrt{Var_i}$$
 (eq. 13)

where S_i represents the area of grid i and Var_i the local temporal variance of the OHC estimates for the grid i. Then we plot $1.96*\epsilon_{OHC_{lower\,bounds}}$ as error bars on the annual OHC time series and $\epsilon_{OHC_{upper\,bounds}}$ in order to consider the 95% confidence intervals of OHC estimates. The $\epsilon_{OHC_{upper\,bounds}}$ are set using (Levitus et al., 2012) approach and represent the arithmetic average of the local errors. The same approach is used to estimate ϵ_{sst} for the steric sea level (SSL) estimates from the 4DAtlantic product.

3.3. Interannual variability along the A25-OVIDE sections

3.3.1. Comparisons between the 4DAtlantic and A25-OVIDE products over 2002-2018

The 9 biennial A25-OVIDE hydrographic data, with high horizontal and vertical resolution, enables accurate estimates of the full-depth OHC across the eastern SPNA (see the red line in Figure 18). The times series of the intercomparison of the full-depth OHC anomalies estimates from the space geodetic 4DAtlantic v0.4 product and the in situ A25-OVIDE data are shown in the Figure 19a. Over the full period (2002-2018), the OHC 4DAtlantic estimates (blue curve) show larger amplitude variations from 1.0 x 10° J/m² to -1.5 x 10° J/m² with a standard deviation, STD = $\sim 10^{\circ}$ J/m². The in situ OHC estimate is shown with the black line with variations ranging from -1.25 to $1.5*10^{\circ}$ J/m² and an STD = $\sim 7*10^{8}$ J/m². Over the entire period, the 4DAtlantic OHC and the A25-Ovide OHC exhibit cooling trends of ~ -10.54 w/m² and ~ -2 w/m², respectively. They have a correlation of r = 0.6 statistically-significant at the 95% confidence level.

In particular, during 2010-2018, there is a strong correlation (with r=0.9 at 95% confidence level) between the two OHC time series: heating and cooling episodes are consistently observed from both OHC estimates. However, there is less consistency between OHC times series prior to that period - 2002 to 2010 - (with r=0.4 as correlation coefficient). One can notice that during 2002-2010, the 4DAtlantic OHC time series shows a cooling trend of \sim -7.43 w/m² whereas the in situ OHC time series trend is negligible (of \sim -0.33 w/m²).



Date: 15/05/2025

Issue: 3.0

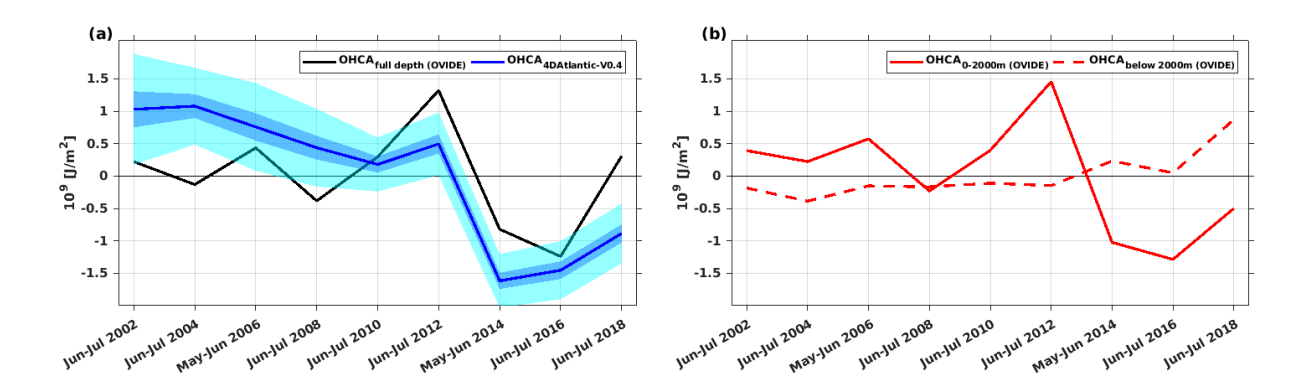


Figure 19: Intercomparison of time series of the full depth Ocean Heat Content Anomalies (OHC) estimates averaged along the A25-OVIDE line from (a) geodetic 4DAtlantic-OHC v0.4 product and in situ OVIDE hydrographic data set (black curve). The light blue and cyan bands represent respectively the lower and upper bounds of the error associated with the OHC estimates from the 4DAtlantic product. (b) A25-OVIDE 0-2000m layer's OHC (solid red cure) and 2000m-bottom (dashed red curve). The OHC are referred to the OHC mean over A25-OVIDE sections period (2002-2020).

If the upper 2000m depth of the oceans has been well constrained by Argo floats since the mid-2000s, temperature and salinity changes in deeper layers are still mostly unknown. Based on the A25-OVIDE data, the full-depth OHC estimate can be decomposed into two layers to evaluate their respective contributions to the full-depth OHC anomalies: 0-2000m depth (red solid line) and 2000m-bottom (dashed red line; see Figure 19b). The 0-2000m OHC time series shows relatively large interannual variations similar to the full-depth OHC estimate, with peak-to-peak amplitude of $\sim 2.8*10^{\circ}$ J/m² and a STD of $\sim 8*10^{\circ}$ J/m². The deeper layer (2000m-bottom) of OHC exhibits weaker changes (peak-to-peak amplitude of $\sim 1.26*10^{\circ}$ J/m² and STD = $\sim 3.5*10^{\circ}$ J/m²). However, while the OHC (0-2000m) therefore explains most of the full-depth OHC variability along the OVIDE line, the deep OHC (below 2000m) is not always negligible. Between 2016 and 2018 in particular, the deep OHC accounted for about 63 % of the full-depth warming rate.

To evaluate the local and basin-scale estimates of the geodetic product, the scatterplot of the full-depth OHC from the 4DAtlantic product and in situ estimates at each grid point along the section is presented in Figure 20a. One can notice the overall good correlation of r = 0.5 (at 95% confidence level) with a RMSD (Root-Mean-Square Deviation) of $0.23*10^{10}$ J/m² between both OHC estimates. The linear regression fit (equation 14) between both estimates indicates that OHC estimates from the 4DAtlantic product is locally lower by factor of $\sim 2/5$ than the in situ estimates.

$$OHCA_{4DAtlantic} = 0.42 * OHCA_{A25-OVIDE} + 1.39 * 10^{-6}$$
 (eq.14)

The largest differences between local OHC estimates along the OVIDE line are found east of Reykjanes Ridge in the range of 1200-3500 km from Greenland (most green to red dots in the Figure 20a). The analysis of the systematic differences - $\Delta(OHC)$ - reveals indeed a large spread of $\pm 8*10^{\circ} \text{J/m}^2$ in the Iceland and Iberian Basins (West European Basin) while smaller spread of $\pm 4*10^{\circ} \text{J/m}^2$ is observed in the Irminger sea ($\sim 0-750$ km from Greenland, West of the Reykjanes Ridge, Figure 20b). This is likely linked to the more energetic upper-layer dynamics found in the eastern basins (North Atlantic Current), and the large filtering of its temperature signature in the coarse-resolution geodetic estimate (300km, monthly-mean) compared to the in situ estimate (10 km, snapshot).



Date: 15/05/2025

Issue: 3.0

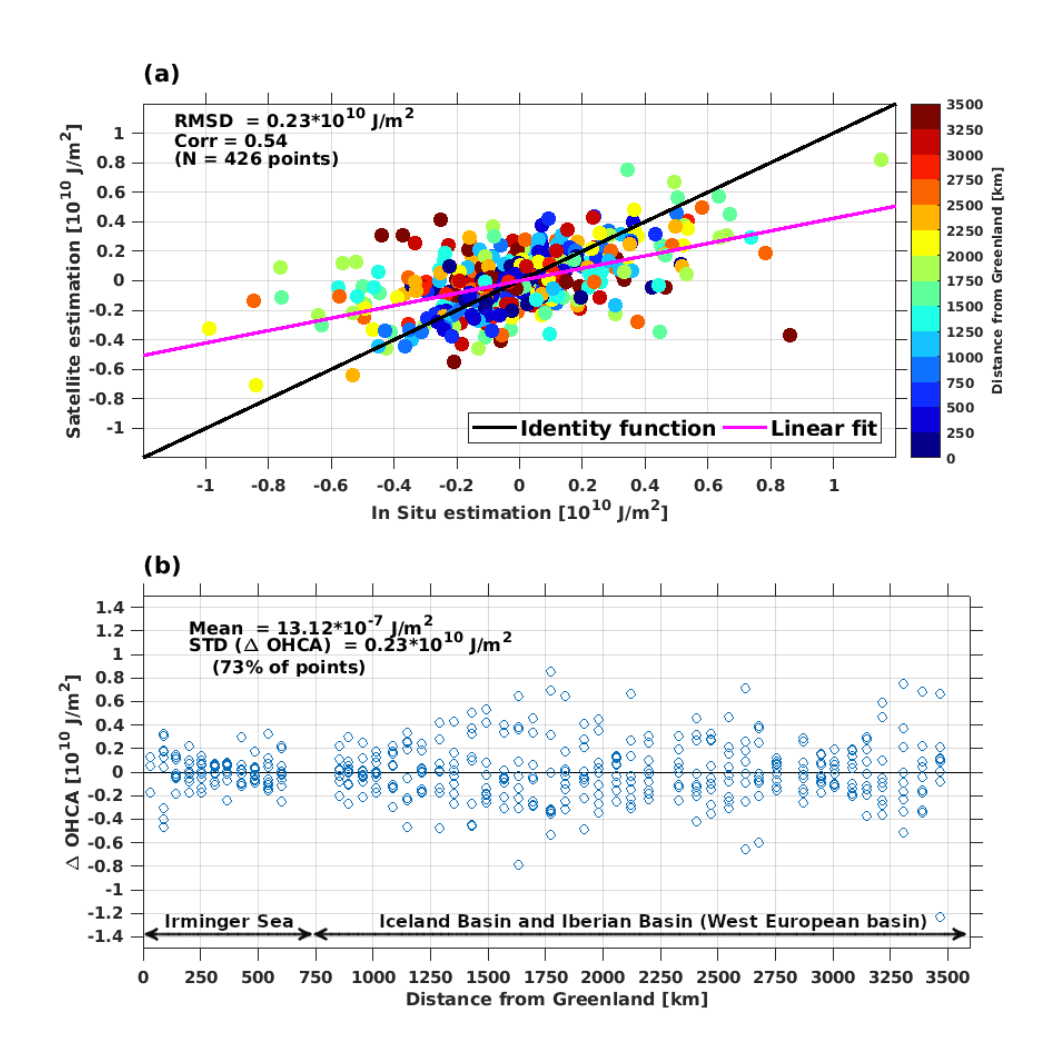


Figure 20: a) Scatter-plot of Ocean Heat Content estimates from 4DAtlantic OHC v0.4 product (vertical axis) and from in situ A25-OVIDE sections hydrographic data set (horizontal axis). The color of the dots indicates the distance from the Greenland; b) Systematic difference between OHC estimates from 4DAtlanti product and from in situ A25-OVIDE data set.

3.3.2. Sub-Basin intercomparison of the OHC estimates

In this section, the ability of the 4DAtlantic solution to capture OHC changes at regional scale is presented and analyzed (Figure 21). In the Irminger sea, all time series of OHC (4DAtlantic -blue curve-, A25-OVIDE full-depth -black curve- and A25-OVIDE 0-2000m - red curve) are well correlated (r = 0.96 at 95% confidence level, Figure 21a). Indeed, the linear regression trends from all time series exhibit a cooling OHC trend of ~-12.32±8.88 w/m² and ~-8.76±6.89 w/m² respectively from 4DAtlantic product and In situ estimates over the entire period of 2002-2018. The observed consistency between OHC time series suggests that the geodetic OHC product is accurate enough to capture the OHC interannual



Date: 15/05/2025

Issue: 3.0

changes and linear trends in a region characterized by relatively quiescent dynamics like the Irminger basin. In contrast, less consistency between OHC time series (r=0.52) is observed for the basins east of Reykjanes Ridge (Figure 21b). During 2002-2010, OHC (4DAtlantic) time series exhibit a strait cooling episode (of \sim -10.63 \pm 3.62 w/m²) through a weakening of \sim -1.5 \pm 10° J/m² whereas in situ estimates show a nearly stable variations of \pm 5 \pm 108 J/m² (of \sim -2.48 \pm 9w/m²) around the OHC mean state. However, beyond 2010, OHC time series are consistent with each other. Thus, regional dynamical characteristics may be determinant in the accuracy of the 4DAtlantic product to capture the OHC changes at the considered time scale (biennial timescale).

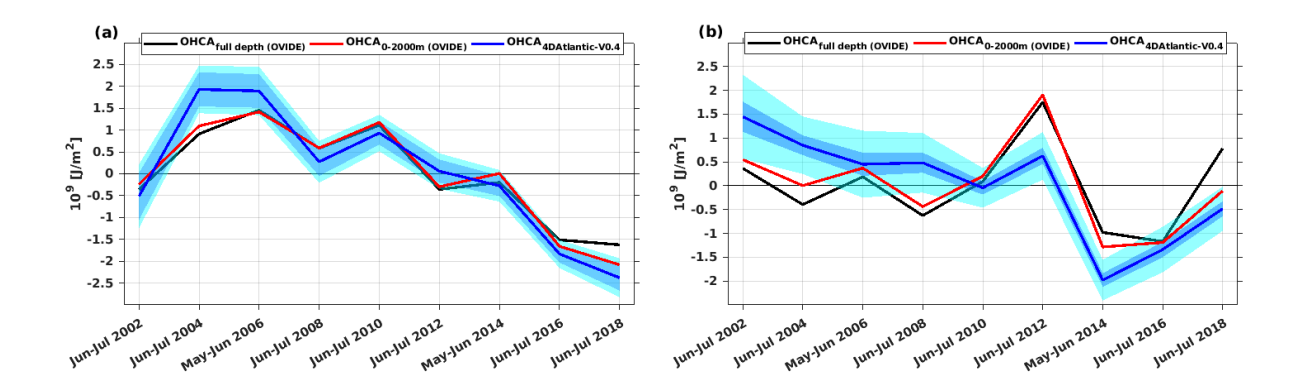


Figure 21: Decomposition of the OHC time series of the A25-OVIDE line into two sub-basins in the Subpolar North Atlantic: (a) for the Irminger sea (West of the Reykjanes Ridge until greenland) and (b) for the Iceland and the Iberian basins (West European basin between Reykjanes Ridge and Portugal). Time series show the space geodetic 4DAtlantic OHC estimates (blue curve), the in situ A25-OVIDE OHC estimates for the full-depth (black curve) and 0-2000m layer (red curve). The light blue and cyan bands represent respectively the lower and upper bounds of the error associated with the OHC estimates from the 4DAtlantic product. The OHC are referred to the OHC mean over A25-OVIDE sections period (2002-2020).

3.4. Seasonal and interannual time scales

3.4.1. Seasonal full-depth OHC changes in the Irminger sea

The intercomparison of the seasonal cycle of the full-depth OHC from the space geodetic 4DAtlantic product and the in situ estimates in the Irminger sea is shown in the Figure 22. There is a fair match between both estimates during boreal winter (Jan-Feb-Mar) whereas discrepancies of about $5*10^8$ J/m² are observed beyond this season (r=0.8 at 95% confidence level). 4DAtlantic-OHC estimates show a minimum peak of \sim - $6*10^8$ J/m² by March, one month earlier than the minimum peak of \sim - $1.12*10^9$ J/m² (in April) from ISAS21 OHC estimates. However, the seasonal maximum peak of OHC in the Iminger sea is observed in September from both OHC estimates: \sim 9.56*10° J/m² and \sim 6*10° J/m² from 4DAtlantic and ISAS21 OHC estimates respectively. The magnitude of the seasonal variations of OHC in that region is about $1.24*10^9$ J/m² from the geodetic 4DAtlantic product while it is \sim 2.08*10° J/m² from in situ ISAS21 estimates. Note that the geodetic full-depth OHC estimates over the seasonal cycle are overall (except during winter) smaller by a factor \sim 2 compared to the in situ full-depth OHC estimates.



Date: 15/05/2025

Issue: 3.0

In the considered Irminger basin (of maximum depth of ~ 3500 m), the OHC changes mainly occur within the layer from the surface to 2000m depth, while OHC changes below 2000m depth can be neglected. Therefore, the observed discrepancies between the space geodetic OHC product and the In situ OHC estimates at seasonal timescale may likely not be associated with a full-depth representativeness concern, at least within the region considered here (likely from the full-depth halosteric sea level computation).

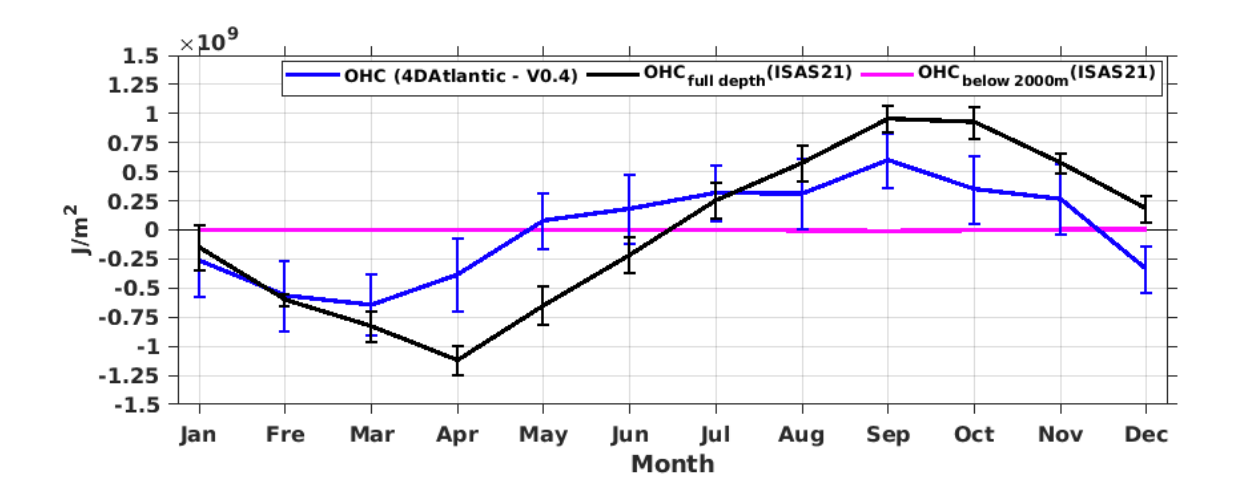


Figure 22: 2002-2020 climatology of seasonal time series of the full-depth OHC estimates from the geodetic 4DAtlantic product (blue curve) and ISAS21 product (black curve) in the Irminger Sea. The vertical blue and black bars represent the spatial STD for the selected domain for Irminger sea. The magenta curve represents the estimates of OHC seasonal cycle for the layer of 2000m-bottom from ISAS21 product.

3.4.2. Year-to-year full-depth OHC changes in the Irminger sea

In this section, we evaluate the OHC estimates from the 4DAtlantic OHC product against ISAS21 OHC estimates in the Irminger sea. The inter-comparison of time series of month-to-month OHC changes during 2002-2020 in the Irminger sea is shown in Figure 23. One can notice that there is a good correlation of r=0.8 (at 95% confidence level) between OHC sub-annual change estimates from both products. The year-to-year seasonal cycle of OHC change is overall well reproduced by the 4DAtlantic product. However, during 2004 a significant mismatch is observed (with r=0.17). In addition, during 2016 anti-correlation of -0.07 are observed between the two OHC time series. Despite these scarce mismatches, consistent OHC trends of -5.28 \pm 0.73 w/m² and -4.42 \pm 0.78w/m² are respectively found for the 4DAtlantic OHC product and in situ ISAS21 estimates.

Consistent cooling trends patterns are also observed spatially in both products in the SPNA, notably in the Irminger, Iceland, Iberian and West European basins (Figure 24). It is worth noting, however, that the full-depth OHC 4DAtlantic product seems to overestimate the cooling trend in the Labrador sea (and also east of Reykjanes Ridge).



Date: 15/05/2025

Issue: 3.0

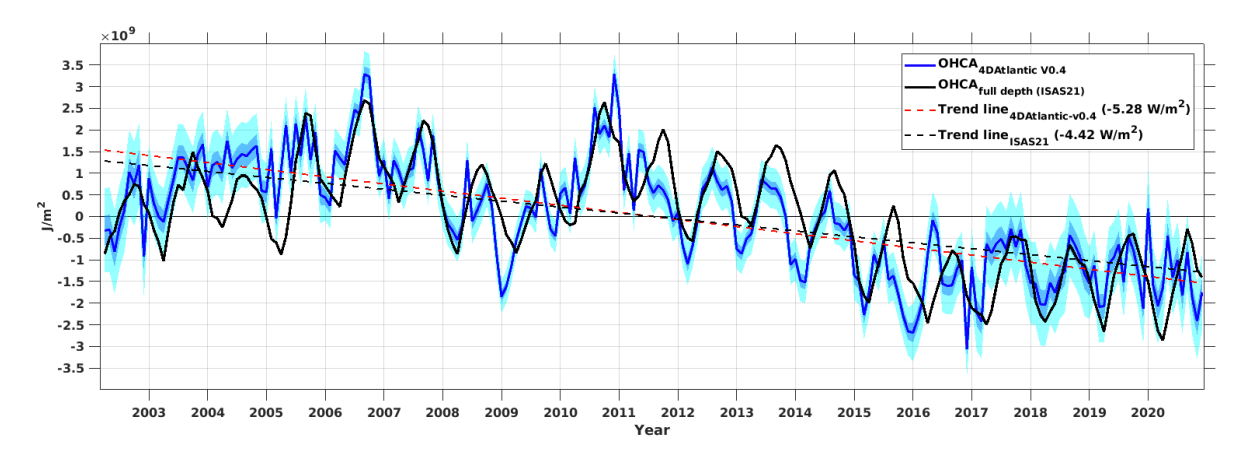


Figure 23: Interannual time series of the Ocean Heat Content Anomalies (OHC) referred the 2002-2020 OHC mean in the Irminger (area of green contour of the Figure 1) estimated from the space geodetic 4DAtlantic OHC product (solid blue curve) and the in situ ISAS21 data set (solid black curve). The dashed red and black curves are OHC trend lines from 4DAtlantic and ISAS21 estimates respectively. The light blue and cyan bands represent the lower and upper bounds of error associated with the OHC estimates from the 4DAtlantic product.

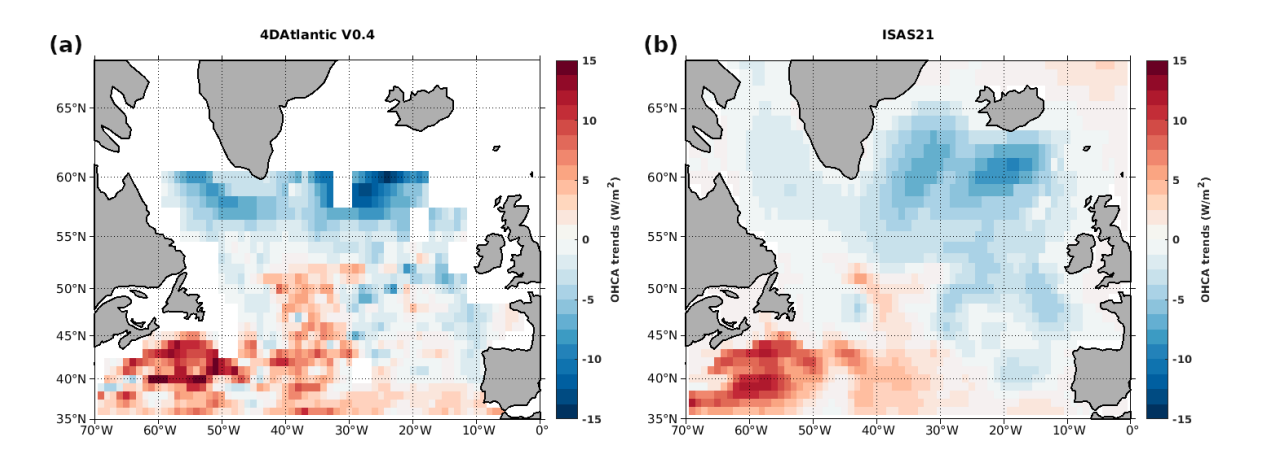


Figure 24: Trends of Ocean Heat Content Anomalies (OHC) from (a) 4DAtlantic product and (b) ISAS21 in situ product in the SPNA.

Regarding the inter-annual time scales of the full-depth OHC changes in the Irminger sea (Figure 25), all time series show a good agreement (r = 0.92 at 95% confidence level) over the entire period. However, during 2003-2005 and in 2013, discrepancies are noticed of about $\pm 7.5*10^8$ in both estimates.

The OHC inter-annual changes within the layer from the surface to 2000m depth explains a large fraction of the full-depth OHC changes (Figure 25). The OHC changes within the layer below 2000m depth are fairly small compared to the full-depth OHC, with an order of magnitude of 108 J/m². The maximum OHC



Date: 15/05/2025

Issue: 3.0

fluctuation (below 2000m depth) occurred over 2016-2020, with a maximum peak of \sim 6.7*10 7 J/m² (which represents 10% of the full-depth OHC changes during that period).

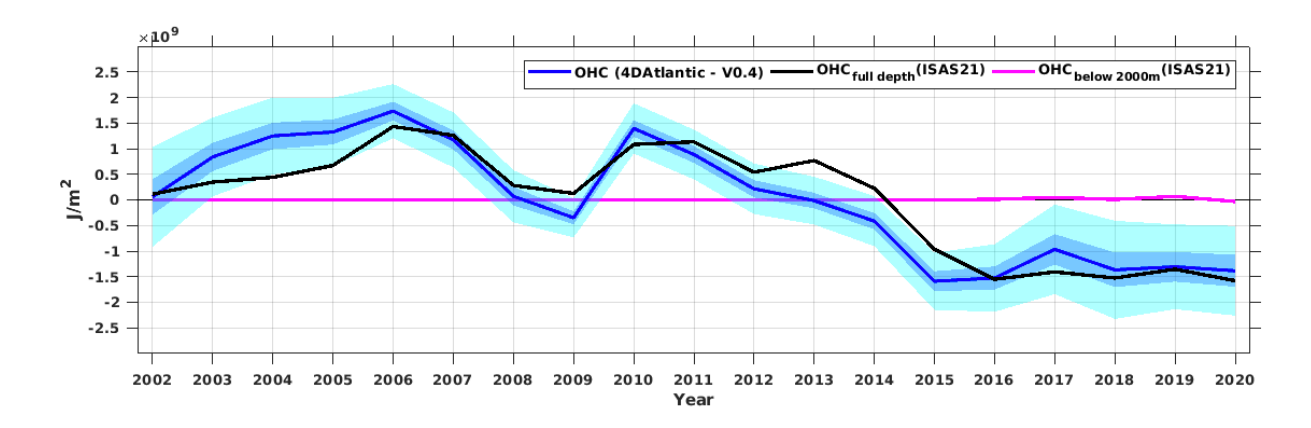


Figure 25: Interannual time series of OHC changes estimates over 2002-2020 in the Irminger sea from the geodetic 4DAtlantic product (blue curve) and from ISAS21 in situ product (black curve). Time series of OHC changes within the layer from 2000m depth to bottom (magenta curve) from ISAS21 in situ product. The light blue and cyan bands represent the lower and upper bounds of error associated with the OHC estimates from the 4DAtlantic product.

3.5. Assessing the geodetic local uncertainties

This section aims to evaluate (i) the magnitude of uncertainties in the satellite-derived OHC estimates related to its coarse resolution, (ii) the reliability of the geodetic full-depth steric sea level anomalies (SSLA) estimates against A25-OVIDE estimates and (iii) the deep (below 2000m) halosteric sea level anomalies (HSSLA) contribution to the SSLA.

To evaluate the potential magnitude of uncertainties in the satellite-derived OHC (4DAtlantic) estimates, our approach is based on analyzing the effects of subsampling the full-resolution (\sim 7km) of in situ A25-OVIDE hydrographic fields onto the 4DAtlantic spatial grid resolution (1° x1°). Time series of full-resolution (black curve) and regridded (red curve) OHC estimates from A25-OVIDE exhibit respectively a standard deviation of \sim 7.11*10⁸ J/m² and \sim 8.23*10⁸ J/m² (Figure 26a). We find differences of \sim 10⁸ J/m² between the high and low spatial resolution estimates. The time series of the difference between in situ OHC estimates based on this approach is shown in Figure 26b (red bars). The main differences of Δ 0HC (more than \sim 25*10⁸J/m²) are observed over the period of mismatch between the space geodetic 4DAtlantic OHC and the in situ estimates (blue curve in Figure 26a). The observed subgrid biases represent about 10% of the order of magnitude of OHC estimates. OHC subgrid biases appear then significant.



Date: 15/05/2025 Issue: 3.0

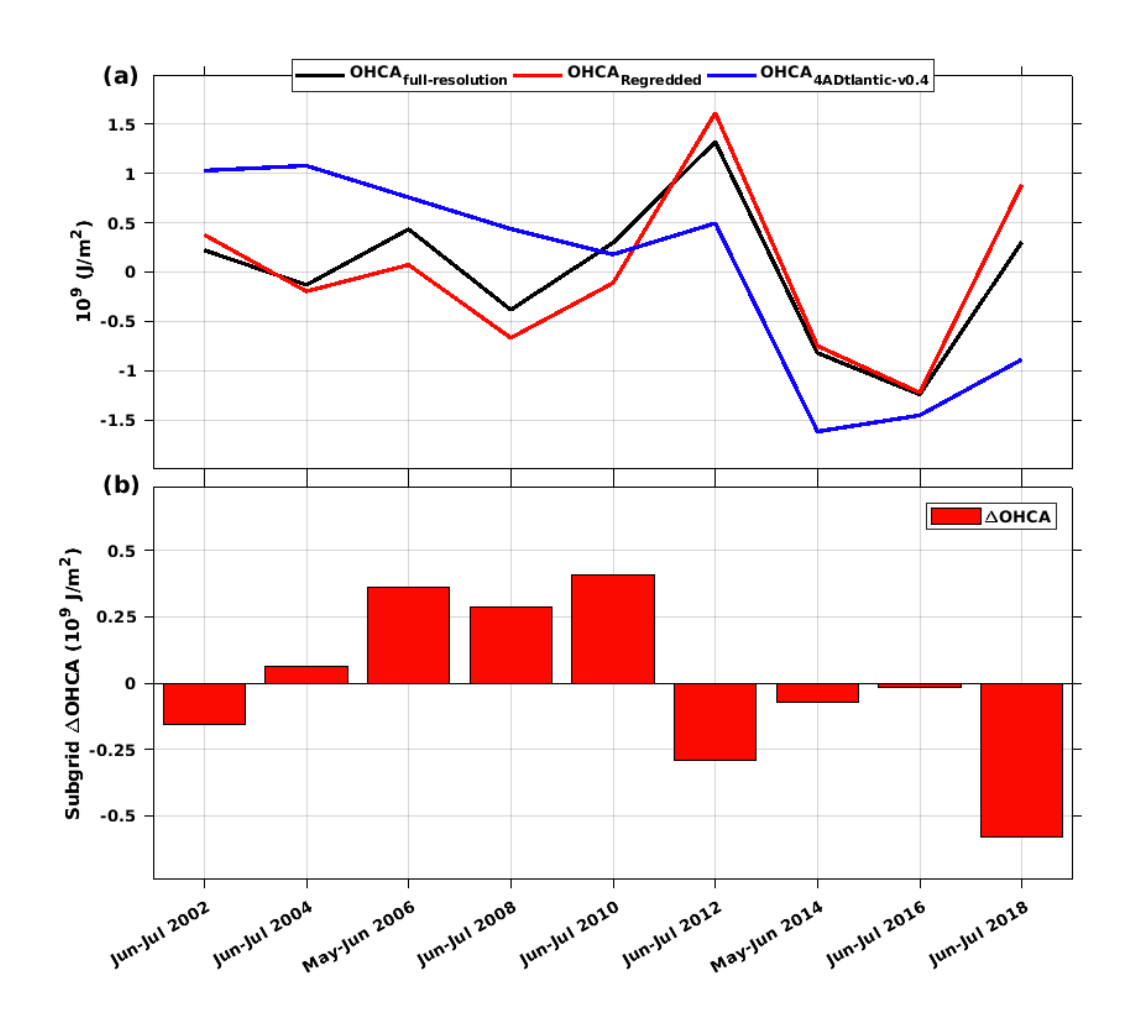


Figure 26: (a) OHC estimates from in situ OVIDE hydrographic with the full-resolution (black curve), with the geodetic 4DAtlantic-OHC v0.4 grid resolution (1°x1°, red curve) and from 4DAtlantic-OHC product (blue curve) averaged along A25-OVIDE line. (b) Difference of OHC A25-OVIDE estimates between the full in situ resolution and satellite-derived grid resolution: $\Delta OHC = OHCA(OVIDE)_{full \, resolution} - OHCA(OVIDE)_{satellite \, resolution} (red \, barplot).$

The intercomparison of space geodetic 4DAtlantic steric sea level anomalies (SSLA) against in situ OVIDE full-depth SSLA estimates is presented in the Figure 27a. One can notice that both SSLA time series agree over 2008-2014 (r=0.8 as correlation coefficient at 95% confidence level). However, during 2002-2006 the SSLA 4DAtlantic estimates display larger amplitude variation (of ~4cm, with STD = 1.6cm) than in situ estimates (of ~1cm, with STD = 0.41 cm). In particular, beyond 2014, both SSL estimates depict discrepancies. Since the total sea level anomalies are the sum of Ocean mass anomalies and the steric sea level anomalies (see equation 15), this suggests a large ocean mass component in the 4DAtlantic SSL reconstruction whereas the in situ SSL estimate is pointing out its relatively low contribution. There may be an inconsistency in the ocean mass estimates in the 4DAtlantic-OHC. Thus, the observed discrepancies in the OHC 4DAtlantic estimates against the in situ one (see Figure 19) may also be due to the SSL computation process, likely in the full-depth halosteric (HSSL) and thermosteric



Date: 15/05/2025

Issue: 3.0

(TSSL) components estimates. In fact, the OHC is derived from the full-depth TSSL with the integrated efficiency coefficient of heat (IEEH) so that errors from SSL estimates will be propagated into OHC estimates. This may also be due to the spatio-temporal inconsistency between the spatial geodetic sampling and the in situ dataset: the spatial geodetic product data are monthly with a spatial resolution of $1^{\circ}x1^{\circ}$ whereas the OVIDE in situ data situ are mostly a snapshot (\sim days timescale) with 7 kmx 7 km spatial resolution.

$$\Delta SL_{total} = \Delta SL_{mass} + \Delta SL_{steric} \quad \text{(eq.15)}$$
 where $\Delta SL_{steric} = \Delta SL_{halosteric} + \Delta SL_{thermosteric} \quad \text{(eq.16)}$

Regarding the halosteric sea level anomalies (HSSLA) time series from A25-OVIDE hydrographic data, it is found that the largest variation (STD = 2.4cm) of the full-depth HSSLA appear within the surface to 2000m over the entire OVIDE sections period (Figure 27b), with a positive trend of $\sim 0.61 \text{cm/yr}$. The 2000m-bottom HSSLA shows weaker interannual variations but still accounts for a positive trend of $\sim 0.23 \text{cm/yr}$, which largely results from a sharp deep ocean freshening during 2012-2018. This suggests that neglecting the deep halosteric sea level changes might not be a valid hypothesis in the subpolar North Atlantic ocean, especially over the OVIDE section.



Date: 15/05/2025 Issue: 3.0

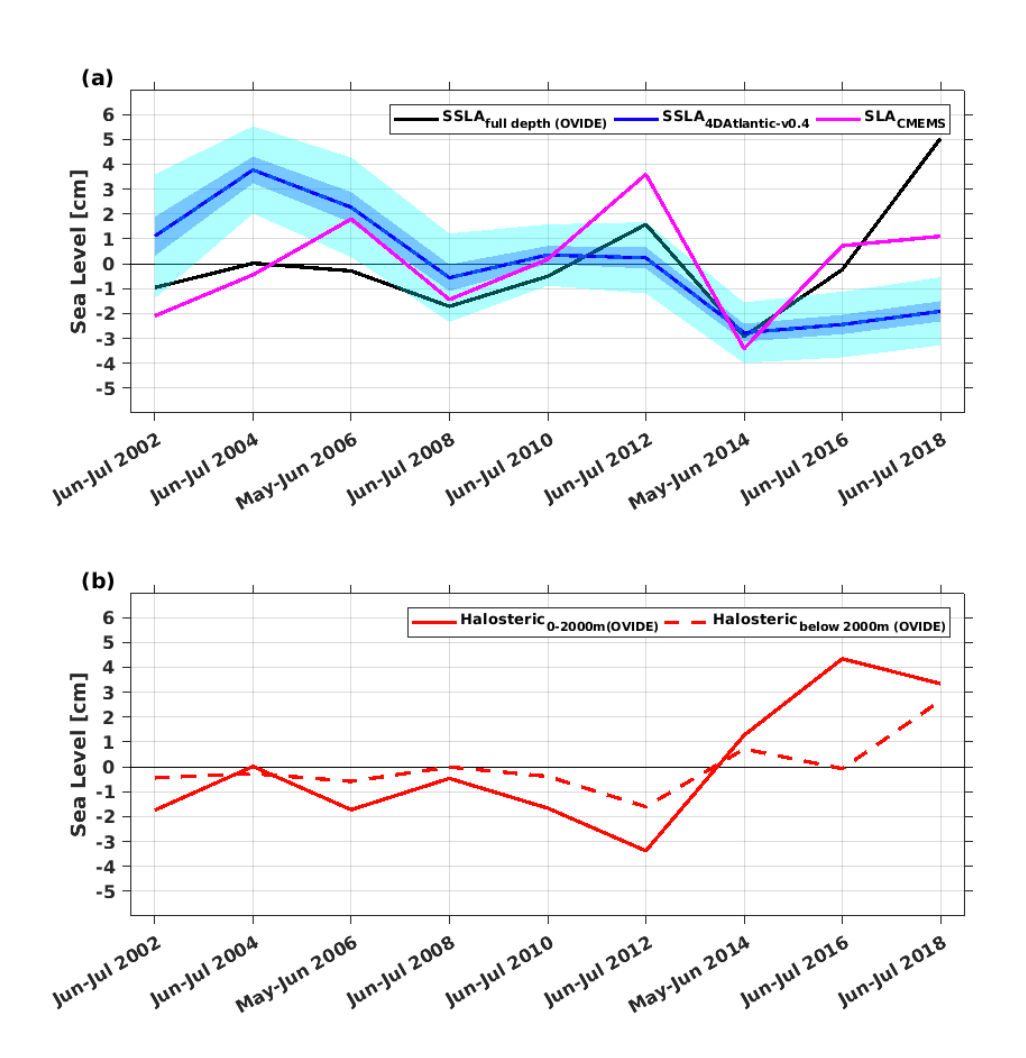


Figure 27: (a) Full-depth Steric sea level anomalies (SSLA) estimates from A25-OVIDE hydrographic data (black curve) and the space geodetic 4DAtlantic product (blue curve) and, the associated Sea Level Anomalies (LSA) from CMEMS product (magenta curve) during 2002-2018. The light blue and cyan bands represent respectively the lower and upper bounds of the error associated with the SSL estimates from the 4DAtlantic product. (b) sub-layer decomposition of the halosteric sea level anomalies (HSSLA): 0-2000m depth layer (solid red curve) and for the layer below 2000m (dashed red curve).

3.6. Validation of experimental products

3.6.1. Overview

This complement of the validation tasks stands to evaluate the reliability of the 4DAtlantic-OHC product from different methods in the Subpolar North Atlantic (SPNA, Figure 28). Two types of 4DAtlantic-OHC products are evaluated: first product includes the ECCO model for the computation of the



Date: 15/05/2025

Issue: 3.0

IEEH (over 2002-2017), which offerts northward spatial coverage (>60°N), and second product includes the MASCON method (over 2002-2020).

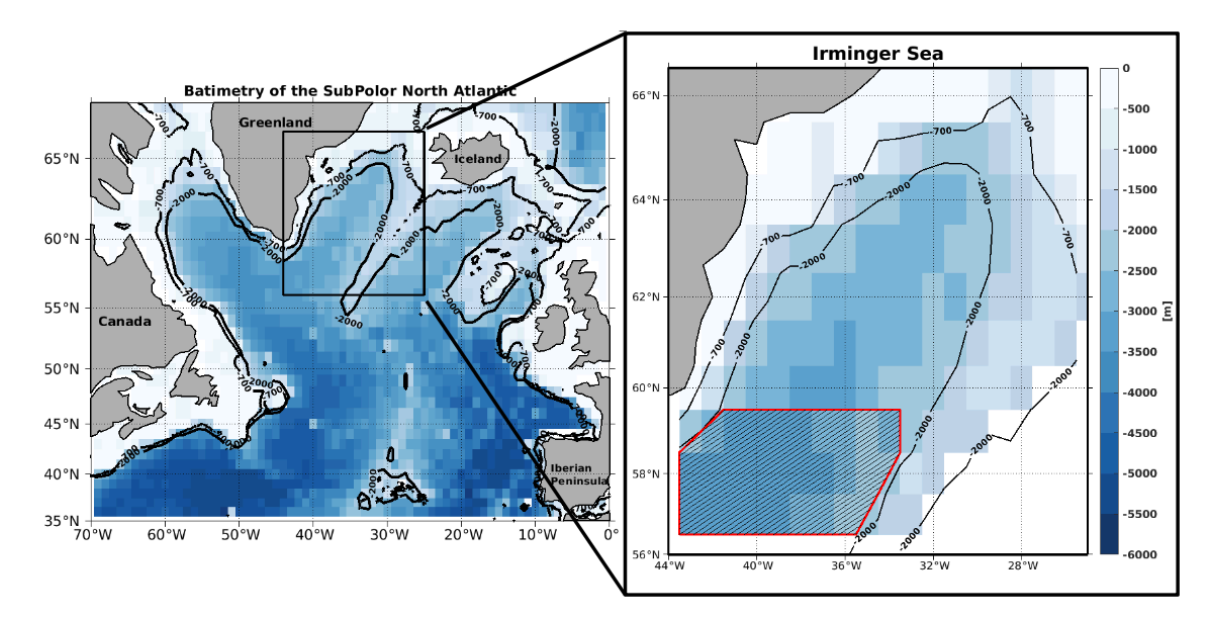


Figure 28: The north Atlantic ocean area (left panel). Bathymetry is based on the ETOPO dataset (doi:10.7289/V5C8276M) with the solid black line showing the -2000m isobath. Right: Commun area of the Irminger sea between 4DAtlantic-OHC (with ECCO model) and ISAS21 products, and the red contour (hatched area) corresponds to the common area between the 4DAtlantic product (with MASCON method) and the ISAS21 product for validation purposes.

3.6.2. 4DAtlantic with ECCO model vs ISAS21 estimates

In this section, the comparison between 4DAtlantic-OHC (with ECCO model) and ISAS21 OHC estimates is presented and analyzed, from seasonal to interannual timescale in the Irminger sea.

3.6.2.1. Seasonal full-depth OHC changes in the Irminger sea

The comparison of the seasonal cycle of the full-depth OHC changes in the Irminger sea from the 4DAtlantic-OHC product and in situ ISAS21 product is shown in Figure 29. One can notice that there is a good agreement between both full-depth OHC time series with a correlation coefficient of r=0.79 (at 95% confidence level). The 4DAtlantic-OHC seasonal minimum peak appears two months earlier than ISAS21 OHC one (Feb. vs Apr.), while its maximum peak appears one month earlier than ISAS21 OHC (Jul. vs Aug.). During Jan-Feb, the 4DAtlantic-OHC amplitude is larger than ISAS21 OHC, whereas over the rest of the year, it appears lower. Note that the seasonal variation of the OHC within the layer of 2000m to the bottom (magenta curve of Figure 29) does not play any significant contribution for the full-depth OHC seasonal change. In addition, it appears that the 4DAtlantic-OHC v0.4 and 4DAtlantic-OHC (with ECCO model) have a similar agreement feather against ISAS21 OHC at seasonal time scale in the Irminger sea (nearly the same correlation coefficient, fc. the main rapport of the validation task).



Ref.: OHCATL_DT_033_MAG Date: 15/05/2025

Issue: 3.0

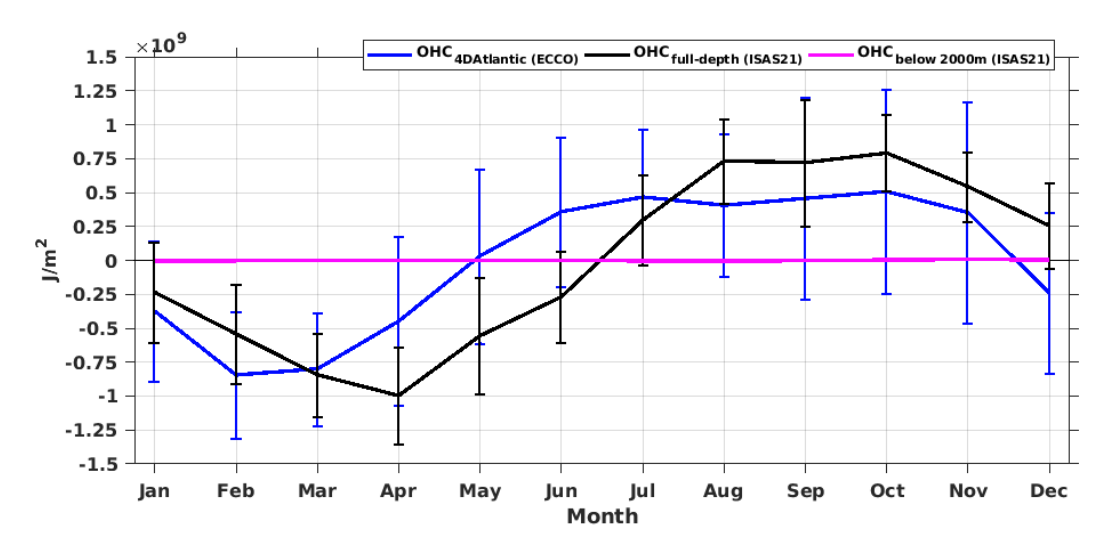


Figure 29: 2002-2017 climatology of seasonal time series of the full-depth OHC estimates from the geodetic 4DAtlantic (with ECCO model) product (blue curve) and ISAS21 product (black curve) in the Irminger Sea. The vertical blue and black bars represent the spatial STD for the selected domain for Irminger sea. The magenta curve represents the estimates of OHC seasonal cycle for the layer of 2000m-bottom from ISAS21 product.

3.6.2.2. Year-to-year full-depth OHC changes in the Irminger sea

Here, the comparison of time series of month-to-month of the full-depth OHC changes in the Irminger sea from 4DAtlantic-OHC against ISAS21 OHC estimates are shown in Figure 30. Both full-depth OHC time series exhibit an overall good agreement with a correlation coefficient of r=0.78 (with 95% of confidence level). One can notice that the year-to-year seasonal cycle of OHC is overall well reproduced by the 4DAtlantic-OHC, except during 2004 where its amplitude appears larger than the in situ ISAS21 OHC estimates. All full-depth OHC time series exhibit cooling trends. The 4DAtlantic OHC trends are twice more larger than the ISAS21 OHC trends: -6.59 ± 0.92 w/m² vs -2.9 ± 0.89 w/m². The month-to-month OHC changes within the layer of 2000m to the bottom appear to show non-significant contribution into the full-depth OHC changes.

Regarding the OHC interannual changes in the Irminger sea (Figure 31), all time series of the full-depth OHC show a good agreement (r = 0.87 at 95% confidence level). Large difference amplitudes (of $\sim 10^{\circ}$ J/m²) between time series can only be observed during 2003-2004. The OHC changes within the layer below 2000m depth are fairly small compared to the full-depth OHC changes signal.



Date: 15/05/2025 Issue: 3.0

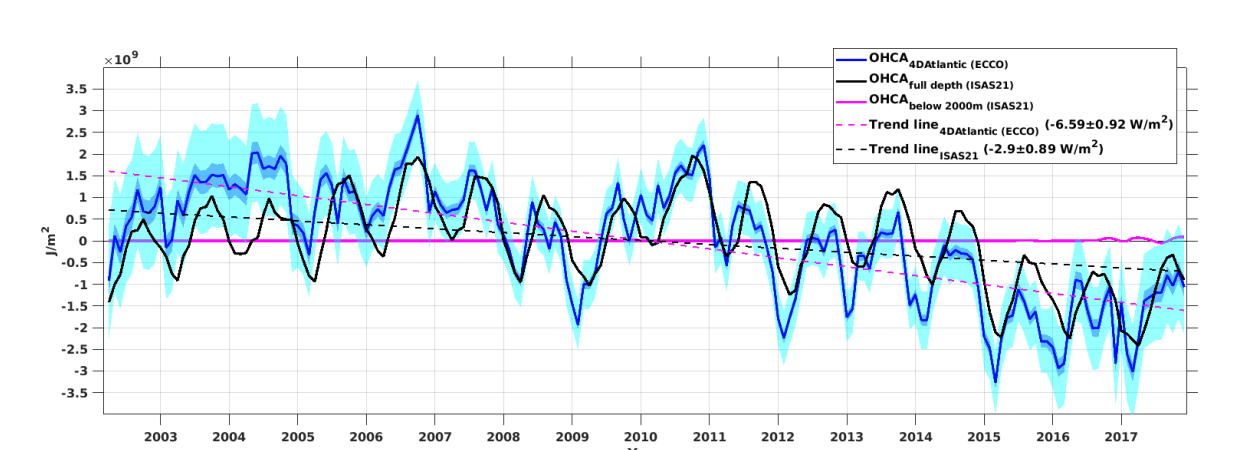


Figure 30: Interannual time series of the Ocean Heat Content Anomalies (OHC) referred the 2002-2017 OHC mean in the Irminger (selected area of the Figure 28, right figure) estimated from the space geodetic 4DAtlantic OHC product with ECCO model (solid blue curve) and the in situ ISAS21 data set (solid black curve). The magenta curve represents the interannual time series of OHC from ISAS21 within the layer of 2000m to bottom. The dashed magenta and black curves are OHC trend lines from 4DAtlantic and ISAS21 estimates respectively. The light blue and cyan bands represent the lower and upper bounds of error associated with the OHC estimates from the 4DAtlantic product.

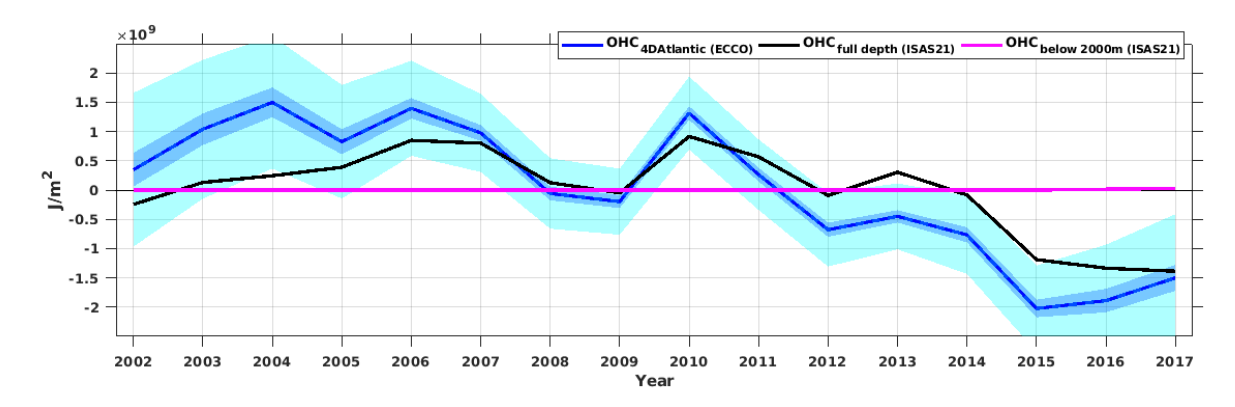


Figure 31: Interannual time series of OHC changes estimates over 2002-2017 in the Irminger sea from the geodetic 4DAtlantic product with ECCO model (blue curve) and from ISAS21 in situ product (black curve). Time series of OHC changes within the layer from 2000m depth to bottom (magenta curve) from ISAS21 in situ product. The light blue and cyan bands represent the lower and upper bounds of error associated with the OHC estimates from the 4DAtlantic product.

In the SPNA, coherent spatial OHC trends patterns in both OHC products are observed (Figure 32 a) and b)). Cooling trends patterns are also observed, while the 4DAtlantic-OHC product depicts larger amplitudes than the in situ ISAS21 product, notably in the Irminger and Labrador seas (ranging from \sim 10 to 30 w/m² of difference, Figure 32 c)). In the southern area of the SPNA, lower amplitude differences are observed (\sim ±5 W/m²).



Date: 15/05/2025 Issue: 3.0

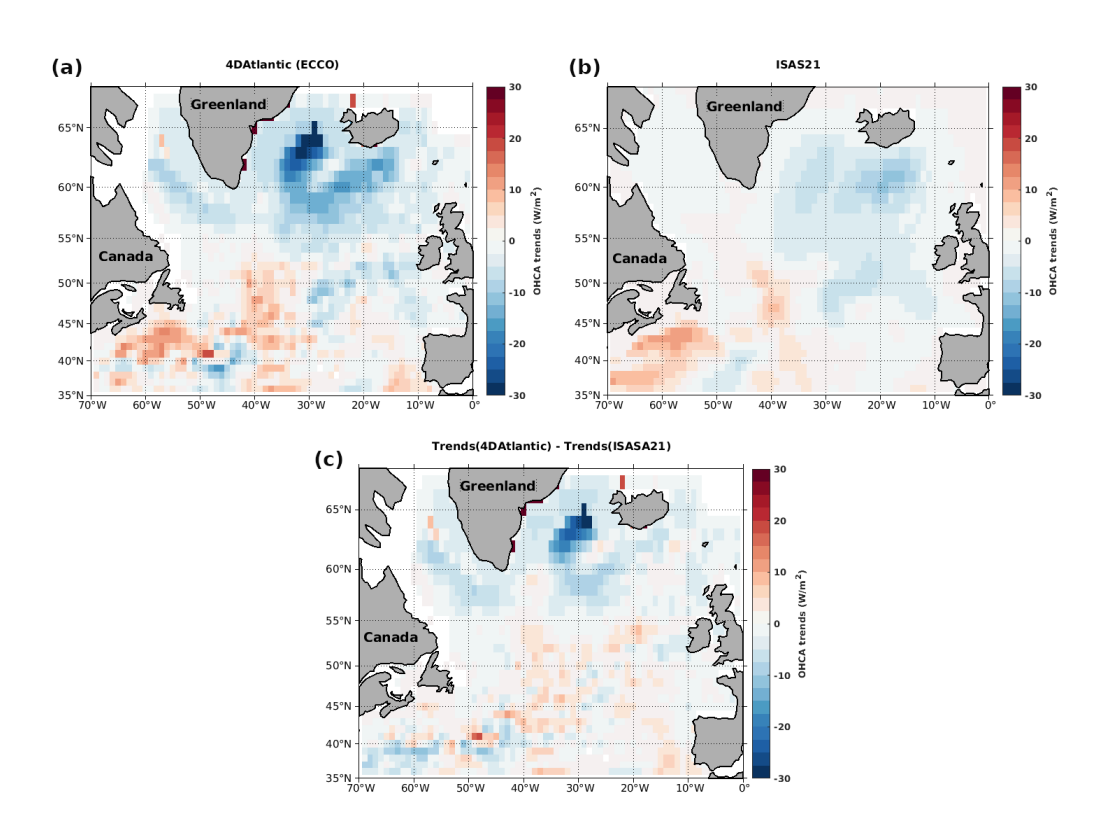


Figure 32: Trends of Ocean Heat Content Anomalies (OHC) over 2002-2017 from (a) 4DAtlantic product (with ECCO model) and (b) ISAS21 in situ product in the SPNA, and (c) represents the difference between (a) and (b).

3.6.3. 4DAtlantic with MASCON method vs ISAS21 estimates

This section stands to present and analyze the comparison between 4DAtlantic-OHC (with MASCON method) and ISAS21 OHC estimates from seasonal to interannual timescale in the Irminger sea.

3.6.3.1. Seasonal full-depth OHC changes in the Irminger sea

The times series of the seasonal cycle of the full-depth OHC changes from the 4DAtlantic-OHC product (blue curve for the product with MASCON method and green curve for the one with ECCO model) and the in situ ISAS21 estimates (black curve) are shown in Figure 33. There is good agreement between the 4DAtlantic-OHC (with MASCON method) and ISAS21 estimate (with correlation coefficient of r=0.99 at 95% confidence level). The 4DAtlantic-OHC product with MASCON method appears more reliable than the one with the ECCO model (blue curve vs green curve, Figure 33). The seasonal of the ful-depth OHC changes mostly appear within the layer from the surface to 2000m depth since the OHC changes from 2000m to the bottom do not play a significant role (magenta curve, Figure 33).



Ref.: OHCATL_DT_033_MAG Date: 15/05/2025

Issue: 3.0

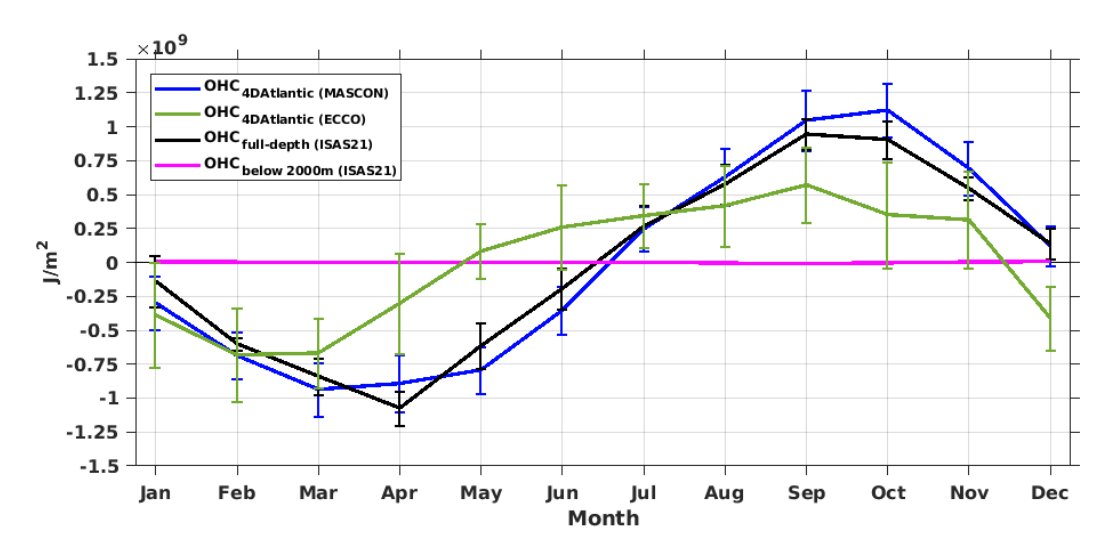


Figure 33: 2002-2020 climatology of seasonal time series of the full-depth OHC estimates from the geodetic 4DAtlantic (with MASCON method) product (blue curve) and ISAS21 product (black curve) in the Irminger Sea. The green curve stands for the 2002-2017 climatology of seasonal time series of the full-depth OHC from 4DAtlantic product (with ECCO model) within the red contour of the Figure 28 (right panel). The vertical blue, green and black bars represent the associated spatial STD for each selected for the Irminger sea. The magenta curve represents the estimates of OHC seasonal cycle for the layer of 2000m-bottom from ISAS21 product.

3.6.3.2. Year-to-year full-depth OHC changes in the Irminger sea

The inter-comparison of the times series of the month-to-month OHC changes over 2002-2020 from the 4DAtlantic-OHC product (with the MASCON method, blue curve) and ISAS21 estimates is shown (black curve) in Figure 34. Both time series exhibit a good agreement over the entire period (r = 0.91 at 95% confidence level), but in 2004 and in 2016, compared to the 4DAtlantic product with ECCO model (blue and black curves vs green curve, Figure 34). However, one can notice that beyond 2017, the amplitude of the 4DAtlantic-OHC time series appears larger than the ISAS21 estimates. Like in the previous sections, the OHC changes within the layer below 2000m depth are fairly small compared to the full-depth OHC changes signal, with a fairly visible fluctuation over 2017-2020 (magenta curve, Figure 34).

All OHC time series over 2002-2020 show cooling trends: -2.96 ± 0.86 w/m² and -4.42 ± 0.78 w/m² for the 4DAtlantic-OHC and the in situ ISAS21 OHC estimates, respectively. The 4DAtlantic-OHC trends over 2002-2020 appear almost twice lower than the ISAS21 OHC trends.



Date: 15/05/2025 Issue: 3.0

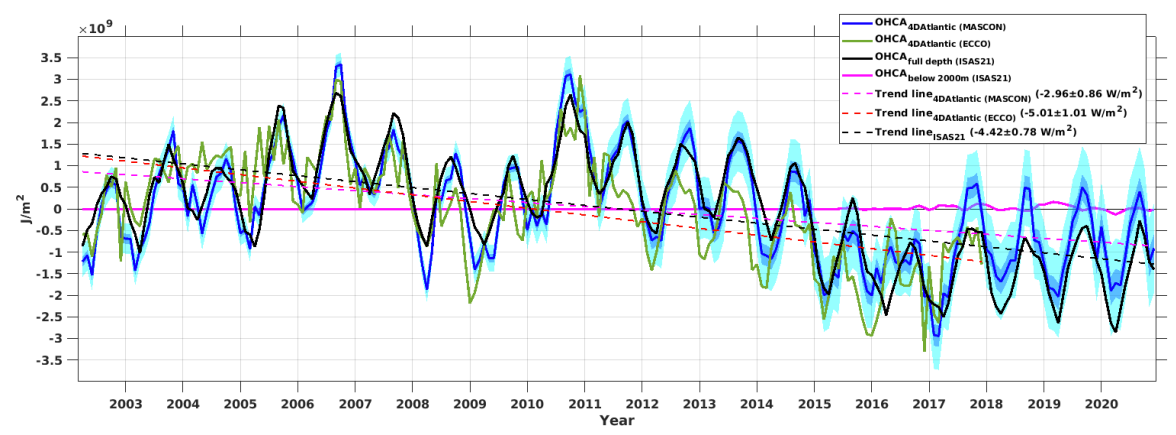


Figure 34: Interannual time series of the Ocean Heat Content Anomalies (OHC) referred the 2002-2020 OHC mean in the Irminger (within the red contour of the Figure 28, right panel) estimated from the space geodetic 4DAtlantic OHC product with MASCON method (solid blue curve) and the in situ ISAS21 data set (solid black curve). The magenta curve represents the interannual time series of OHC from ISAS21 within the layer of 2000m to bottom. The green curve stands for the interannual OHC time series from 4DAtlantic (with ECCO model, within the red contour of the Figure 28) over 2002-2017. The dashed magenta, red and black curves are OHC trend lines from 4DAtlantic (with MASCON method and ECCO model respectively) and ISAS21 estimates respectively. The light blue and cyan bands represent the lower and upper bounds of error associated with the OHC estimates from the 4DAtlantic product (with MASCON method).

The 4DAtlantic-OHC (with MASCON method) exhibits a coherent spatial OHC trend pattern against the in situ ISAS21 estimates in the SPNA (Figure 35 a) and b)). Consistent cooling trends patterns are also observed in the Irminger, Iceland and Labrador basins, while the 4DAtlantic-OHC product depicts larger heating trends of more than $\sim 5~\text{W/m}^2$ in the south of SPNA (Figure 35 c)). Thus, the 4DAtlantic-OHC product (with MASCON method) appears reliable enough in the SPNA.



Date: 15/05/2025

Issue: 3.0

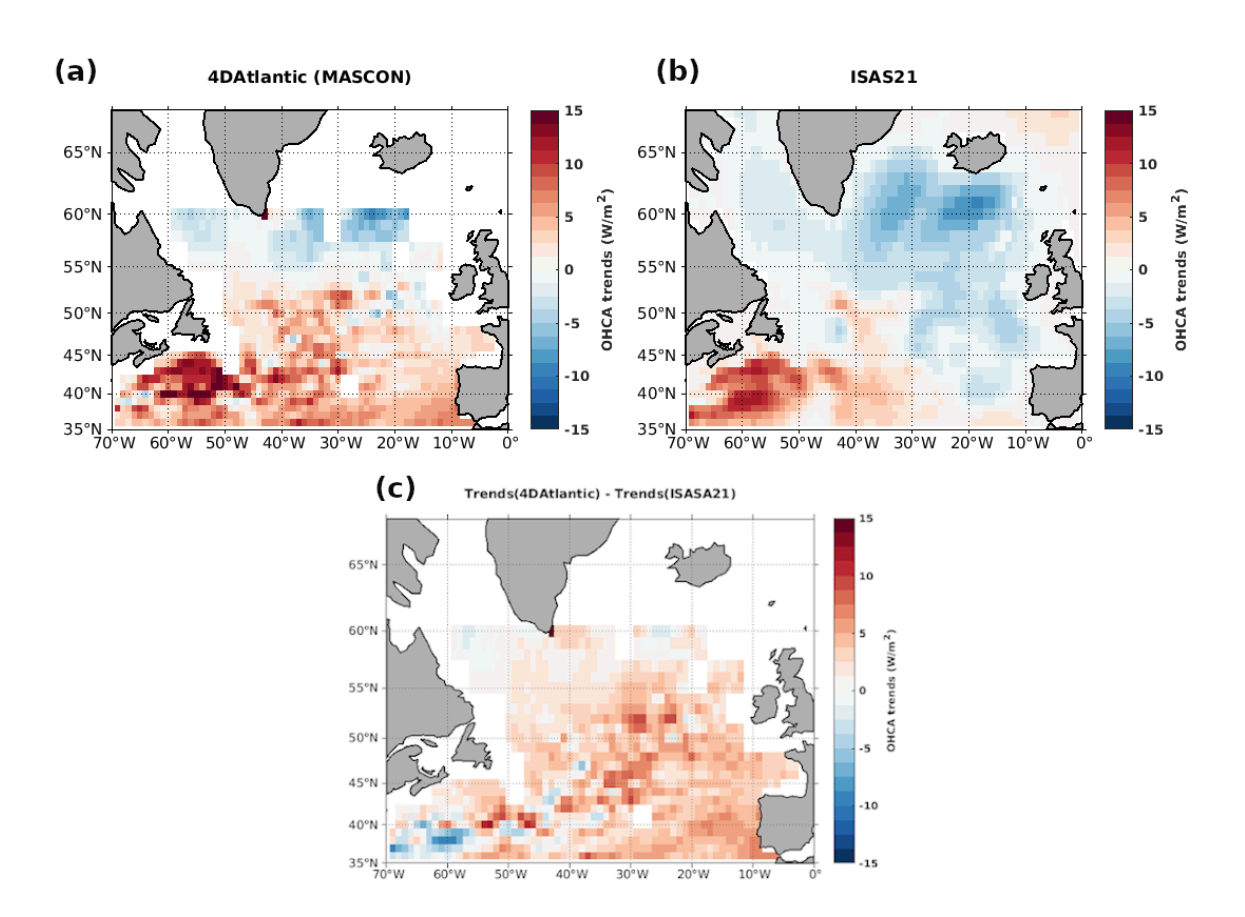


Figure 35: Trends of Ocean Heat Content Anomalies (OHC) over 2002-2020 from (a) 4DAtlantic product (with MASCON method) and (b) ISAS21 in situ product in the SPNA, and (c) represents the difference between (a) and (b).

At the interannual time scale, the OHC changes in the Irminger sea, all time series of the full-depth OHC time series show a good agreement (r = 0.95 at 95% confidence level, Figure 36). And again, the OHC changes within the layer below 2000m depth are fairly small compared to the full-depth OHC changes signal.

Date: 15/05/2025 Issue: 3.0

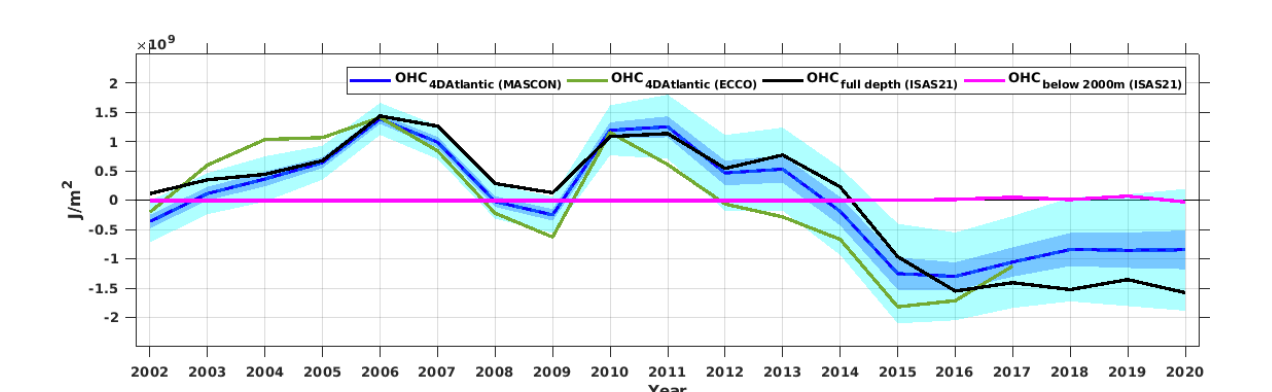


Figure 36: Interannual time series of OHC changes estimates over 2002-2020 in the Irminger sea from the geodetic 4DAtlantic product with MASCON method (blue curve) and from ISAS21 in situ product (black curve). The green curve stands for the one over 2002-2017 from the 4DAtlantic-OHC with ECCO model. The magenta curve represents the time series of OHC changes within the layer from 2000m depth to bottom from ISAS21 in situ product. The light blue and cyan bands represent the lower and upper bounds of error associated with the OHC estimates from the 4DAtlantic product.

3.7. Summary

In this validation activity, the 4DAtlantic-OHC v0.4 product was compared against in situ OHC estimates from A25-OVIDE hydrography data and ISAS21 gridded product in the Subpolar North Atlantic (SPNA). The comparisons at basin-scale along the OVIDE line showed that the 4DAtlantic-OHC estimates can locally underestimate in situ (A25-OVIDE) OHC estimates by about 40%. At biennial timescale and over the full period of OVIDE sections (2002-2018), the 4DAtlantic-OHC v0.4 shows a strong cooling trend (\sim -10.54 w/m²) not captured in the in situ OHC estimate (\sim -2 w/m²), yet both time series have a correlation of r = 0.6 (statistically-significant at the 95% confidence level). The 4DAtlantic-OHC v0.4 product notably showed a good ability to capture the OHC changes in the Irminger sea (\sim 0-750 km from Greenland, West of the Reykjanes Ridge), a region characterized by relatively quiescent dynamics compared to those basin east of Reykjanes Ridge, where the comparison shows less consistency.

At seasonal timescale, the comparison between the 4DAtlantic-OHC v0.4 and in situ ISAS21 OHC estimates in the Irminger basin depicts a good correlation (r=0.8 at 95% confidence level) although the geodetic seasonal signal in the is overall (except during winter) smaller by a factor \sim 2 compared to the in situ full-depth OHC estimates.

At interannual timescale, the 4DAtlantic-OHC v0.4 product demonstrates a good ability to capture the year-to-year OHC changes in the Irminger sea, with a correlation of r=0.8 (at 95% confidence level) against in situ ISAS21 OHC estimates (over 2002-2020). Consistent OHC trends of -5.28 \pm 0.73 w/m² and -4.42 \pm 0.78w/m² are respectively found for the 4DAtlantic OHC product and in situ ISAS21 estimates, respectively. The spatial distribution of the OHC trends within the SPNA also show good consistency between the two products.

Regarding the steric sea level intercomparison averaged over the OVIDE sections, we find good agreement over 2008-2014 (correlation coefficient of 0.8 at the 95% confidence level). However, the



Date: 15/05/2025

Issue: 3.0

SSLA 4DAtlantic estimates display larger amplitude variation than in situ estimates (in particular, during 2002-2006 and beyond 2014).

For the future progress in the validation of the 4DAtlantic OHC product, it would be worthwhile to extend the spatial coverage poleward (>60°N) and to provide a variance-covariance matrix at monthly timescale.

The 4DAtlantic-OHC products with ECCO model and MASCON method have also been evaluated against in situ ISAS21 OHC estimates from seasonal to interannual time scale. At seasonal time scale, the 4DAtlantic-OHC product with MASCON method (vs the one with ECCO model) shows a good ability to reproduce OHC changes in the Irminger sea against in situ ISAS21 estimates: r = 0.99 (vs r = 0.79 with seasonal minimum and maximum peaks largs for months). The 4DAtlantic-OHC product with MASCON method also shows a good ability (vs the one with ECCO model) to reproduce the OHC changes against ISAS21 estimates at interannual time scale (and also at decenal time scale, even if the times series are on \sim 19 years), with respect to the cooling and heating episodes. It should be worth noting that the 4DAtlantic-OHC (with ECCO model) cooling trend is twice larger than the in situ ISAS21, whereas the 4DAtlantic-OCH (with MASCON method) is twice lower than the in situ one. Furthermore, the systematic difference between 4DAtlantic-OHC product (with ECCO model) and ISAS21 OHC estimates largely increases northward in the Irminger sea (the one with the MASCON method seems negligible).

4. Validation on OVIDE section (V2.0)

In the second phase of validation activities, the 4DAtlantic-OHC products (V1; V2alpha and V2official) were compared against in situ OHC estimates from A25-OVIDE hydrography data and ISAS21 gridded product in the Subpolar North Atlantic (SPNA).

V2alpha was an intermediate version of the product produced during the development phase with certain improvements. Validation of this intermediate product enabled us to identify the improvements to be made for version V2official.

4.1. Comparisons against A25-OVIDE sections from Greenland to Portugal coasts

Figure 37 shows the full-depth OHC integrated along the OVIDE Greenland-Portugal hydrographic section in the 4DAtlantic-OHC products (blue lines), in the ISAS21 product (black lines) and from ship-based hydrography snapshots (red dots) for the for V1 (upper panel), V2alpha (middle panel) and V2official (lower panel) versions of the geodetic product.

As the 4Datlantic products cover different time periods, the validation activities will be reduced to the common 2005-2020 time-span. The linear full-depth OHC trends account for -2.59 \pm 1.04 W/m² , -1.12 \pm 1.02 W/m² and 1.8 \pm 0.96 W/m² for V1 , V2alpha and V2official, respectively. The corresponding linear trend in ISAS21 accounts for -3.53 \pm 0.8 W/m² . Therefore, we find that the 4Datlantic-OHC V1 trend is



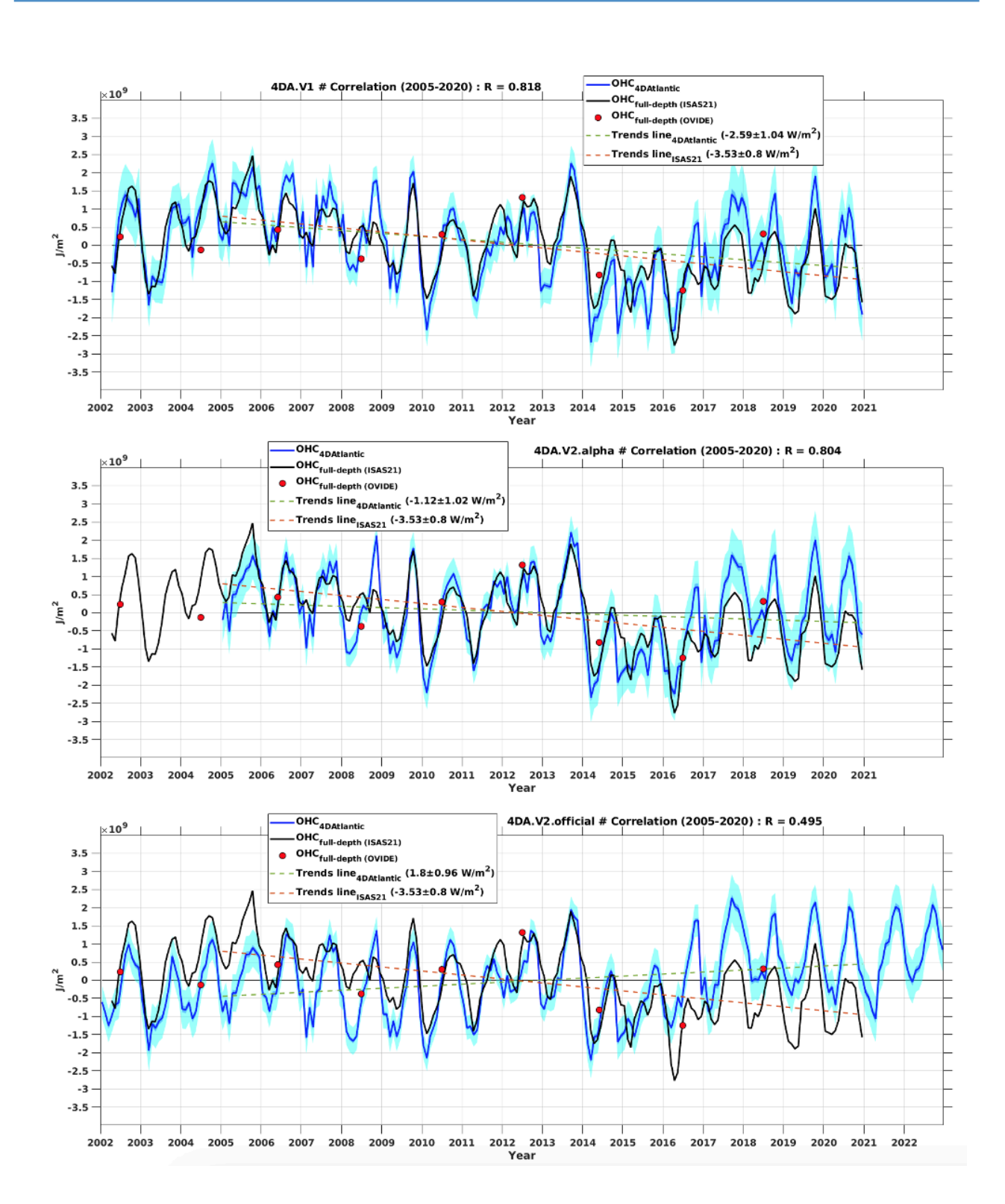
Date: 15/05/2025

Issue: 3.0

more in line with ISAS21 OHC trend estimate over 2005-2020. We also report a higher correlation coefficient between ISAS21 and V1 (0.81) than for V2alpha (0.80) and V2official (\sim 0.5). Larger discrepancies are particularly observed during the 2016-2020 time-span, with the geodetic products showing a positive bias and an overestimation of the annual cycle amplitude. Therefore, over the OVIDE section, our analysis shows that the V1 solution stands as the best fit to the ISAS21 gridded product.



Date: 15/05/2025 Issue: 3.0





Ref.: OHCATL_DT_033_MAG Date: 15/05/2025

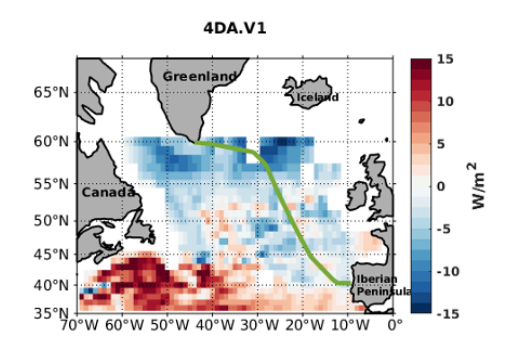
Issue: 3.0

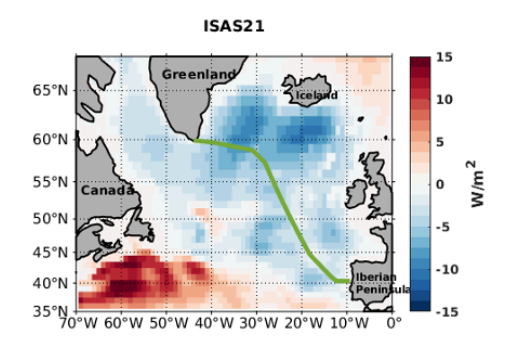
Figure 37: Time series of Ocean Heat Content per unit area (in J m-2) along the A25-OVIDE section over 2002-2021 for ISAS21 (black lines), the 4DAtlantic products (blue lines; V1 upper panel, V2alpha middle panel and V2official for the lower panel). The dashed red and black curves are OHC linear fits from 4Datlantic products and ISAS21 estimates respectively. The blue envelops represent the uncertainty range derived from the 4DAtlantic products. The red dots represent the full-depth OHC estimates from full-depth and high-resolution repeat hydrography cruises.

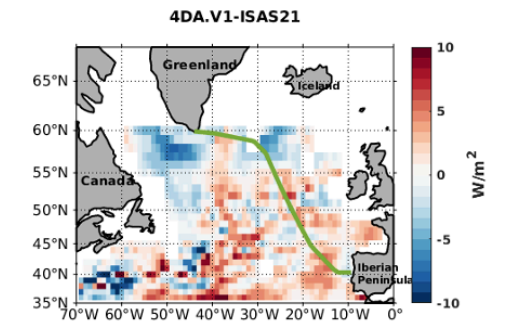
4.2. Comparisons against ISAS21 gridded products in the North Atlantic ocean

We also evaluate the aforementioned versions of the 4Datlantic-OHC products in the North Atlantic ocean. Figure 38 shows the regional OHC trends inferred from V1 product (upper right panel), ISAS21 (upper right panel) and the differences between V1 and ISAS21 (lower left panel). As previously mentioned (see Section 3), regional OHC trends in 4Datlantic-OHC V1 compares relatively well with ISAS21, with a consistent dipole between the northwestern subtropics (warming) and the northeastern subpolar (cooling) regions. Trend differences between the two products are in the order of 5 to 10 W/m2.

OHC Trends, 2005-2020









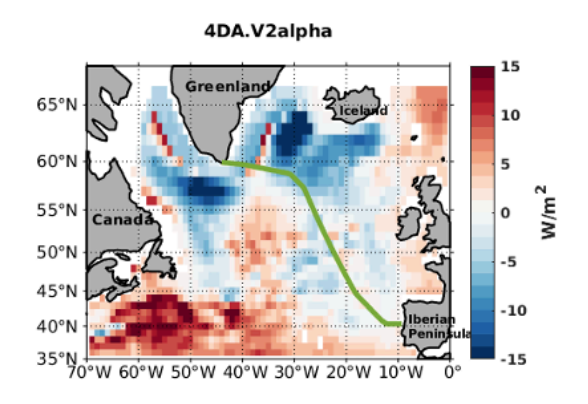
Date: 15/05/2025

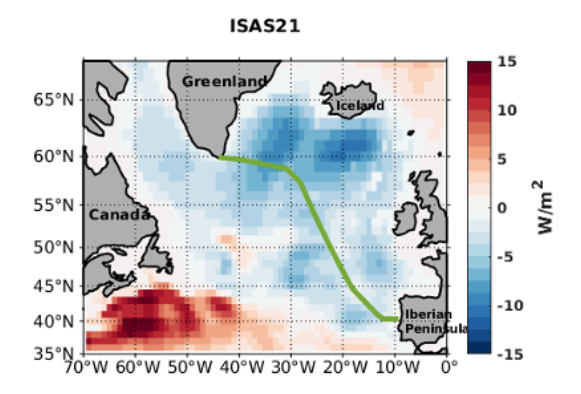
Issue: 3.0

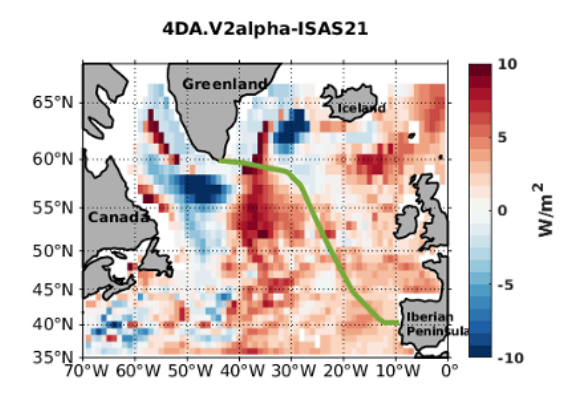
Figure 38: OHC trend maps (in W m-2) over 2005-2020 from 4DatlanticV1 product (upper left panel), ISAS21 in situ product (upper right panel) and the difference between 4Datlantic and ISAS21 products (lower right panel).

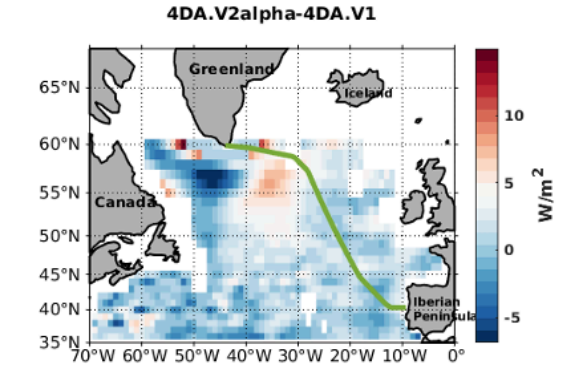
Figure 39 shows the maps of regional OHC trends computed over 2005-2020 for the 4Datlantic-OHC V2alpha product (upper left panel), ISAS21 product (upper right panel), the OHC trend differences between 4Datlantic-OHC V2alpha and ISAS21 (lower left panel) and the differences between 4Datlantic-OHC V1 and V2alpha (lower right panel). Compared to the V1 solution, V2alpha products has been extended northward to cover the entire subpolar North Atlantic ocean. V2alpha shows similar OHC trend patterns than the V1 solution with larger amplitudes (more than \pm 10W/m2 over the entire region). Comparisons with ISAS21 suggest larger biases than for the previous 4DAtlantic V1 product. Those biases include a widespread warming bias in the central and eastern basins (reaching as north as the Nordic Seas), cooling biases in the central Labrador and Irminger seas, and narrow but intense warming biases near Greenland's continental slopes. Biases are nearing the size of the signal for some locations (\pm 10 Wm-2).

OHC Trends, 2005-2020









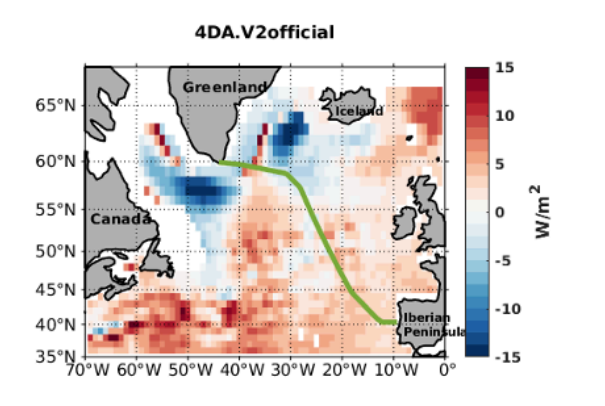


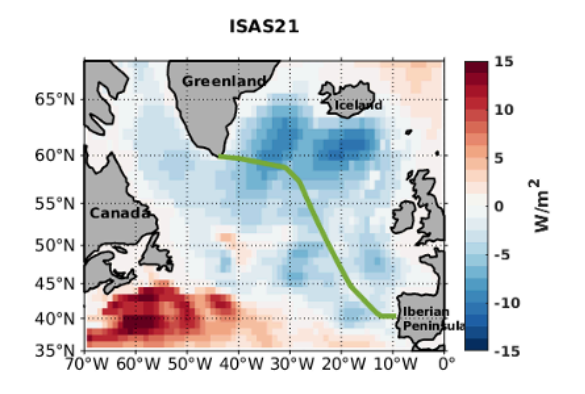
Date: 15/05/2025 Issue: 3.0

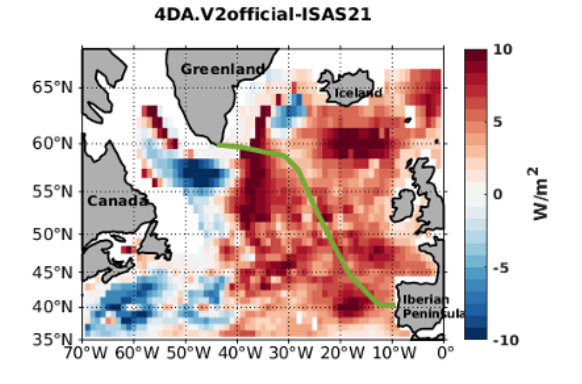
Figure 39: OHC trend maps (in W m-2) over 2005-2020 from 4DatlanticV2alpha product (upper left panel), ISAS21 in situ product (upper right panel) and the difference between 4Datlantic and ISAS21 products (lower right panel) and between 4Datlantic V2alpha and V1 (lower right panel).

Figure 40 shows the maps of regional OHC trends computed over 2005-2020 for the 4Datlantic-OHC V2official product (upper left panel), ISAS21 product (upper right panel), the OHC trend differences between 4Datlantic-OHC V2official and ISAS21 (lower left panel) and the differences between 4Datlantic-OHC V1 and V2official (lower right panel). The V2 official solution shows a similar general trend pattern than the V2alpha, except for a weaker cooling of the northeastern subpolar basins (e.g. Iceland Basin) and a weaker warming of the northwestern subtropics. Similarly to the V2alpha product, V2 shows suspicious large regional OHC trends in the rims of the subpolar North Atlantic ocean. These patterns are surprising and seems conspicious. We find larger differences between V2 official and ISAS21 product with biases reaching up to 10 W/m2 almost everywhere in the eastern part of the North Atlantic ocean.

OHC Trends, 2005-2020







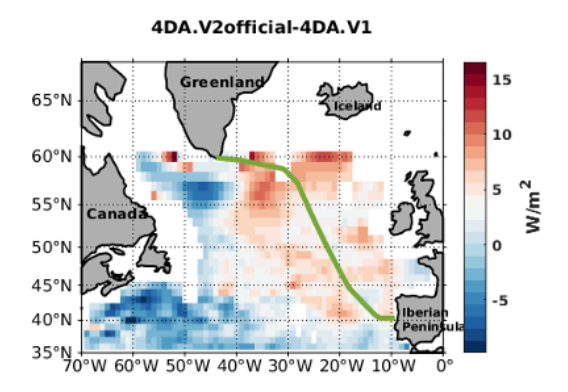


Figure 40: OHC trend maps (in W m-2) over 2005-2020 from 4DatlanticV2official product (upper left panel), ISAS21 in situ product (upper right panel) and the difference between 4Datlantic V2 official and ISAS21 products (lower right panel) and between 4Datlantic V2official and V1 (lower right panel).

Date: 15/05/2025

Issue: 3.0

5. Validation of the V3.0

As part of the current validation phase, the 4DAtlantic-OHC v3.0 product was systematically assessed against the previous version and in situ-derived OHC estimates from available gridded products (ISAS20, SIO, NOAA, EN4, IAP, IPRC, JAMSTEC). The 4DAtlantic-OHC v3.0 product represents a significant advancement over its predecessor by extending spatial coverage beyond the Atlantic Ocean. Version 3.0 provides full global ocean coverage, including the Mediterranean Sea. This expanded domain allows for a more comprehensive assessment of OHC.

5.1. 4DAtlantic-OHC v3.0 product

OHC trends and variance estimated in each 1° grid cell for the 4DAtlantic v0.3 product are shown in Figure 41a. The overall patterns in the 4DAtlantic v3.0 dataset reveal consistent cooling trends in the Southern Ocean, Subtropical Western Pacific, Bering Sea, and SPNA, while positive trends dominate the rest of the global ocean. In the western North Atlantic, positive OHC trends reach up to 10 W m $^{-2}$. This pattern is particularly intensified in the Gulf Stream region and is likely associated with the warming of the North Atlantic subtropical gyre. Similar to the previous version, 4DAtlantic v3.0 displays suspiciously large regional trends in OHC along the margins of the subpolar North Atlantic, with values reaching as low as -10 W m $^{-2}$. Regarding OHC variance, the highest values are found in the ocean's most energetic regions, such as the Southern Ocean and western boundary currents (Figure 41b).



Date: 15/05/2025 Issue: 3.0

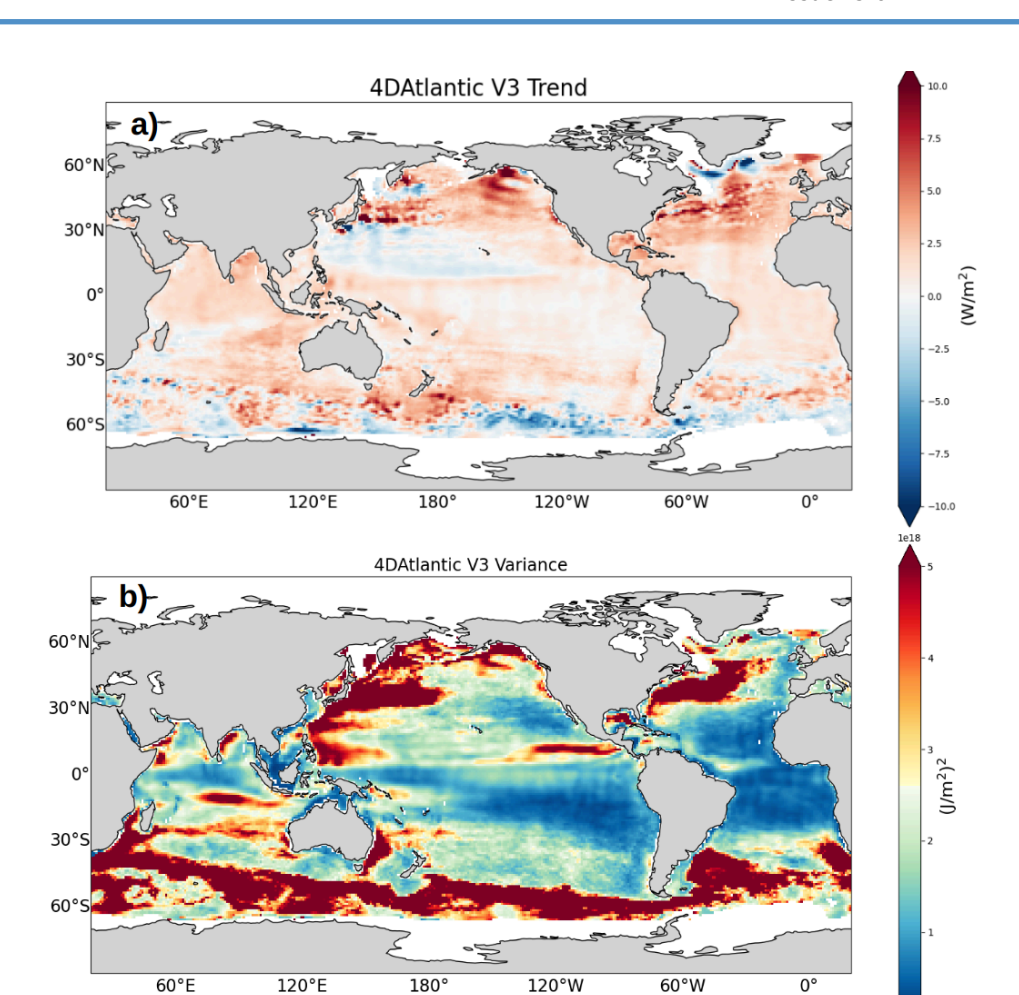


Figure 41: Anomalies in the Ocean Heat Content Trends (a) and variance (b) estimated using 4DAtlantic v3 dataset for the period April 2002—December 2022.

5.2. Comparative Assessment of 4DAtlantic-OHC v3.0 and v2.0 Products in the Atlantic Basin

To compare the OHC estimates from the latest two versions of the space-geodetic 4DAtlantic products, differences in OHC trend anomalies between versions 3 and 2 were analyzed (Figure 42). The inter-version trend differences reveal a pronounced hemispheric asymmetry, with 4DAtlantic version 2 yielding systematically lower OHC trend estimates in the North Atlantic and higher estimates in the South Atlantic compared to version 3. These differences may be attributed to the change in the International Terrestrial Reference Frame (ITRF) used in the altimetric data processing for the different versions of the space-geodetic 4DAtlantic products. Sea-level changes derived from altimetric measurements used to estimate 4DAtlantic-OHC products are referenced to ITRF2014 in version 2.0 and to ITRF2020 in version 3.0. Further detailed analyses are necessary to quantitatively assess the impact of this transition on the estimates.



Date: 15/05/2025

Issue: 3.0

Patterns of OHC variance are broadly similar between the two 4DAtlantic dataset versions. However, Figure 2 reveals slight regional differences. In particular, version 2 shows increased variance in the South Atlantic, especially near the Subantarctic Front, as well as in the SPNA region.

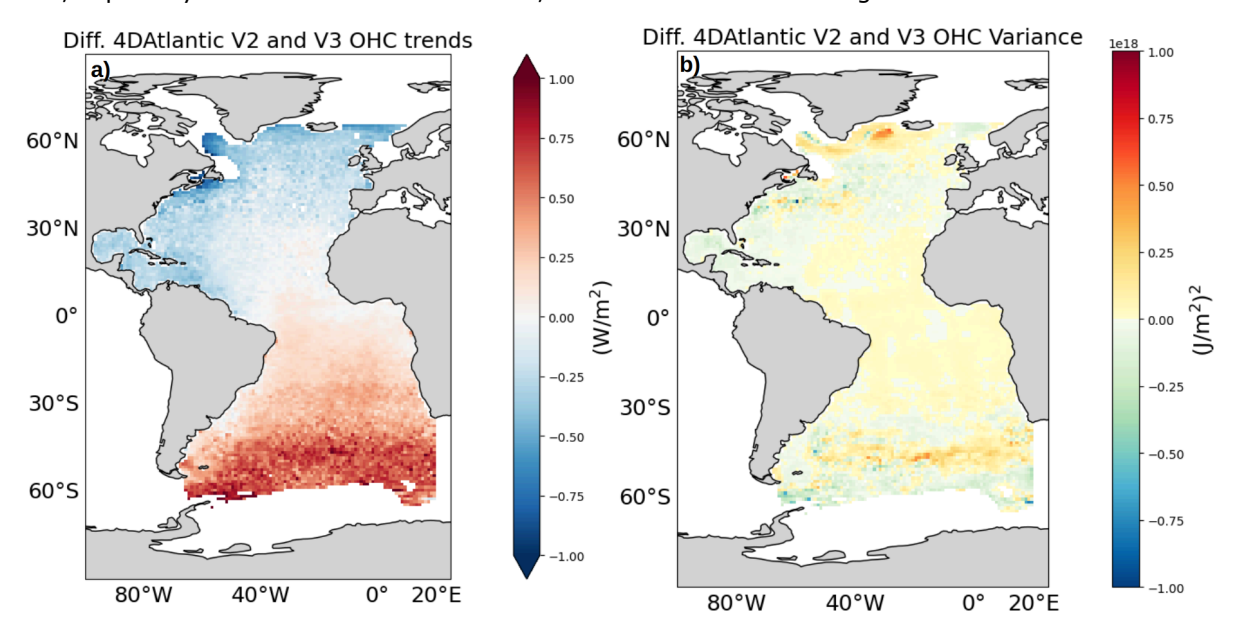


Figure 42: Anomalies in Ocean Heat Content Trend (a) and Variance (b): Differences between 4DAtlantic v3 and v2.

5.3. Evaluating differences between 4DAtlantic-OHC v3.0 and in situ products

To assess the accuracy of the 4DAtlantic-OHC v3.0 geodetic product, OHC trend estimates derived from geodetic observations are compared with those obtained from in situ datasets. At large spatial scales, the distribution of OHC trends shows good agreement between the geodetic and in situ products. The OHC trend patterns derived from the in situ dataset are very similar to those obtained from the geodetic estimates (Figure 43), displaying a coherent cooling signal across the Southern Ocean and the western Pacific, alongside widespread warming across the remainder of the global ocean basin. However, the most pronounced differences are located in the eastern North Atlantic, with biases reaching up to 10 W/m². The trend differences between V3.0 and in situ products range from 2 to 14 W/m².

The spatial distribution patterns of OHC variance from the 4DAtlantic v3.0 product and in situ-based estimates are generally consistent and of comparable magnitude (Figure 44). The main differences are observed in the Southern Ocean, particularly in the Pacific sector, where the geodetic product exhibits markedly larger variance compared to the in situ observations.



Ref.: OHCATL_DT_033_MAG Date: 15/05/2025 Issue: 3.0

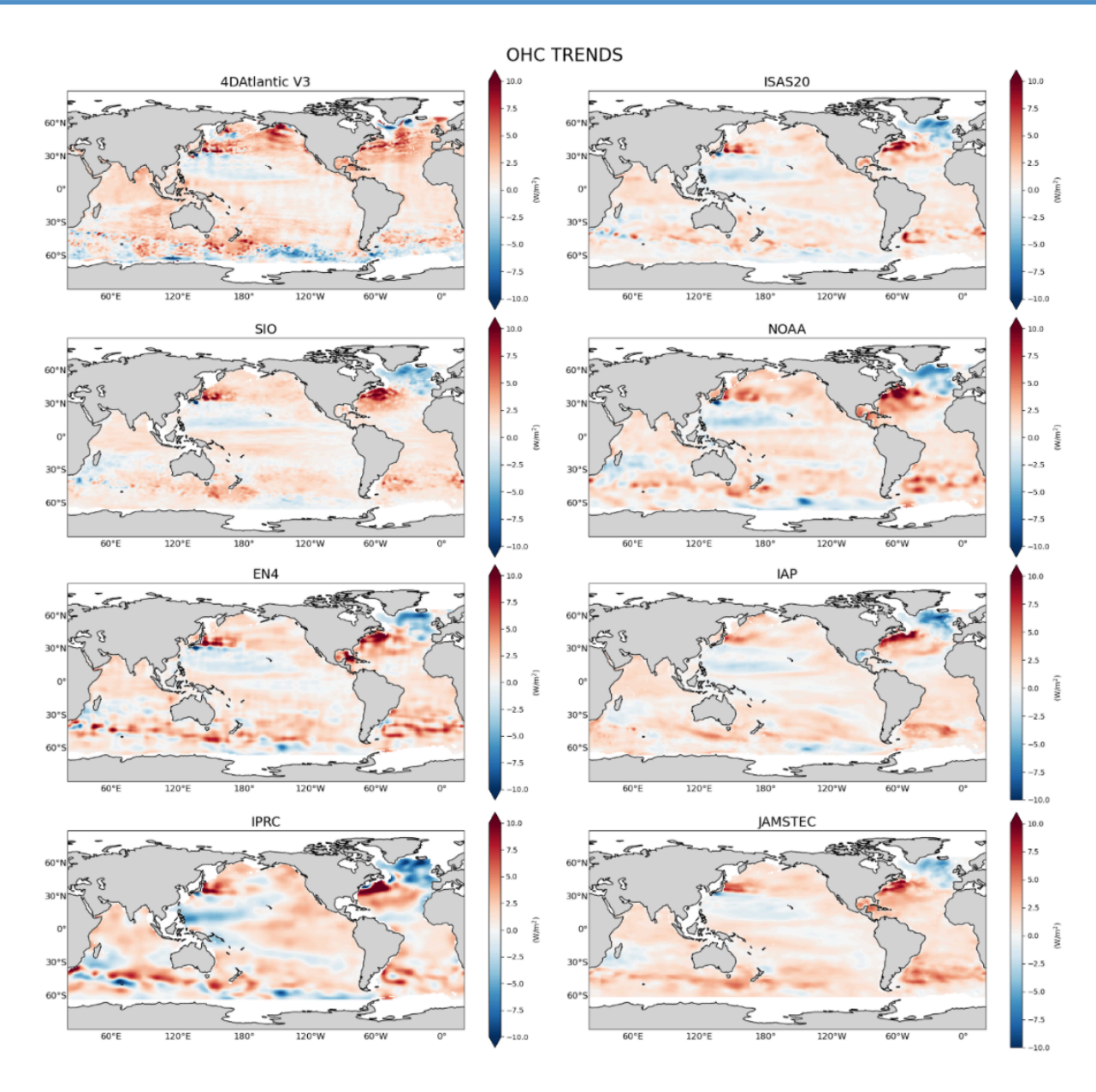


Figure 43: Ocean Heat Content Trend Anomalies from 4DAtlantic v3 and in situ products.

Date: 15/05/2025 Issue: 3.0

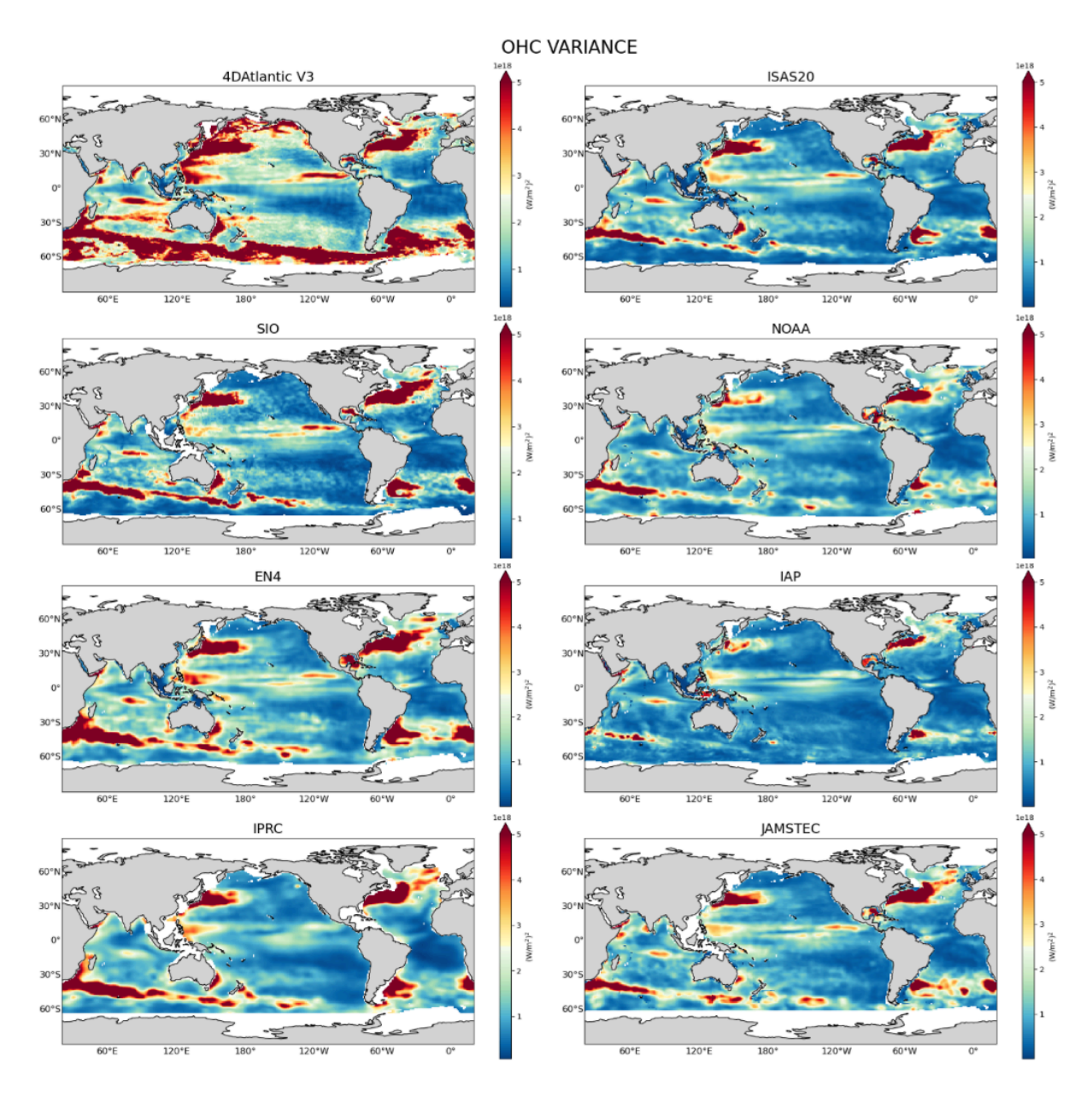


Figure 44: Standard deviation of the Ocean Heat Content from 4DAtlantic v3 and in situ products.

Date: 15/05/2025 Issue: 3.0

5.3. Analysis of the geodetic product in the Mediterranean Sea

OHC estimates derived from the 4DAtlantic v3 dataset exhibit predominantly positive trends across most of the Mediterranean basin ranging from 1 to $5~\mathrm{W/m^2}$ (Figure 45a). The strongest warming is observed in the southern sectors of the Western and Central Mediterranean, as well as in the eastern portion of the Eastern Mediterranean Sea. However, the southern part of the Eastern Mediterranean Sea exhibits a slight negative trend (-1 $\mathrm{W/m^2}$). Moreover, the Western Basin shows higher OHC variability compared to the Eastern Basin (Figure 45b). While achieving spatial coverage of OHC in the Mediterranean Sea represents a significant advancement, the observed patterns do not fully align with those estimated from in situ data (Kubin et al., 2023). These discrepancies are primarily attributed to limitations in the accuracy and resolution of the underlying gravimetric and altimetric datasets. Enhancements in the quality and consistency of these inputs are expected to be incorporated in forthcoming product versions, potentially improving the reliability of OHC estimates in this region.

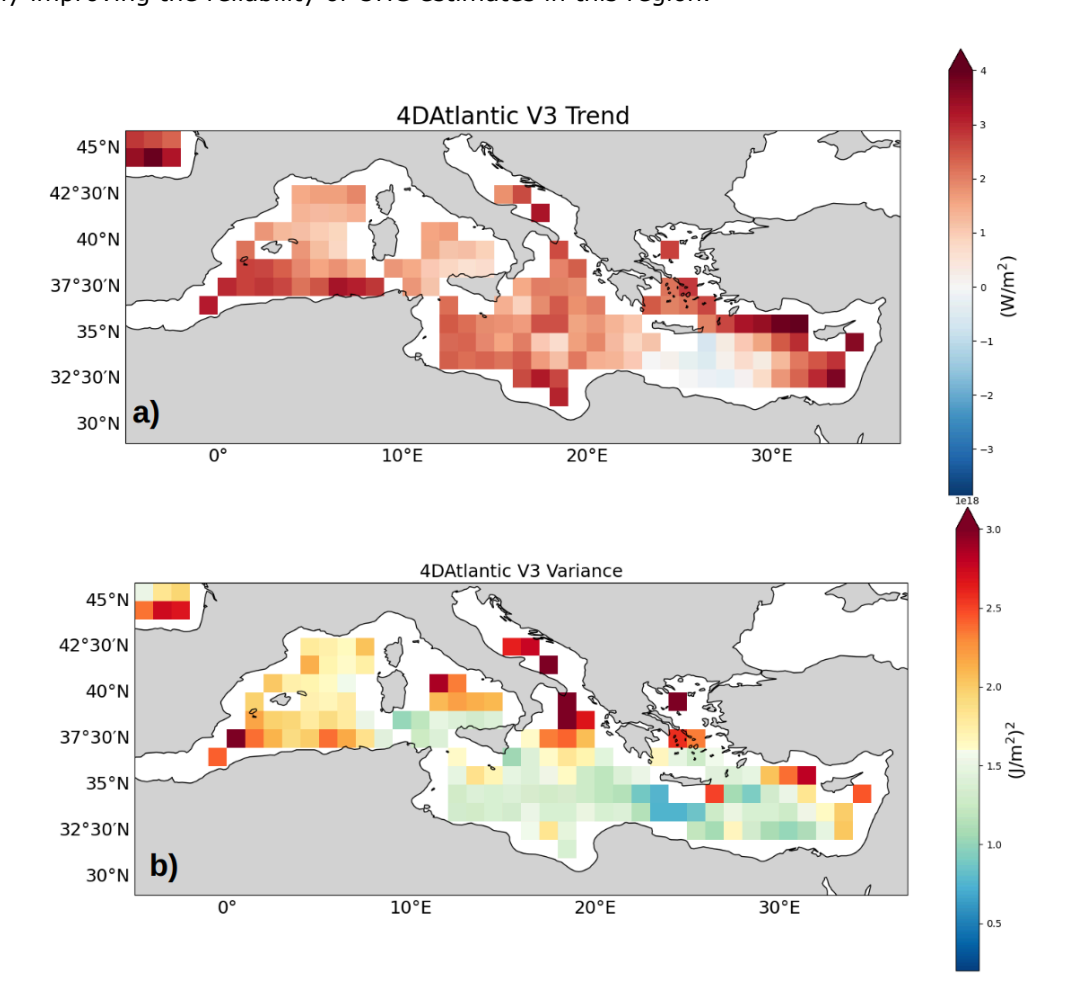


Figure 45: Anomalies in the Ocean Heat Content Trends (a) and variance (b) estimated using 4DAtlantic v3 dataset for the period April 2002–December 2022 in the Mediterranean Sea.



Date: 15/05/2025

Issue: 3.0

5.3. Assessing global ocean heat content from geodetic and in situ observations

Figure 46 presents the Global Ocean Heat Content (GOHC) estimates for the Atlantic Basin derived from the 4DAtlantic v2 and v3 products, with the seasonal cycle removed from both datasets. The overall pattern of GOHC variability remains consistent between the two versions, with similar amplitudes and comparable linear trend magnitudes.

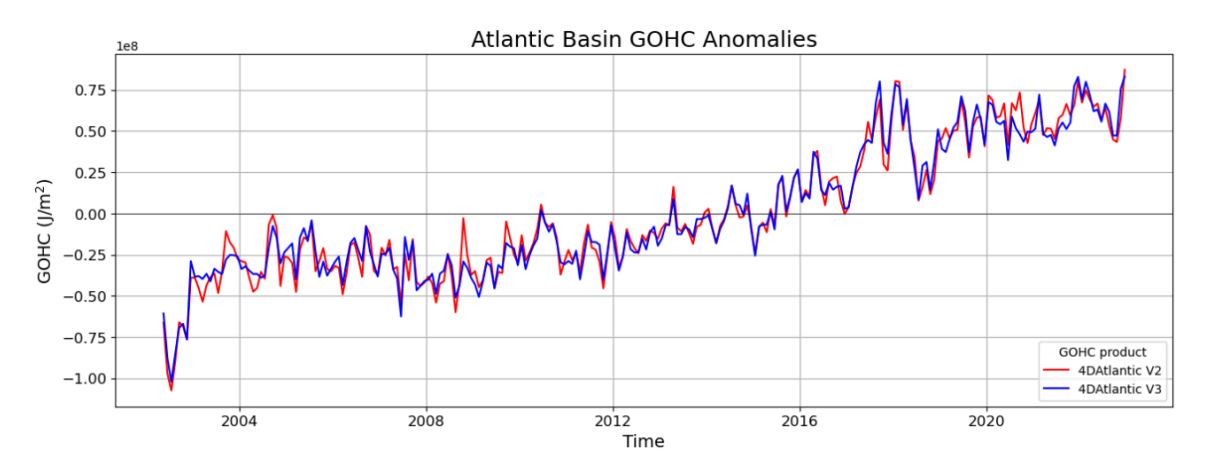


Figure 46: Time series of Global Ocean Heat Content derived from the 4DAtlantic v2 (red) and v3 (blue) datasets for the Atlantic Basin.

GOHC time series derived from the 4DAtlantic v3 are compared with those obtained from in situ datasets (Figure 47). The amplitude of GOHC variability showed good agreement between the geodetic and in situ products. However, the most pronounced discrepancies appear in the trend estimates over the full analysis period, with the 4DAtlantic v3 GOHC product exhibiting trends at least 0.25 W/m² higher than those derived from in situ observations (Table 3).

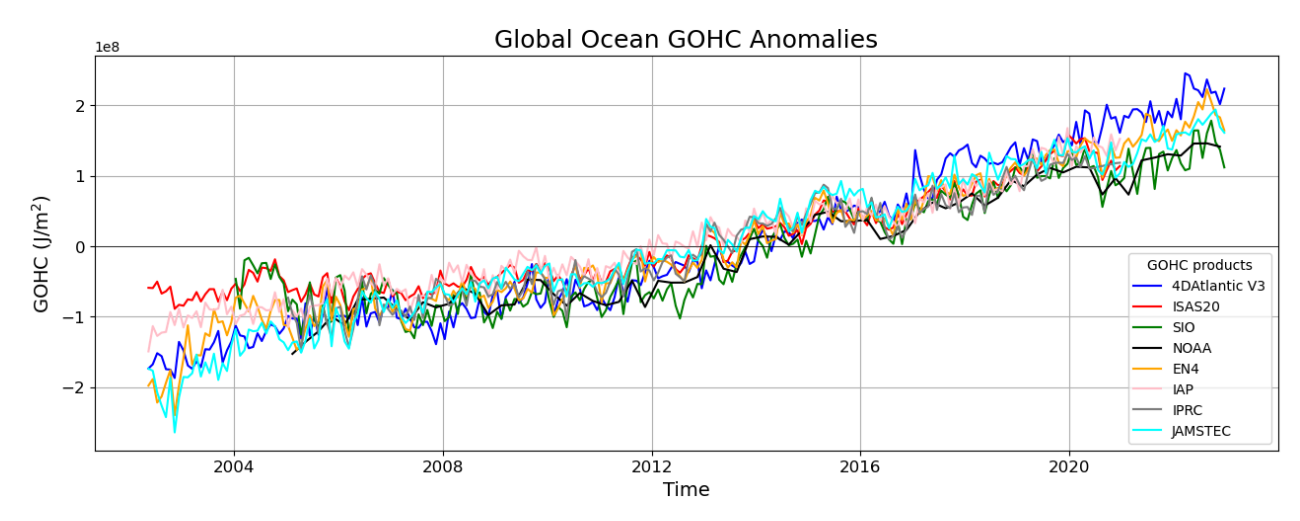


Figure 47: Time series of Global Ocean Heat Content derived from the 4DAtlantic v3 and in situ products.

Date: 15/05/2025

Issue: 3.0

Produc t	4DAtlantic v3	ISAS20 20	SIO	NOAA	EN4	IAP	IPRC	JAMSTEC
Linear trend (W/m²)	0.6	0.36	0.43	0.48	0.51	0.42	0.47	0.55

Table 3: Linear trends of the Global Ocean Heat Content time series derived from the 4DAtlantic v3 and in situ products.

6. Conclusions

6.1. Validation of the V1.0

The validation activities of the 4DAtlantic-OHC product were carried out by two independent working groups of the project team. It was conducted on the northern part of the Atlantic Ocean and shows the evolution from v0.2 to v0.4 versions. As a reminder, version V0.4 was chosen to be the official version 1.0 of the product and is disseminated publicly.

Firstly, the validation activities were carried out over the Subtropical North Atlantic region. The use of the NOC ARGO OI dataset has revealed that correlations between the in-situ product and the v0.4 product were significant over most parts of the Subtropical North Atlantic region. An additional analysis on the RAPID mooring section has highlighted a net amelioration of the 4DAtlantic-OHC product with final discrepancies being less than 5-10%. All the results have shown a net amelioration of the 4DAtlantic-OHC product from v0.2 to v0.4.

In the third part, the 4DAtlantic-OHC v0.4 product was validated in the Subpolar North Atlantic region. The v0.4 product was compared against in situ OHC estimates from A25-OVIDE. The comparison has shown good consistency between both products over the Irminger Sea but less over the Reykjanes Sea. The comparison of the v0.4 with ISAS21 gridded product emphasised the good consistency of the results of v4.0 against in-situ data over the Irminger Sea at both seasonal and interannual timescales. This good consistency has also been shown for spatial regional trends.

Concerning both validation, most of the differences between in-situ data and space geodetic products which are observed during the period 2016-2020 could be attributed to i) the spurious drift of conductivity sensors affecting salinity data and ii) the reliability of gravimetry data (there is a data gap between 06/2017 to 06/2018).

For the future progress in the validation of the 4DAtlantic OHC products, it would be worthwhile to extend the spatial coverage poleward (>60°N) and to provide a variance-covariance matrix at monthly timescales.



Date: 15/05/2025

Issue: 3.0

6.2. Validation of the V2.0

We conclude that the 4DAtlantic V1 solution remains as of today the best fit to observational hydrography-based and float-based OHC estimates in the North Atlantic. The V2 alpha and V2 official particularly show noticeable weakness along the OVIDE hydrographic section in the latest years (2016 onward) with an overestimated amplitude of the annual cycle and large departure from in situ OHC indices. This likely results in the strong departure of local OHC trends computed from those products, which include a striking warming bias in most of the domain as well as spurious artifacts near Greenland's continental slopes.

The use of salinity climatology for in situ data in the space geodetic product (cf. ATBD [AD-2] section 3.4.2) explains the degradation in terms of temporal correlation observed between 4DAtlantic V2 and the in situ data at local scales. There are two main reasons why the choice of the salinity climatology is relevant:

- 1) It allows the removal of the current drift in the halosteric sea level component at the global mean, which was detected by Barnoud et al. (2021) and is caused by an unexpected ageing of some sensors among the Argo network, especially after 2016. As the trend of the halosteric sea level component is assumed to be negligible, it is recommended to remove this drift. This study chose to use a climatology for the halosteric sea level component which does not contain any trends at local scale and at global mean.
- 2) Another ESA-supported project (MOTECUSOMA) recently demonstrated that the ocean heat uptake derived from the ocean heat content at a global scale displayed a better correlation with independent data using the climatology than the in-situ data for the sea level halosteric component.

Therefore the 4DAtlantic V2 solution is better than the V1 solution to estimate the ocean heat uptake and the earth energy imbalance.

6.3. Validation of the V3.0

A comparison of OHC trend anomalies between 4DAtlantic versions 2 and 3 reveals notable hemispheric asymmetries: version 2 shows lower trends in the North Atlantic and higher trends in the South Atlantic relative to version 3. These differences could be attributed to the change in the ITRF used in the altimetric data processing for the different versions of the space-geodetic 4DAtlantic products. While overall variance patterns are similar, version 2 exhibits slightly larger energy patterns in regions such as the South Atlantic near the Subantarctic Front and SPNA.

OHC trend estimates from the 4DAtlantic-OHC v3.0 geodetic product were compared to in situ datasets. At large scales, trends are consistent, showing similar cooling in the Southern Ocean and western Pacific, and warming elsewhere. However, significant biases (up to $10~\text{W/m}^2$) are observed in the eastern North Atlantic, with differences between V3.0 and in situ products ranging from 2 to $14~\text{W/m}^2$. Furthermore, OHC estimates from the v3.0 dataset reveal predominantly positive trends ($1-5~\text{W/m}^2$) across the Mediterranean, with strongest warming in the southern Western and Central sectors and the eastern Eastern Basin. A weak negative trend ($-1~\text{W/m}^2$) is observed in the southern Eastern Mediterranean. The Western Basin also exhibits greater OHC variability. While the dataset represents a step forward in spatial coverage, notable discrepancies with in situ estimates—likely due to limitations in gravimetric and altimetric data—highlight the need for improved input data in future product versions.



Date: 15/05/2025

Issue: 3.0

Finally, GOHC variability patterns for the Atlantic Basin are consistent between both versions, exhibiting similar amplitudes and trend magnitudes. Although the amplitude of GOHC variability is consistent between geodetic and in situ products, the 4DAtlantic v3 solution exhibits systematically higher linear trend estimates ($> 0.25 \, \text{W/m}^2$) over the full analysis period.

End of the document

